Universidade de Aveiro Departamento de Engenharia Mecânica
2020

Mariana
Peneda Conde

Design of a heterogeneous interior notched specimen using shape optimisation approach

Desenvolvimento de um provete heterogéneo recorrendo à otimização de forma do recorte

Universidade de Aveiro Departamento de Engenharia Mecânica
2020

Mariana Peneda Conde

Design of a heterogeneous interior notched specimen using shape optimisation approach

Desenvolvimento de um provete heterogéneo recorrendo à otimização de forma do recorte

Dissertação apresentada à Universidade de Aveiro para cumprimento dos requisitos necessários à obtenção do grau de Mestre em Engenharia Mecânica, realizada sob orientação científica de António Gil Andrade Campos, Professor Auxiliar com Agregação, do Departamento de Engenharia Mecânica da Universidade de Aveiro.

The author gratefully acknowledge the financial support of the Portuguese Foundation for Science and Technology (FCT) under the projects PTDC/EME-APL/29713/2017 (CENTRO-01-0145-FEDER-029713), PTDC/EMS-TEC/6400/2014 (POCI-01-0145-FEDER-016876), PTDC/EME-EME/31243/2017 (POCI-01-0145-FEDER-031243) and PTDC/EME-EME/30592/2017 (POCI-01-0145-FEDER-030592) by UE/FEDER through the programs CENTRO 2020 and COMPETE 2020, and UID/EMS/00481/2019-FCT - FCT - Fundação para a Ciência e a Tecnologia; and CENTRO-01-0145-FEDER-022083 - Centro Portugal Regional Operational Programme (Centro2020), under the PORTUGAL 2020 Partnership Agreement, through the European Regional Development Fund.

This work was also supported by the European Research Project VFormxSteels: "Toward virtual forming and design: Thermomechanical characterization of advanced high strength steels through full-field measurements and a single designed test", project number 888153 [2020].

o júri / the jury

presidente / president

Prof. Doutor João Alexandre Dias de Oliveira
Professor Auxiliar da Universidade de Aveiro

Prof. Doutor José Manuel Cardoso Xavier
Professor Auxiliar da *Faculdade de Ciências e Tecnologia da Universidade NOVA de Lisboa*

Prof. Doutor António Gil Andrade Campos
Professor Auxiliar com Agregação da Universidade de Aveiro (orientador)

agradecimentos / acknowledgements

Ao Professor Doutor António Gil Andrade Campos, pela brilhante orientação e constante disponibilidade ao longo de todo o percurso. Pela partilha de conhecimento, pelos diversos desafios propostos e pela confiança no meu trabalho. Um sincero agradecimento pelo incansável apoio prestado, mesmo em circunstâncias mais adversas. A toda a equipa de investigação que, ao longo desta jornada, me transmitiu o seu conhecimento e me auxiliou constantemente. Pessoas excecionais, que foram sempre um exemplo e uma inspiração. À minha família, pela incansável paciência e ajuda. Eles que são a razão de quem eu sou hoje. Um franco obrigado por tudo o que fazem e fizeram por mim. Aos meus amigos, pelo suporte e animo. Eles que são incansáveis e despertam o melhor que há em mim. Um sincero obrigado. Aos meus colegas de treino, pelo amparo nos momentos menos bons e sorrisos nos momentos de sucesso. Eles que me animam e suportam incessantemente. A todas as pessoas que se comigo se cruzaram ao longo do curso e de uma maneira ou de outra me tornaram uma melhor pessoa. A todos os docentes que fizeram parte do meu percurso académico, pelo conhecimento transmitido que levou ao meu desenvolvimento pessoal e profissional.

keywords Heterogeneity, mechanical testing, shape optimisation, finite element method (FEM), strain measurements, material behaviour, design by optimisation

abstract Nowadays, virtual predictions are essential in the design and development of new engineering parts. A critical aspect for virtual predictions is the accuracy of the constitutive model to simulate the material behaviour. A state-of-the-art constitutive model generally involves a large number of parameters, and according to classical procedures, it requires many mechanical experiments for its accurate identification. Fortunately, this large number of mechanical experiments can be reduced using heterogeneous mechanical tests, which provide richer mechanical information than classical homogeneous tests. However, the richness is much dependent on the specimen's geometry and can be improved with the development of new specimens. Therefore, this work aims to design a uniaxial tensile load test that presents heterogeneous strain fields using a shape optimisation methodology, by controlling the specimen's interior notch shape. The optimisation problem is driven by a cost function composed by several indicators of the heterogeneity present in the specimen. Results show that the specimen's heterogeneity is increased with a non-circular interior notch, compared to a circular one. The achieved virtual mechanical test originates both uniaxial tension and shear strain states in the plastic region, being the uniaxial tension strain state predominant.

palavras-chave

Heterogeneidade, ensaio mecânico, otimização de forma, método dos elementos finitos (MEF), medições de deformação, comportamento do material, projeto através de otimização

resumo

Hoje em dia, as previsões virtuais do comportamento dos materiais são essenciais para o projeto e desenvolvimento de novas peças e componentes de engenharia. Um aspeto fulcral para a sua virtualização é a exatidão dos modelos constitutivos. Um modelo constitutivo do comportamento de materiais geralmente implica um elevado número de parâmetros que, para uma correta identificação, são necessários diversos ensaios mecânicos clássicos. Este número de ensaios pode ser reduzido utilizando ensaios mecânicos heterogéneos, que providenciam mais informação mecânica do que os ensaios homogéneos clássicos. Contudo, a riqueza do ensaio mecânico é bastante dependente da geometria do provete usado, que pode ser melhorada através do desenvolvimento de novos provetes. Portanto, o objetivo deste trabalho é desenvolver um ensaio de carregamento uniaxial que apresenta estados de deformação heterogéneos, utilizando uma metodologia de optimização de forma, com o intuito de controlar a geometria do recorte interior do provete. O problema de otimização é guiado através de uma função objetivo composta por diversos indicadores de heterogeneidade presente no provete. Os resultados mostram que a heterogeneidade de um provete com um recorte interior não circular é superior ao de um circular. O ensaio mecânico obtido origina estados de tensão uniaxial e corte puro, na região de deformação plástica, sendo o estado de tensão uniaxial predominante.

Contents

List of Tables

Intentionally blank page.

List of Figures

Chapter 1

Introduction and background

1.1 Framework and motivation

Nowadays, for companies to be competitive, it is necessary to produce faster, with better quality and with the least waste of resources. The traditional production method based on empirical knowledge generates lots of waste as well as non-productive time. The improvement of modeling and numerical simulation tools has shown to improve these issues. The finite element method (FEM) can foretell the process of manufacturing and usage of the final product. Besides, more complex components can be analysed, leading to better quality outcomes. Finally, this technology can reduce the waste produced, make the time more valuable, thus, generate economic success. However, inadequate material parameters and simple constitutive models can result in unreliable conclusions. An accurate numerical simulation requires complex constitutive models, which involve significant amount of material parameters. To achieve an accurate material parameter calibration, many experimental tests are essential, such as the uniaxial tensile, simple shear, plane strain tension, and hydraulic bulge test. However, the large number of necessary experiments are costly and time-consuming.

Currently, classical tests are the core of the prediction of material macroscopic behaviour. Although these provide the stress and strain results for a fixed stress state, these do not resemble the complex stress and strain fields originated in many manufacturing procedures [Cooreman *et al.* 2008]. Therefore, a more complex mechanical test is necessary to better predict the behaviour of materials. Due to full-field measurements (FFM), such as digital image correlation (DIC), it is possible to obtain the strain fields along the surface of a specimen of an inhomogeneous mechanical test. DIC techniques allows the acquisition of rich and sufficient mechanical information with just a few experiments, or even for just one. Mechanical experiments with a specimen of a particular geometry, along with its specific boundary conditions, can result in a large range of stress and strain states. This approach can significantly reduce the number of mechanical experiments, as well as, enhance the calibration of the constitutive models and reliability of numerical simulations.

As demonstrated in Fig. 1.1, an improvement on a specimen's geometry could reduce the number of mechanical tests and improve the numerical material characterisation resulting in more accurate finite element simulation of sheet metal forming procedures and better development of components from different fields, such as aeronautics and automotive. The goal is to use validated modelling to replace physical testing at the

structural level of components.

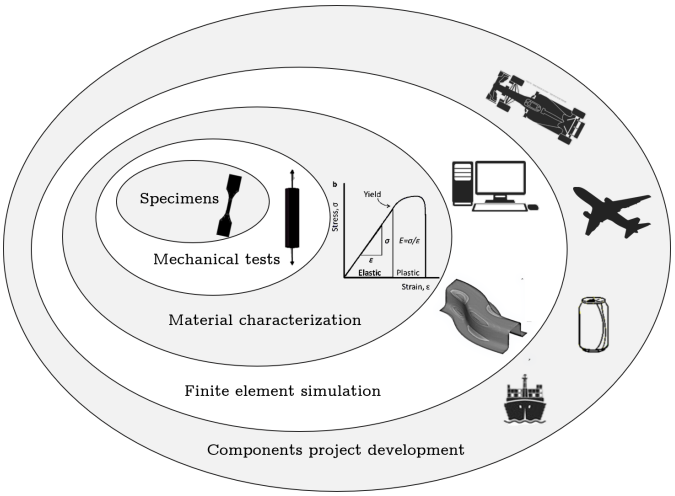

Figure 1.1: Framework and impact of this work.

1.2 Literature review

1.2.1 Homogeneous mechanical tests

Uniaxial tensile test

Uniaxial tensile tests provide information on the strength and ductility of materials under uniaxial tensile stresses [ASTM E8 2010]. For testing metallic materials in the form of plate, shapes, and flat material having a nominal thickness of 5 mm or over, a plate-type specimen is used. For testing materials in the form of sheet, plate, flat wire, strip, band, hoop, rectangles, and shapes ranging in nominal thickness from 0.13 to 19 mm, it is used sheet-type specimen. These two types of samples are the most commonly used and are represented in Fig. 1.2, along with the standard dimensions. The round specimens are used quite generally for testing metallic materials, both cast and wrought, and are represented in Fig. 1.3.

During a uniaxial tensile test with a round specimen, the engineering stress and engineering strain curve is obtained, as shown in Fig. 1.4. In Block 1, elastic and uniform deformations are undergoing up to the yielding point [Choung and Cho 2008]. From that point to the onset of diffuse necking, deformation is still uniform, but the material experiences plastic deformation. In Block 3, non-uniform plastic deformation occurs until fracture.

Shear test

Shear tests, among others, have turned out to be an effective way to characterise sheet metal yielding [Brosius *et al.* 2011]. Briefly, the device is designed in order to impose a parallel displacement of two lateral grips. The resulting deformation of the rectangular specimen is shown in Fig. 1.5.

When compared to the commonly used uniaxial test, the simple shear test has no necking development, it achieves a large range of homogeneous strains, the geometry

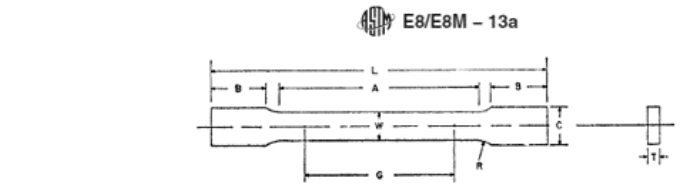

	Dimensions		
	Standard Specimens		Subsize Specimen
	Plate-Type, 40 mm [1.500 in.] Wide	Sheet-Type, 12.5 mm [0.500 in.] Wide	6 mm [0.250 in.] Wide
	mm [in.]	mm [in.]	mm [in.]
G—Gauge length (Note 1 and Note 2)	200.0 ± 0.2 [8.00 ± 0.01]	50.0 ± 0.1 [2.000 ± 0.005]	25.0 ± 0.1 [1.000 ± 0.003]
W—Width (Note 3 and Note 4)	40.0 ± 2.0 [1.500 ± 0.125, -0.250]	12.5 ± 0.2 [0.500 ± 0.010]	6.0 ± 0.1 [0.250 ± 0.005]
T—Thickness (Note 5)		thickness of material	
R—Radius of fillet, min (Note 6)	25 [1]	12.5 [0.500]	6 [0.250]
L—Overall length, min (Note 2, Note 7, and Note 8)	450 [18]	200 [8]	100 [4]
A—Length of reduced section, min	225 [9]	57 [2.25]	32 [1.25]
B—Length of grip section, min (Note 9)	75 [3]	50 [2]	30 [1.25]
C—Width of grip section, approximate (Note 4 and Note 9)	50 [2]	20 [0.750]	10 [0.375]

Figure 1.2: Rectangular tension test specimen [ASTM E8 2010].

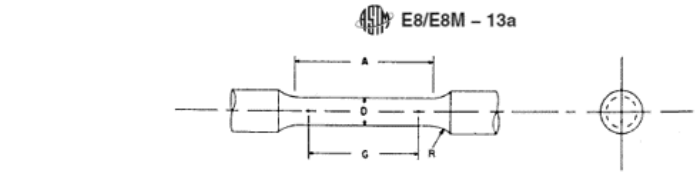

Dimensions, mm [in.]
For Test Specimens with Gauge Length Four times the Diameter [E8]

	Standard Specimen	Small-Size Specimens Proportional to Standard			
	Specimen 1	Specimen 2	Specimen 3	Specimen 4	Specimen 5
G—Gauge length	50.0 ± 0.1 [2.000 ± 0.005]	36.0 ± 0.1 [1.400 ± 0.005]	24.0 ± 0.1 [1.000 ± 0.005]	16.0 ± 0.1 [0.640 ± 0.005]	10.0 ±0.1 [0.450 ± 0.005]
D—Diameter (Note 1)	12.5 ± 0.2 [0.500 ± 0.010]	9.0 ±0.1 [0.350 ± 0.007]	6.0 ± 0.1 [0.250 ± 0.005]	4.0 ± 0.1 [0.160 ± 0.003]	2.5 ± 0.1 [0.113 ± 0.002]
R—Radius of fillet, min	10 [0.375]	8 [0.25]	6 [0.188]	4 [0.156]	2 [0.094]
A—Length of reduced section, min (Note 2)	56 [2.25]	45 [1.75]	30 [1.25]	20 [0.75]	16 [0.625]

Dimensions, mm [in.]
For Test Specimens with Gauge Length Five times the Diameter [E8M]

	Standard Specimen	Small-Size Specimens Proportional to Standard			
	Specimen 1	Specimen 2	Specimen 3	Specimen 4	Specimen 5
G—Gauge length	62.5 ± 0.1 [2.500 ± 0.005]	45.0 ± 0.1 [1.750 ± 0.005]	30.0 ± 0.1 [1.250 ± 0.005]	20.0 ± 0.1 [0.800 ± 0.005]	12.5 ± 0.1 [0.565 ± 0.005]
D—Diameter (Note 1)	12.5 ± 0.2 [0.500 ± 0.010]	9.0 ± 0.1 [0.350 ± 0.007]	6.0 ± 0.1 [0.250 ± 0.005]	4.0 ± 0.1 [0.160 ± 0.003]	2.5 ± 0.1 [0.113 ± 0.002]
R—Radius of fillet, min	10 [0.375]	8 [0.25]	6 [0.188]	4 [0.156]	2 [0.094]
A—Length of reduced section, min (Note 2)	75 [3.0]	54 [2.0]	36 [1.4]	24 [1.0]	20 [0.75]

Figure 1.3: Round tension test specimen and examples of small-size specimens proportional to the standard specimen [ASTM E8 2010].

is simple, and it is possible to reverse the load direction in the course of the experiment [Rauch 1998].

Concerning the one-sided shear test (Fig. 1.6a), the clamping areas are moved parallel to each other to generate a shear deformation in the gauge area [Brosius *et al.* 2011]. This experiment results in difficulties to achieve enough quality due to the reaction moment created by applying two opposing forces on shifted lines of action. Hence, compensation of the relatively high reaction moment must be reached by complex clamping devices. Though, slipping of the clamps cannot be completely avoided.

The symmetrical shear test according to Miyauchi presents a specimen geometry which involves three clamping areas and two shear zones in between (Fig. 1.6b). Through a parallel displacement of the middle clamps relative to the outer ones, the zones in between are deformed by simple shear [Brosius *et al.* 2011]. Depending on the aniso-

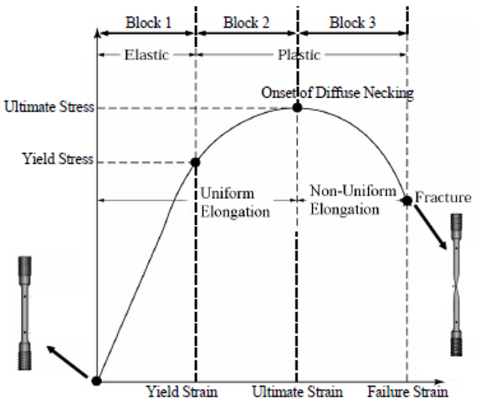

Figure 1.4: Engineering stress-strain representing three typical blocks in the ductile metal specimen under tensile load [Choung and Cho 2008].

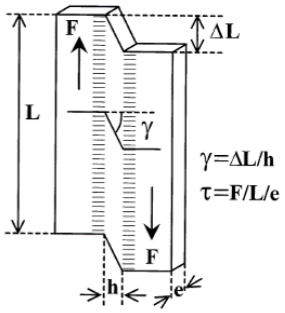

Figure 1.5: Geometry of a shear sample. The deformed volume is delineated by the indentations resulting from the clamping of lateral grips [Rauch 1998].

tropy, the angle between the rolling direction and pre-straining, the shear zones can develop different results. Hence, the measured data may contain the averaged information from both shear zones, which makes it difficult to separate the exact reaction of each alone [Brosius *et al.* 2011].

(a) (b)

Figure 1.6: (a) One-sided shear test specimen and (b) shear test specimen according to Miyauchi [Brosius *et al.* 2011].

The shear test according to ASTM B831 is presented in Fig. 1.7a. Also operating with one single shear zone, this specimen can be installed in a universal testing machine

without extensive modification or high-strength clamping [Brosius *et al.* 2011]. The area between the fillets is sheared when loading with a tensile force. Due to the lack of any spatially adjacent clamps, a rotation of the shear area may occur for higher displacements [Brosius *et al.* 2011]. This sample is not recommended for cyclic loadings because of its buckling tendency.

The twin bridge shear specimen (Fig. 1.7b) has been introduced by [Brosius *et al.* 2011], along with the demonstration of the stress and strain calculus. By rotating the outer clamps against the inner ones, a plane torsional moment is transferred through the specimen and both bridges are sheared in the same way. This mechanical test is able to characterise the plastic behaviour of sheet metals and no unwanted high reaction moments need to be compensated. Since no high compressive forces need to be applied to the experimental setup, there is no danger of buckling, for cyclic loadings. Better results are reached when using optical strain measurements.

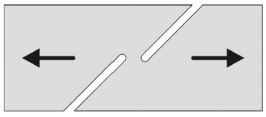

(a)

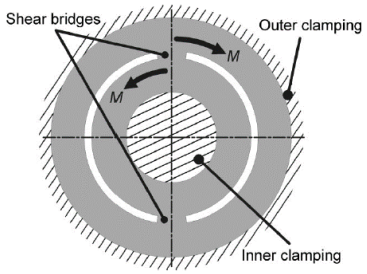

(b)

Figure 1.7: Schematic design of the (a) shear test specimen according to ASTM B831-05 [Brosius *et al.* 2011] and (b) the twin bridge shear specimen analysed in [Brosius *et al.* 2011].

Plane strain test

The plane strain test defines the location of the plane strain point in the first principal stress direction [Pijlman 2001]. A tensile test is performed on sheet metal with a large width compared to its length. The stress in the transverse direction cannot be measured, so the second principal stress is not determined. The gradient in the plane strain point is infinite due to a zero strain in the transverse direction [Pijlman 2001].

[Wagoner 1981] proposed two specimen geometries (Fig. 1.8a) with the intention of characterizing plane strain tension. Using a universal testing machine, a tensile loading is applied to the samples, resulting in near plane strain tension in the centre of the samples.

[Pijlman 2001] suggested an experiment that combines plane strain and shear deformation using biaxial test equipment, shown in Fig. 1.8b. The sample is fixed between two pairs of clamps and the vertical translation of the clamps results in plane strain deformation. The centre of the specimen highlighted in Fig. 1.8b is the deformed zone. So that plane strain tension is obtained, the width of the deformation zone must be larger than the height.

Hydraulic bulge test

The hydraulic bulge test consists of the expansion of sheet metal with internal pressure

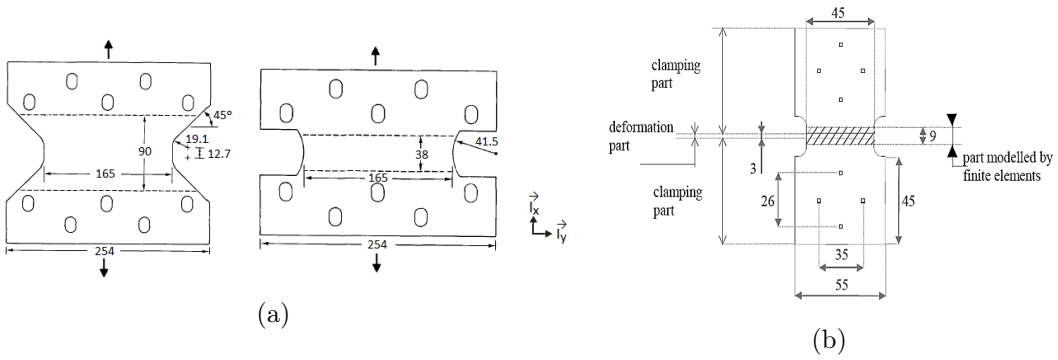

Figure 1.8: Specimen geometries (dimensions in mm) for plane strain testing proposed by (a) [Wagoner 1981] and (b) [Pijlman 2001].

while the edges of the specimen are held to prevent axial movement. During the experiment, the internal pressure, bulge curvature and thickness at the pole are measured continually up to rupture using analytical equations, optical methods or even mechanical methods. This test is used to determine the formability of various materials [Slota 2008]. Large strains are obtained during the bulge test, leading to a better description of the plastic properties of sheet metal, compared to the uniaxial tensile test. This test has advantages, such as the inexistence of frictional interactions, the simplicity of sample preparation and the stress-strain curve extending to the range of effective strain as found in many sheet metal forming processes [Campos *et al.* 2014].

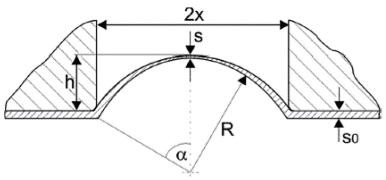

Figure 1.9: Geometric parameter of the hydraulic bulge test [Slota 2008].

1.2.2 Unconventional mechanical tests

Since the material parameters obtained from classical tests, in many cases, do not provide enough information to originate accurate numerical simulations, heterogeneous mechanical tests are crucial. Applying complex loading conditions, testing complex specimen geometries or a combination of both originates a non-homogeneous response of the material. Additionally, techniques are required to measure the strain fields and material parameter determination. Full-field deformation techniques are used to measure the heterogeneous strain fields on the surface of the specimen during the mechanical experiment and an inverse method is adopted to identify the material parameters employing for instance the finite element model updating (FEMU) in which an iterative procedure is used to minimise a cost function concerning the gap between experimental and numerical results.

Concerning biaxial loading conditions, the lack of standard cruciform specimens lead to the development of a new geometry based on the best combination of geometric para-

meters by [Makinde *et al.* 1992]. The method used was based on the statistical tools of factorial and response surface designs. The resulting geometry is a cruciform specimen with a circular reduced central region, as presented in Fig. 1.10.

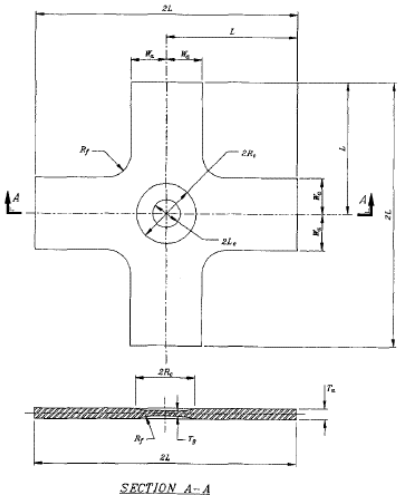

Figure 1.10: Typical cruciform specimen with a circular reduced central section geometrically analysed in [Makinde *et al.* 1992].

[Meuwissen 1998] investigated the usefulness of possible applications of the mixed numerical experimental methods for the mechanical characterisation of materials in a domain relevant for industrial metal forming processes. DIC was used to determine the displacement fields of the experimental tests. The material parameters were determined by means of an inverse method. It was performed a classic uniaxial tensile test, a uniaxial tensile test for an irregular plate with two perforations and one cyclic shearing experiment with a particular geometry, as presented on Fig. 1.11. In the non-standard tensile test, the geometry of the sample caused inhomogeneous stress and strain fields. For the shear experiment, the applied constitutive models resulted in relatively large prediction errors.

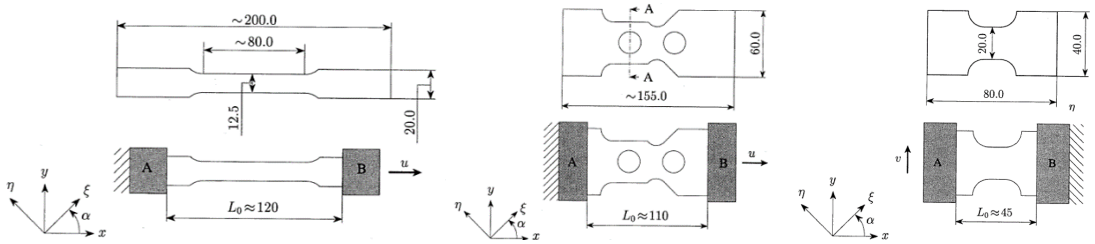

Figure 1.11: Geometry (dimensions in mm), thickness 1.5 mm and loading conditions of the (a) uniaxial tensile test specimen, (b) non-standard tensile test specimen and (c) shearing test specimen. α denotes the angle from the global x-axis to the rolling direction (ξ) of the material [Meuwissen 1998].

Regarding the uniaxial loading, a T-shape specimen was designed by [Grédiac *et al.* 1999] resulting in heterogeneous strain fields (Fig. 1.12). During the experiment, the dis-

placement field over the specimen was measured with an optical technique, using a grid method. The parameters identified showed some discrepancies from the expected, due to the need to differentiate the displacements. The differentiation tends to magnify the measurement noise of the displacements and to reduce the gradients. It is not just enough to develop a heterogeneous specimen it is also desirable an accurate method to analyse it.

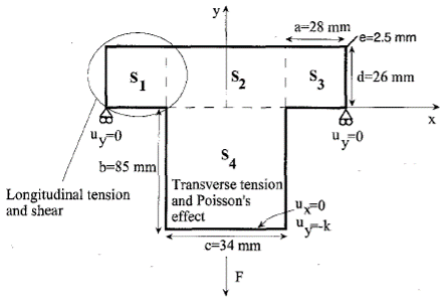

Figure 1.12: T-shape specimen and loading conditions considered in [Grédiac *et al.* 1999].

[Kajberg and Lindkvist 2004] presented a method for material characterisation subjected to large strains. The authors identified the material parameters in two types of constitutive models by inverse modelling using the specimen presented in Fig. 1.13 on a uniaxial test machine. The experimental field information was provided by Digital Speckle Photography (DSP) technique and the numerical data by Finite Element Analysis (FEA). Five material parameters were identified and the stress-strain curves obtained showed a good agreement with the standardised ones.

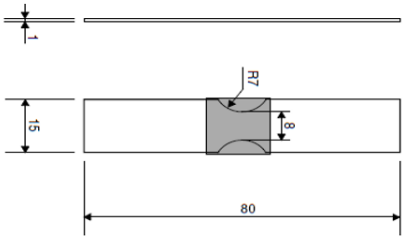

Figure 1.13: Specimen geometry for a non-standard uniaxial tensile test (dimension in mm) analysed in [Kajberg and Lindkvist 2004].

[Mohr and Henn 2007] developed an experimental technique along with a sample geometry to investigate the onset of fracture in metals at low and intermediate stress triaxialities. The mechanical test is performed on a universal biaxial testing device as showed in Fig. 1.14b. The flat specimen (Fig. 1.14a) exhibits different stress states within its gauge section depending on the direction and orientation of the displacement loading. For 90°loading, the predominant stress state is uniaxial tension at moderate strains; at 0°, it is pure shear and at an in-between angle, the stress distribution is non-uniform. The sample was designed in order to develop cracks in the centre area, due to the amplitude of the strains. The mentioned mechanical test offers different strain states depending on

the loading conditions, which does not reduce the number of experiments nor the number of samples but minimises the number of testing machines.

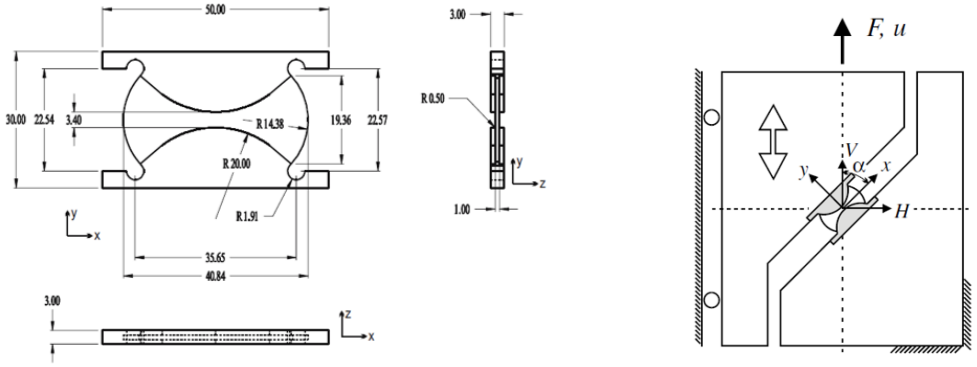

(a) (b)

Figure 1.14: Shape and dimensions in mm (a) of the designed flat specimen and (b) mechanical testing sketch developed in [Mohr and Henn 2007].

[Belhabib *et al.* 2008] proposed a specimen geometry for a non-standard tensile test, to identify material parameters using Finite Element Model Updating (FEMU). The aim was to get large strain heterogeneity in the gauge area, large strain-paths diversity and good sensitivity of the strain field to the material parameters. The authors have compared numerically and experimentally the strain fields, revealing qualitative accordance for three different specimen geometries. It was evaluated a classical tensile test, a plane tensile test and the proposed heterogeneous tensile test (Fig. 1.15). The proposed sample presented a wide heterogeneous strain field in the gauge area and a large diversity of the strain-paths in comparison to the two other specimens.

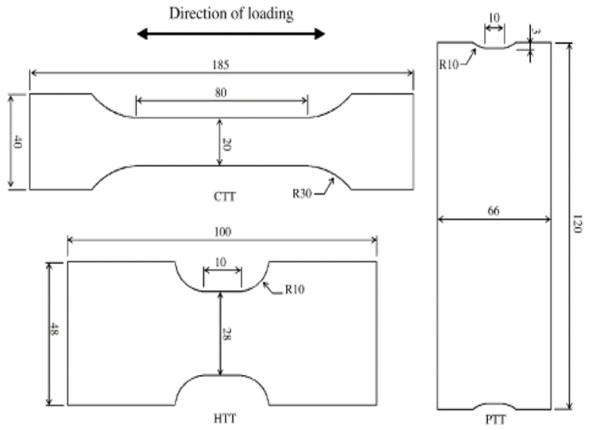

Figure 1.15: Shapes of the samples used in [Belhabib *et al.* 2008]: classical tensile test (CTT), plane tensile test (PTT) and the proposed heterogeneous tensile test (HTT).

[Cooreman 2008] made a similar study with a uniaxial specimen test on a perforated specimen as well as on a more complex geometry and a biaxial tensile test with a perforated cruciform, as can be seen in Fig. 1.16. Six material parameters were suc-

cessfully identified, reducing the number of the required experimental tests from at least three standard tensile tests to only one complex experiment. Additionally, it was recommended by the authors to develop the mechanical tests in agreement with the forming process, if the material behaviour is described by simple phenomenological models.

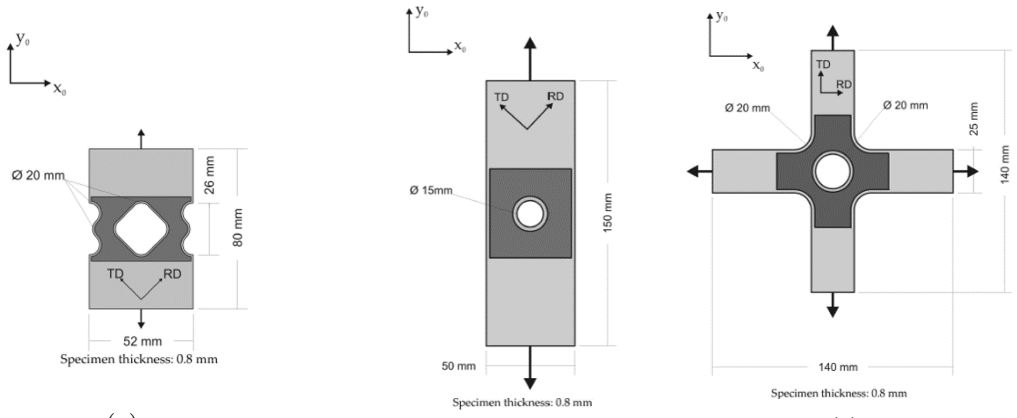

(a) (b) (c)

Figure 1.16: Set-up of (a) the uniaxial tensile test on the perforated tensile specimen, (b) the uniaxial tensile test on the complex shaped material specimen and (c) the biaxial tensile test on the perforated cruciform specimen studied in [Cooreman 2008].

[Syed-Muhammad *et al.* 2009] made a study on the optimisation of a bending test performed on anisotropic plate specimens. It was analysed the supports location, the applied force location, the shape of the specimen and the orientation of the material fibres separately or in combination. The heterogeneous strain fields were the input data for the determination of the constitutive parameters using the virtual field method (VFM). The global sensitivity to noise of the parameters to be determined was introduced as a cost function to be minimised. The main parameters influencing the optimisation process were the location of the supports and loads. The boundary specimen's shape optimisation, presented in Fig. 1.17, revealed to be less significant to the optimisation approach.

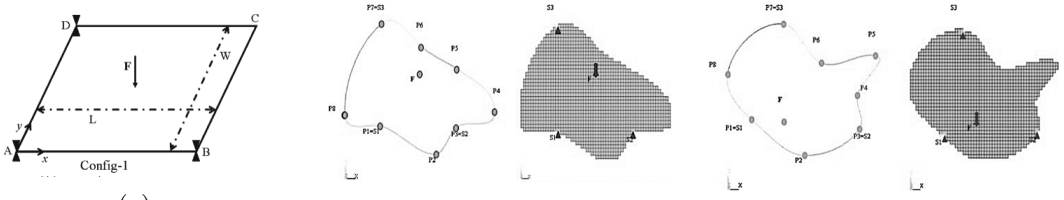

(a) (b) (c)

Figure 1.17: (a) Initial configuration of the shape optimisation procedure and (b) resulting shape with and (c) without fixed supports and force application analysed in [Syed-Muhammad *et al.* 2009].

[Banabic *et al.* 2010] made an interesting review regarding the advances of anisotropy and formability, in which is presented the experimental methods for measuring

and modelling the anisotropic plastic behaviour of metal sheets. Concerning the biaxial tension test using a cruciform specimen, the authors distinguish the samples into three types, as presented in Fig. 1.18. Type A provides difficulties in identifying an effective cross-sectional area for determining biaxial stress components accurately, due to having slits in the arms. The type B specimen has a gauge section thinner than the periphery. Hence, the thick periphery may prohibit uniform deformation of the gauge section. Besides, it has a varying thickness, so it is not easy to produce the sample. The type C samples provide a simple way to determine biaxial stress components in the gauge section by virtue of slits in the arms or welded thin strips. Moreover, this type of specimen is easy to make, although the C1 type requires welding for fixing the thin strips to the gauge section.

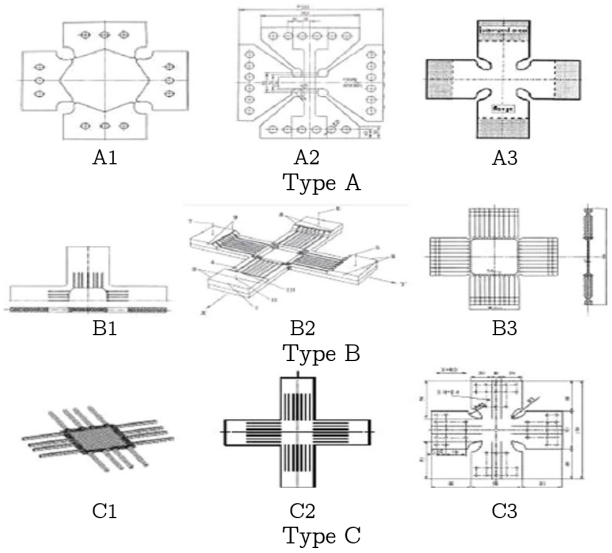

Figure 1.18: Cruciform specimens for biaxial tension experiments presented in [Banabic *et al.* 2010].

[Ishiki *et al.* 2011] carried out biaxial stress tests and in-plane tension/compression tests of pure titanium sheets to evaluate the anisotropic plastic deformation behaviour under linear stress paths. It was performed a biaxial tensile test of a cruciform specimen, combined tension-internal pressure tests on tubular specimens, combined tensile and compressive tests using a newly designed specimen (Fig. 1.19) and uniaxial in-plane compression test. The authors developed a new methodology for analysing the differential work hardening behaviour of the pure titanium sheet using the spline function of Bezier curves. The results showed good agreement with the differential work hardening behaviour of the pure titanium sheet.

[Pottier *et al.* 2011] compared three specimen geometries using uniaxial tensile tests: a classic tensile test with a basic sample, one perforated specimen, and one shear-like tensile test (Fig. 1.20). The authors applied the FEMU inverse method by the means of DIC to identify six material parameters of an anisotropic elastic-plastic constitutive model. A validation through simulation of a deep drawing forming operation was performed. It was proved that the proposed inverse method is able to decrease the number of tests required for the determination of the material parameters. The parameters iden-

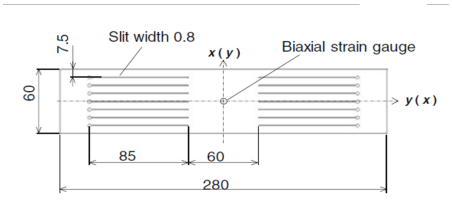

Figure 1.19: Specimen for combined tension-compression test (dimensions in mm) analysed in [Ishiki *et al.* 2011].

tified from the classic tensile test were unable to predict the global reaction force when other kinds of strain fields are involved. On the contrary, the shear-like specimen is the best to provide a good force prediction. Hence, it was demonstrated the improvement of parameter identification when heterogeneous strain fields are used. Regarding the deep-drawing validation, it was showed that the quality of the shape prediction increases with the strain field heterogeneity.

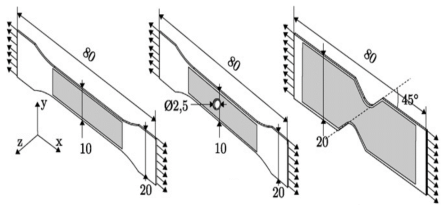

Figure 1.20: Investigated specimens geometries in [Pottier *et al.* 2011] and DIC analysis zones (dimensions in mm).

[Güner *et al.* 2012] proposed a method to include the distribution of strains in the identification of the planar anisotropy of sheet metals, including optical measurement of strains and an inverse parameter identification scheme. Aiming the generation of an inhomogeneous deformation field and giving equal importance to all types of deformation, the authors analysed numerically three notch radius variations of a uniaxial tensile test specimen (Fig. 1.21). The 5 mm radius sample showed difficulties in setting the tool displacement, with respect to a selected maximum strain not to exceed the flow curve limits. The 40 mm radius specimen hardly showed a deformation gradient. These two specimens were not selected for further studies. The deformation state of the 25 mm radius sample lied between the uniaxial tension and plane strain tension states. This geometry was experimentally tested and further analysed to determine the material parameters, revealing overall accordance in the distribution of the strains. However, the material parameters obtained were not accurate due to the assumption of neglecting the kinematic hardening.

[Pottier *et al.* 2012] proposed a heterogeneous mechanical test using a new sample geometry based on out-of-plane deformations. The sample was designed to exhibit tensile, shear and expansion behaviours, as can be seen in Fig. 1.22. The material parameters of an elasto-plastic constitutive model were successfully identified and, therefore, was concluded that the identification based on the heterogeneous test leads to better calibration of material behaviour than using a planar inverse identification.

[Zidane *et al.* 2014] numerically investigated several cruciform specimens from the literature and proposed a new specimen based on the geometry developed in [Johnston

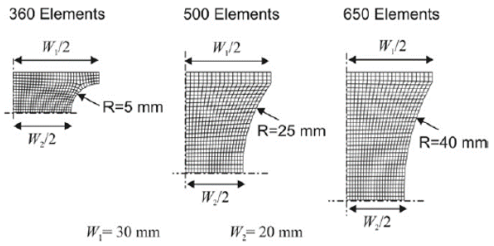

Figure 1.21: Specimen geometries and the finite element meshes with varying notch radii analysed in [Güner *et al.* 2012].

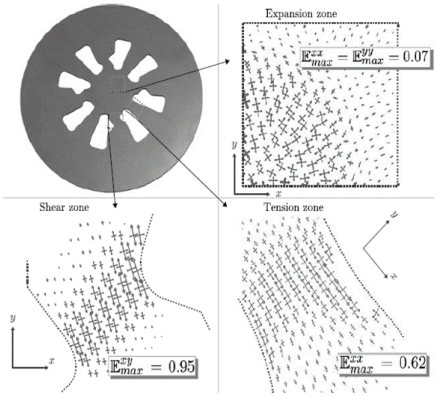

Figure 1.22: Sample geometry investigated in [Pottier *et al.* 2012] and principal strain directions after punch displacement $u_z = 10$ mm. E is the axial component of the Green-Lagrange strain tensor.

et al. 2002]. A parametric study on the length between the ends of the grooves and the edge of the square central zone, the fillet of the arms, the thickness and diameter of the central section was carried out to develop a sample that shows strain localisation in the central zone (Fig. 1.23). Experimental validation was successfully conducted.

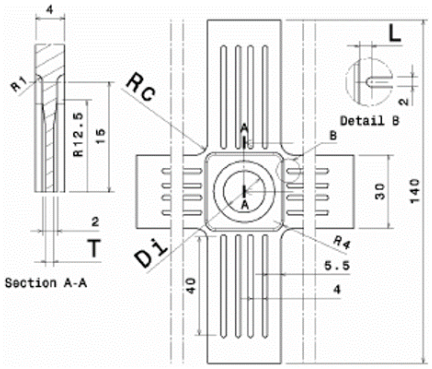

Figure 1.23: Geometry of the specimen developed in [Zidane *et al.* 2014].

[Kim *et al.* 2014] developed a specimen for a uniaxial tensile test based on trial and error which can provide heterogeneous stress states (Fig. 1.24). The authors analysed

four sample shapes using FFM technique and used the VFM to find the constitutive parameters of the Hill1948 yield criterion with Swift hardening law. It was concluded that the simultaneous identification of all anisotropic plastic parameters was reasonable only when the tests could offer enough heterogeneous information relevant to each anisotropic parameter. Geometry (d) offered some heterogeneous stress fields but did not provide enough information for each parameter. Therefore, the mentioned geometry by itself was unsuited for the simultaneous identification of all anisotropic parameters. Even though geometry (a) yielded very satisfactory identification results from the numerical simulation data, the sample tended to buckle in the experiments. Geometry (b) provided several heterogeneous stress states and the identification of the anisotropic parameters was carried out successfully. Geometry (c) provided biaxial stress states in the central area between the two holes and necking occurred at very early stages in the hole areas during the experiments, resulting in unsuccessful identification.

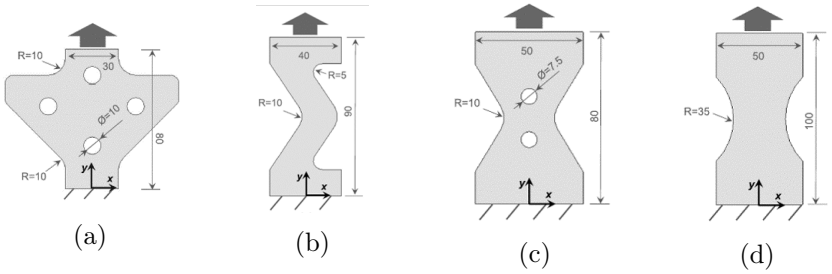

Figure 1.24: Specimen geometry (a), (b), (c) and (d) analysed by a uniaxial tensile test (dimensions in mm) presented in [Kim *et al.* 2014].

[Prates *et al.* 2014] proposed an inverse analysis methodology for determining the parameters of plastic constitutive models, using a biaxial tensile test on cruciform samples of sheet metals. The specimen was studied based on some geometric parameters, such as the fillet radius R, the L_1/L_2 ratio and the opening angle of the arms β. The aim was to select the values in order to cover as much as possible strain paths from uniaxial tension to biaxial tension in a balanced way, to maximise the strain value attained in the centre of the specimen while minimizing the stress concentration in the fillet region and ensuring a relatively high strain value in the centre of the specimen. The chosen geometry is presented in Fig. 1.25 and it accomplishes the previously mentioned objectives. The proposed identification approach was shown to be competitive with classical strategies, requiring only the measurement of the load evolutions during the biaxial tensile test of the cruciform specimen and the evaluations of the equivalent plastic strain distribution along the axes of the sample, at a given moment of the experiment.

[Liu *et al.* 2015] investigated the potential of the in-plane biaxial tensile test on the cross specimen for characterizing the hardening behaviour of metallic sheets under large strains. The authors proposed a cruciform specimen shape as presented in Fig. 1.26a and 1.26b. The sample was developed based on some literature review knowledge and numerical simulations of some geometry attempts. The authors considered relevant to determine the radius r of the thickness-reduced zone, the position D and radius R of the notches and the positions S_1 and S_2 of the slots. It was obtained parametrically the best set of parameters that lead to large strains in the thickness-reduced zone and small strains located in the notches and at slot ends.

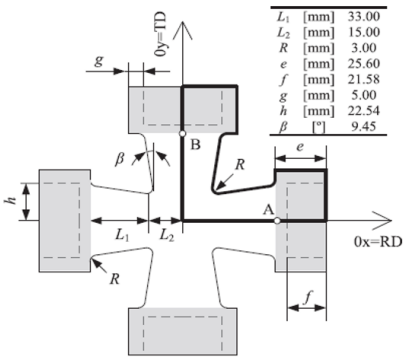

Figure 1.25: Geometry and dimensions in mm of the cruciform specimen considered in [Prates *et al.* 2014]. The grips, represented in grey, hold the specimen by grabbing it along the dashed grey lines.

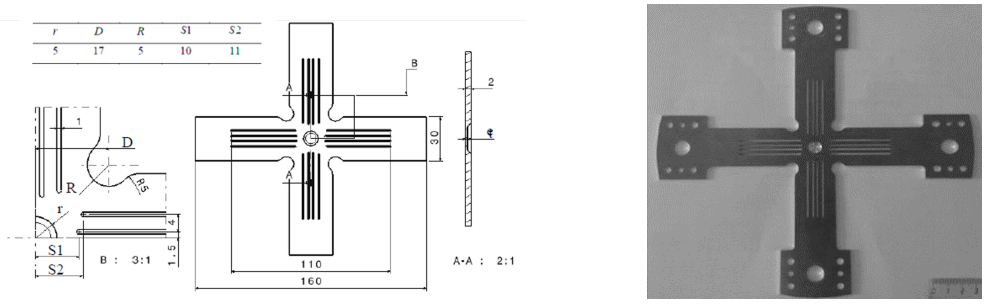

(a) (b)

Figure 1.26: (a) Sketch of the optimised cruciform specimen (dimension in mm) and (b) specimen machined explored in [Liu *et al.* 2015].

[Souto 2015] proposed a computational design of heterogeneous tests for material parameters identification using a shape optimisation method for the determination of the specimen's boundaries. In addition, the authors have proposed an indicator to rate and rank mechanical tests regarding the strain state range covered by the test, the deformation heterogeneity of the specimen and the strain level achieved up to rupture. It was generated the optimum shape of the specimen for a uniaxial tensile test as well as a biaxial tensile test, resulting in a butterfly-shaped sample and a cruciform specimen, respectively, as shown in Fig. 1.27. Concerning the uniaxial tensile test, the specimen exhibited a strain state range between simple shear to plane strain tension, for a one-step procedure, while the biaxial tensile test provided more mechanical information. The authors have also determined effectively the material parameters for complex phenomenological models involving many parameters.

Following on the previous research, [Souto *et al.* 2016] focused on the investigation of the design by optimisation using either Cubic Splines or B-Splines for characterisation of the specimen shape for a uniaxial tensile test. The resulting shapes are presented in Fig. 1.28. The authors proved that a specimen shape leading to a rich strain field information is achieved using B-Splines. However, the designs obtained show high strain gradients and stress intensification on the outer edges of the blank, which can result in

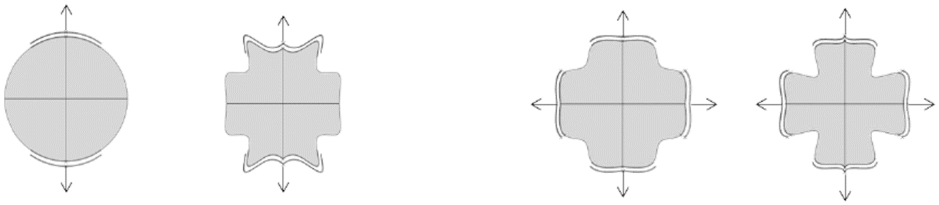

(a) Butterfly test. (b) Cruciform test.

Figure 1.27: Initial (left) and optimal (right) specimen shapes obtained by a design optimisation process with one step procedure using (a) 1 tool and (b) 2 tools analysed in [Souto 2015].

edge cracking in a real experimental test. It is proposed to adopt a constraint avoiding situations where the maximum stress is on the edges and preventing sharp concave radii in the optimisation problem.

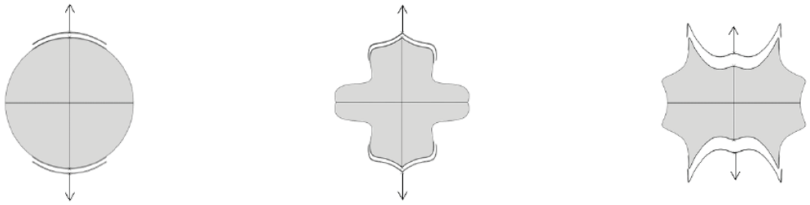

(a) (b) (c)

Figure 1.28: (a) Initial and optimal shapes using (b) Cubic Splines and (c) B-Splines presented in [Souto *et al.* 2016].

In order to minimise the cost function that provides the optimum heterogeneous specimen shape for a uniaxial tensile test, based on the indicator developed by [Souto 2015], [Andrade-Campos *et al.* 2019] investigated the best curve parametrisation and optimisation algorithm. Seven optimisation strategies were used, but only four of them were able to converge to a solution: the Nelder-Mead, pattern search, SDBOX, and CMA-ES. It was also determined the number of control points that minimises the cost function regarding the different curve parametrisation. The result was seven control points for B-splines and NURBS, and six for Splines. The specimen that was able to provide more mechanical information was obtained by using NURBS with CMA-ES. However, CMA-ES optimisation strategy can be considered as good as SDBOX, providing similar results and presenting a 10-times faster convergence. The resulting sample shows a butterfly shape, providing most strain states fitting in the neighbourhood of uniaxial tension due to the tensile load conditions of the test and the best solutions offered shear and uniaxial compression states for small values of strain. None of the tests was able to produce the biaxial strain state. Furthermore, not a unique test presented both the overall range of stress/strain and large levels of plastic strains.

[Aquino *et al.* 2019] made an experimental validation of the butterfly mechanical test proposed in [Souto *et al.* 2017] using a parameter identification framework. Due to machining constrains, the virtually designed butterfly test was adapted, resulting in a higher value of the heterogeneity indicator developed [Souto 2015]. However, there is

a measuring zone in the experiments smaller than the virtual one, resulting in loss of information and reduction of the indicator value. It was proved experimentally that the butterfly test does not show any plane strain information nor has privileged the anisotropy characterisation. Regarding the parameter identification, the results demonstrated that the solutions are dependent on the initial set of parameters, but the material behaviour is quite accurate compared to the experimental observations. Although, differences in the yield surface are visible.

[Jones *et al.* 2018] focused on identifying model parameters using VFM, which is based on the principle of virtual work. With the aim of maximise the stress heterogeneity and the range of strain rates, minimise large gradients in stress or strain near specimen edges, restrict the geometry to planar, while preventing buckling and ensure a uniaxial loading direction, the authors developed a new specimen geometry via an iterative process (Fig. 1.29). Starting from an initial shape selected by intuition, performing a finite element analysis and adjusting the design manually for the geometry to fit the criteria, a final capital letter "D" shape specimen was obtained. The numerical analysis showed a good heterogeneity of the stress field and the most probable stress states were tension along the vertical axis, with some amounts of biaxial and shear. Although this specimen did not cover all the possible strain states, it showed more strain heterogeneity than a standard dog bone sample before necking.

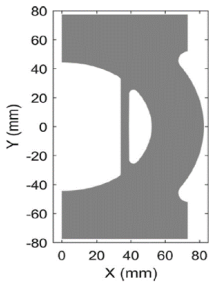

Figure 1.29: Geometry of the D-specimen used for model calibration with VFM in the work presented in [Jones *et al.* 2018].

A complex geometry of a heterogeneous specimen for a uniaxial tensile test was proposed by [Küsters and Brosius 2019] and it is represented in Fig. 1.30. The sample was studied to demonstrate the extended method for damage characterisation and provide a wide range of different stress conditions with only one experiment. They performed experimental tests on a universal tensile testing machine using DIC analysis for acquisition of the heterogeneous strain field distribution. The specimen presented mainly stress states between uniaxial tension and plane strain, in the plastic region and equi-biaxial tension stress state with very low plastic deformation.

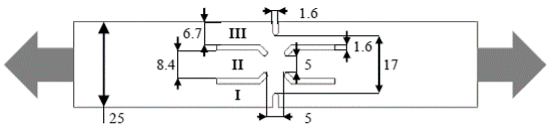

Figure 1.30: Geometry of the heterogeneous specimen (dimension in mm) proposed in [Küsters and Brosius 2019].

A finite element modelling coupled with the orthogonal design was used to evaluate the influence of some geometric parameters of a biaxial tensile test of a cruciform specimen by [Zhu *et al.* 2019]. Three specimen geometries (Fig. 1.31) were experimentally analysed, and the process was successfully validated. It was concluded that an inner chamfer is effective in reducing the degree of stress concentration and increase the homogeneous stress distribution in the centre region of the specimen and the thinning of the sample can restrict the plastic flow in the centre region.

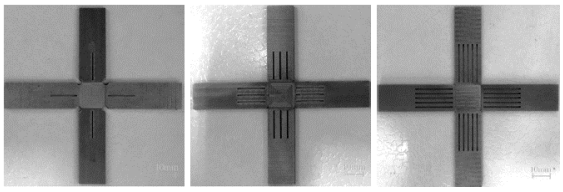

Figure 1.31: Three different specimens tested experimentally for validation of the geometry optimisation in [Zhu *et al.* 2019].

[Oliveira *et al.* 2020] proposed an indicator based on the principal direction associated with the maximum principal stress in absolute value and the material frame to evaluate the sensitivity of the mechanical tests to anisotropy. Three specimens from the literature [Belhabib *et al.* 2008, Kim *et al.* 2014, Jones *et al.* 2018] were virtually studied and qualitatively ranked in terms of heterogeneity by the use of the major and minor strain diagram, the major and minor stress diagram and histogram of rotation angle distribution, in function of the equivalent plastic strain. This work provides a good way to qualitatively classify heterogeneous tests. Although, a quantitative approach is necessary for a precise ranking.

It was proposed to use topology optimisation for the specimen design by [Chamoin *et al.* 2020]. The purpose was to find the geometry of a uniaxial tensile test sample that maximises the sensitivity of the measured displacement field to sought parameters, under volume fraction constrains and without any a priori information on the specimen shape. Numerical results and experimental validation have confirmed the method. The design obtained from the optimisation procedure (Fig. 1.32a) revealed a part of the specimen not linked to the remainder of the structure after filtering. For the experimental approach, the geometry suffered some adaptations due to manufacturing limitations and it is presented in Fig. 1.32b. This approach revealed a strong issue to face regarding the physical feasibility of some outcoming shapes. Hence, it is required further research on the machining capabilities, the smoothing of boundaries as well as the manufacturing constraints that could be introduced in the cost function. Topology optimisation was also used by [Barroqueiro *et al.* 2020] to design a new specimen for a tensile test. The obtained specimen presented pure shear, compression and tensile stress states in the plastic region. However, no experimental validation took place.

1.2.3 Commercial review

Regarding the material mechanical characterisation patents, [Knoxville *et al.* 2012] presented a method to characterise materials under multiple strains and strain states. Specimens (Fig. 1.33a) for measuring the behaviour of a material with only a single strain test, a system (Fig. 1.33b) and a method for characterizing material behaviour were in-

(a) (b)

Figure 1.32: (a) Sketch of the specimen geometry and (b) manufactured sample obtained using topology optimisation for a uniaxial tensile test developed in [Chamoin *et al.* 2020].

troduced. The new method, the specimen design and the testing procedure can produce continuously varying levels of plastic strain achieved at various locations in the specimen and at different strain rates [Knoxville *et al.* 2012].

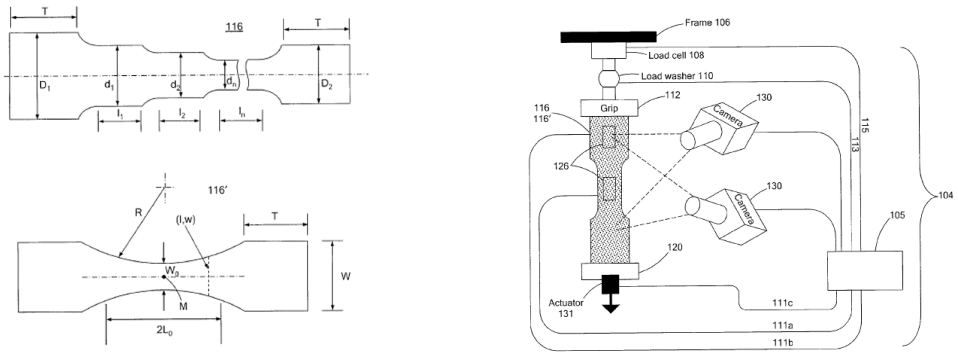

(a) (b)

Figure 1.33: (a) Sketch of the specimens to be used with the (b) measuring system presented in [Knoxville *et al.* 2012].

The invention held by [Hanabusa 2014] relates to a tensile testing machine used for a biaxial tensile test of thin sheet material and is shown in Fig. 1.34a. Using a uniaxial tensile testing device, it is performed a synchronised tensile test in four directions along two axes perpendicular to each other. The main advantages are the simplification of the structure of the device and the reduced number of components required.

A type of cruciform specimen was patented in [Yulong 2015] to apply in a thermal environment with a biaxial tensile loading. This way, the centre region of the sample is subjected to large deformations.

Regarding the commercial point of view, there are no heterogeneous mechanical test specimens nor specific equipment available for acquisition. This area is still on scientific development. Though, there are universal uniaxial testing machines available that can perform uniaxial tensile test on non-standard specimen geometries if the sample has specific attributes. Hence, it is appropriate to develop sample designs capable of being tested on this type of machines.

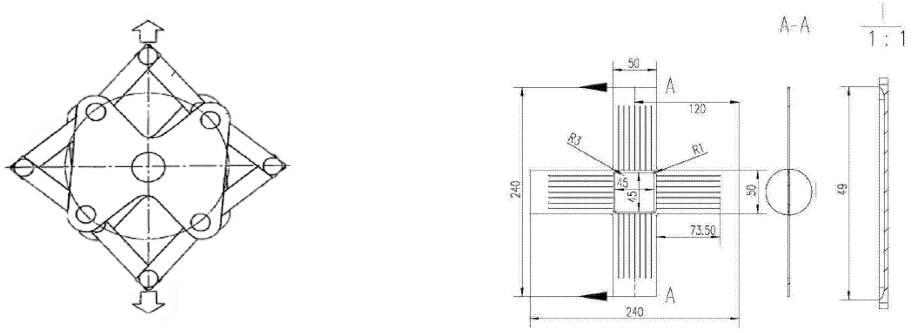

(a) (b)

Figure 1.34: Sketches illustrating (a) the biaxial tensile testing machine of the invention in [Hanabusa 2014] and (b) the cruciform specimen for thermal environment testing introduced in [Yulong 2015].

1.3 Discussion and proposed solution

More complex mechanical tests, providing different stress and strain fields are required for a better material parameter identification and thus, a more precise material behaviour numerical prediction. Complexity can be introduced thanks to non-standard specimen geometries, complex loading conditions or a combination of both.

Many scientific advances on the specimen's geometry were due to trial and error on uniaxial loadings as well as biaxial loadings, generating heterogeneous strain fields. These advances were mainly based on uniaxial tests on perforated specimens, notched specimens, shear-like tensile zones on samples and other more complicated shapes. Regarding the biaxial loading, much research has been done on cruciform shaped samples with plenty of differences on some geometrical parameters as well as introducing perforations. Concerning the optimisation approaches, interesting studies have been made using shape optimisation of the specimen outer boundaries in [Souto 2015] and also topology optimisation in [Chamoin *et al.* 2020] and [Barroqueiro *et al.* 2020].

Regarding the reliability on heterogeneous mechanical test for the material parameter identification, numerical prediction and simulation of materials, its success was proved in [Kajberg and Lindkvist 2004, Cooreman *et al.* 2008, Cooreman 2008, Pottier *et al.* 2011, Pottier *et al.* 2012, Kim *et al.* 2014, Prates *et al.* 2014, Souto 2015, Zhang *et al.* 2015, Jones *et al.* 2018]. It was concluded in [Cooreman *et al.* 2008, Pottier *et al.* 2012, Prates *et al.* 2014] that parameter identification from heterogeneous specimens outcomes the one using classical homogeneous tests, such as uniaxial tensile test. Experimental procedures performed in [Belhabib *et al.* 2008, Güner *et al.* 2012, Aquino *et al.* 2019, Küsters and Brosius 2019, Zhu *et al.* 2019, Chamoin *et al.* 2020] on this type of specimens also demonstrated its reliability. In [Pottier *et al.* 2011] was demonstrated that, regarding the deep-drawing validation, the quality of the shape prediction increases with the strain field heterogeneity. Furthermore, it was proved in [Cooreman 2008] that heterogeneous mechanical tests can reduce the number of the required experimental classical tests for the material parameter identification.

The work developed in [Souto 2015, Souto *et al.* 2016, Andrade-Campos *et al.* 2019,

Aquino *et al.* 2019] generated an experimentally validated butterfly-type specimen for uniaxial loading using shape optimisation of the contours. It was also created a cruciform-type specimen for a biaxial loading using the same approach. The butterfly sample virtually exhibits strain state range between simple shear to plane strain tension and experimentally similar results, but without plane strain. It also revealed poor anisotropy characterisation and limitations due to the symmetries of the design. However, this specimen has problems related to the slipping of the grips, due to the irregularity of the boundaries. Besides, the irregular geometry of the outer boundaries cannot be analysed via DIC because of the smaller region of interest, thus strain measurements near the edges of the sample are not possible. Moreover, loss of mechanical information occurs for the exact same reason. A big advantage is the possibility of performing the experiment in a universal tensile test machine, on contrary of the cruciform specimen obtained by the same method. Although, the cruciform specimen shape provides finer mechanical information.

The present work aims to design a uniaxial tensile load test that presents heterogeneous strain paths using shape optimisation methods. However, the design shape is limited to the specimen's interior notch. The outer boundaries of the sample are rectangular, which can be simply tested in a standard tensile test machine, reducing the sliding of the grips. Besides, the specimen has two symmetries assuring the balance during the experimental test. The proposed solution is expected to reduce the number of evaluations of mechanical tests and, consecutively, acquire higher quality on numerical simulations of the materials due to better parameterisation of complex constitutive models. A uniaxial tensile virtual test of the specimen is held up to rupture with a continuous loading path. Curve parametrisation of the specimen's perforation is considered as design variable that generates the larger amount of mechanical information. An indicator which rates the strain field of the experiment by quantifying mechanical information will be part of the cost function of the optimisation procedure. For every defined geometry, this indicator is calculated in order to seek for the most inhomogeneous material behaviour solution with greater strain intensities. A suitable optimisation algorithm which provides a good relation between efficiency and precision is applied to find the best solution. ABAQUS software [Dassault Systèmes 2014] and Python [Python Software Foundation 2020] scrips are used to simulate the numerical behaviour of the specimen in specific conditions and to hold the optimisation formulation and algorithm.

1.4 Reading guidelines

This work is divided into four parts. The first part presents the framework and motivation, literature reviews, such as the scientific, commercial and industrial review, proposed solution, and reading guidelines. The second part of this work is related to the methodology used and its implementation. It involves the general methodology, the optimisation problem formulation, and the solution's evaluation. Concerning the implementation and the numerical simulation procedure, it is presented the specimen's dimension and curve definition, the material characteristics, the boundary conditions applied, the finite element mesh implemented, and the rupture criterion used. Besides, it is mentioned the optimisation algorithm and the initial solution used in the optimisation procedure. It is presented in the third part the finite element type and dimension analysis and its con-

clusions, as well as the reference solution used for further comparisons. In the same part, several parameters' dependency analysis is performed, to find the best combination of them. It is studied the objective function and the heterogeneity criterion, the boundary conditions, the number of curve control points, the specimen's height/width ratio, the initial solution, and the optimisation algorithm. In addition, it is also presented the results that outcome from the combination of the best parameters and the three better solutions are highlighted. The last part is related to the conclusions and suggestions for future works.

Chapter 2

Methodology and implementation

2.1 General methodology, problem formulation and solution's evaluation

An iterative process was used to design by optimisation the heterogeneous specimen, as depicted in Fig. 2.1. The process starts by defining the design variables of the optimisation procedure. These design variables are the radial coordinate of the points that define the interior notched specimen shape. For the definition of the specimen shape, different curve parametrisations can be used. The specimen outer contours are established and constant during the process. The uniaxial tensile-load test is simulated, and the resulting strain and stress states and fields are evaluated using a heterogeneity criterion. This criterion is used as objective function in the optimisation procedure that generates new design variables for another evaluation, until convergence is obtained. The best solution is a shape of the interior notched specimen that generates large number of heterogeneous strains and stress states during the test until rupture.

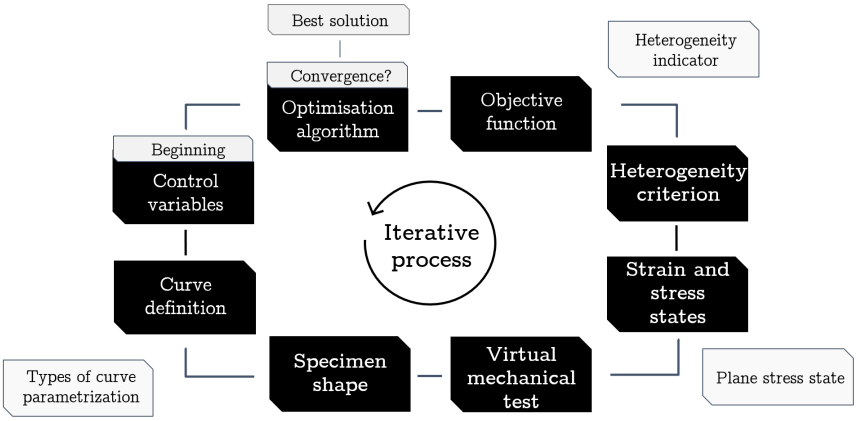

Figure 2.1: Iterative process methodology for the design of the heterogeneous specimen.

Regarding the problem formulation, the iterative process aims to maximise the heterogeneity of the specimen, by varying the shape of the curve. The interior notched curve is defined by n control points, as shown in Fig.2.2a. The location of the control points

are the design variables.

Also, for the reduction of optimisation variables number, only the radial coordinate of the curve was considered as design variables. The angular space was equally split for the number of control and fixed points, as shown in Fig.2.2b and a search space was defined.

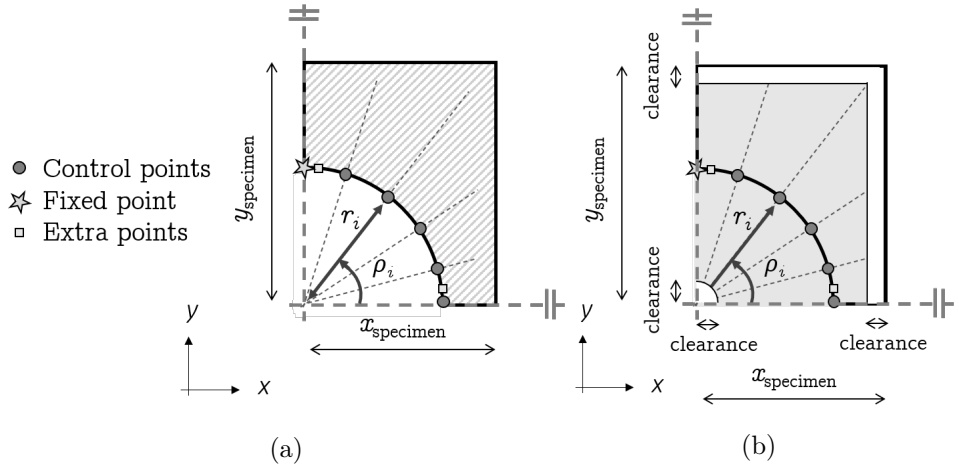

Figure 2.2: Representation of the specimen perforation and (a) its curve control points and (b) their search space.

Therefore, the aim is to find $\mathbf{r} = [r_i]$, with $i = 1, \ldots, n$, that maximises the specimen's heterogeneity (H), and can be formulated as:

$$\begin{aligned} \text{Max:} \quad & H(\mathbf{r}, \mathbf{u}) \\ \mathbf{r} \in \; & \mathbb{R}^n \\ \text{subjected to:} \quad & \\ & r_i^{\min} \leq r_i \leq r_i^{\max}, \text{with } i = 1, ..., n \\ & \mathbf{K} \cdot \mathbf{u} = \mathbf{F}. \end{aligned} \tag{2.1}$$

Every time a solution is defined, it is evaluated in terms of stress and strain heterogeneity. It is required a way to quantify and rank the specimen's heterogeneity. Considering that there is no heterogeneity criterion standardisation, its definition is necessary.

To analyse the mechanical test's richness, the strain or the stress states can be used (Fig. 2.3). The strain states are defined using the minor and major strain ratio ($\frac{\varepsilon_2}{\varepsilon_1}$), whereas the stress states are calculated concerning the ratio between the minor and major stresses ($\frac{\sigma_2}{\sigma_1}$). This way it is possible to identify the strain and stress states in the specimen's sheet plane. In sheet metal forming processes, the most common observed strain and stress states are the equibiaxial tension, plane strain tension, uniaxial tension, shear, and less commonly uniaxial compression [Oliveira *et al.* 2020]. On Tab. 2.1 there are the strain and stress states defined with the ratio intervals, for an isotropic material. In the work, it is considered that more and different strain and stress states will outcome in a more heterogeneous mechanical test and, therefore, a more rich test.

Besides, it is also necessary to perform mechanical tests with high strain levels in a large specimen region. The equivalent plastic strain ($\overline{\varepsilon}^{\mathrm{P}}$) is a standard indicator par-

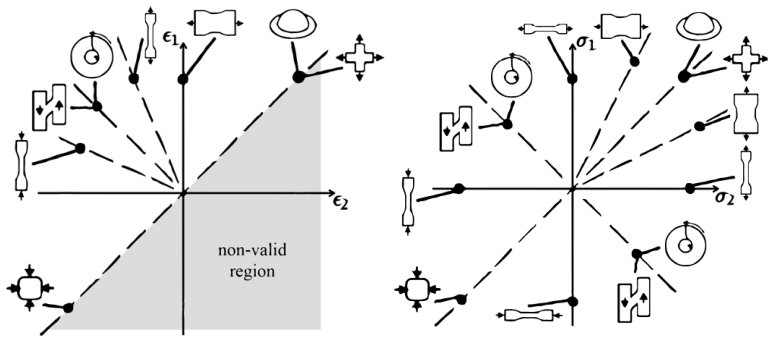

(a) (b)

Figure 2.3: An overview of mechanical tests for material characterisation of sheet metal forming processes on (a) major and minor strain, and (b) major and minor stress diagrams [Oliveira *et al.* 2020].

Table 2.1: Main strain and stress states observed in mechanical tests for material characterisation of sheet metal forming processes, for an isotropic material [Oliveira *et al.* 2020].

	Strain	**Stress**
Equibiaxial tension	$\frac{\varepsilon_2}{\varepsilon_1} = 1;\ \varepsilon_2 > 0;\ \varepsilon_1 > 0$	$\frac{\sigma_2}{\sigma_1} = 1;\ \sigma_2 > 0;\ \sigma_1 > 0$
Plane strain tension	$\varepsilon_2 = 0;\ \varepsilon_1 > 0$	$\frac{\sigma_2}{\sigma_1} = \nu;\ \sigma_2 > 0;\ \sigma_1 > 0$
Uniaxial tension	$\frac{\varepsilon_2}{\varepsilon_1} = 0.5;\ \varepsilon_2 < 0;\ \varepsilon_1 > 0$	$\sigma_2 = 0;\ \sigma_1 > 0$
Pure shear	$\frac{\varepsilon_2}{\varepsilon_1} = -1;\ \varepsilon_2 < 0;\ \varepsilon_1 > 0$	$\frac{\sigma_2}{\sigma_1} = -1;\ \sigma_2 < 0;\ \sigma_1 > 0$
Uniaxial compression	$\frac{\varepsilon_2}{\varepsilon_1} = -2;\ \varepsilon_2 < 0;\ \varepsilon_1 < 0$	$\sigma_2 < 0;\ \sigma_1 = 0$

ticularly important to measure the level of plastic strain reached during the mechanical tests [Oliveira *et al.* 2020].

So, a heterogeneity indicator should benefit solutions with different strain and stress states, as well as large equivalent plastic strain in every state.

In this investigation, three different heterogeneity indicators where analysed. The first is an adaptation of the heterogeneity criterion used in [Souto 2015]. Instead of evaluating continuously the specimen strain and stress fields until rupture, it was only analysed the moment just before rupture. So, the equation terms were only evaluated at the end of the test. This simplification was made since almost all cases considered in [Souto 2015] showed that the equivalent plastic strain and strain state standard deviation reached its larger values at the end of the test. Besides, it was also proved in [Souto 2015] that the equivalent plastic strain distribution increases along the test, and the strain state distribution is almost constant along time, due to linear strain paths. Besides, the maximum equivalent plastic strain of the test is achieved at the end of it, as well as the average deformation. Therefore, the indicator used is given as:

$$I_{\mathrm{T1}} = w_{\mathrm{r1}} \cdot \frac{\mathrm{Std}(\varepsilon_2/\varepsilon_1)}{w_{\mathrm{a1}}} + w_{\mathrm{r2}} \cdot \frac{(\varepsilon_2/\varepsilon_1)_{\mathrm{R}}}{w_{\mathrm{a2}}} + w_{\mathrm{r3}} \cdot \frac{\mathrm{Std}(\bar{\varepsilon}^{\mathrm{P}})}{w_{\mathrm{a3}}} + w_{\mathrm{r4}} \cdot \frac{\bar{\varepsilon}^{\mathrm{P}}_{\mathrm{MAX}}}{w_{\mathrm{a4}}} + w_{\mathrm{r5}} \cdot \frac{Av_{\bar{\varepsilon}^{\mathrm{P}}}}{w_{\mathrm{a5}}} \quad (2.2)$$

The mention indicator has in consideration the strain state range ($(\varepsilon_2/\varepsilon_1)_{\mathrm{R}}$), the strain state standard deviation ($\mathrm{Std}(\varepsilon_2/\varepsilon_1)$), the equivalent plastic strain standard deviation ($\mathrm{Std}(\bar{\varepsilon}^{\mathrm{P}})$), the mean of each strain state maximum equivalent plastic strain and maximum equivalent plastic strain of the test ($\bar{\varepsilon}^{\mathrm{P}}_{\mathrm{MAX}}$) and the average deformation ($Av_{\bar{\varepsilon}^{\mathrm{P}}}$). These terms have relative weights ($w_{\mathrm{r1}}, w_{\mathrm{r2}}, w_{\mathrm{r3}}, w_{\mathrm{r4}}, w_{\mathrm{r5}}$) and absolute values ($w_{\mathrm{a1}}, w_{\mathrm{a2}}, w_{\mathrm{a3}}, w_{\mathrm{a4}}, w_{\mathrm{a5}}$) for the terms adjustment of importance and normalisation. The maximum possible value achieved by the indicator is 1. For this indicator, the cost function to be minimised is $CF_{\mathrm{T1}} = 2 - I_{\mathrm{T1}}$ and the used relative weights and absolute values are indicated on Tab. 2.2. These were adjusted in order to improve the optimisation results. An importance increase of the terms concerning the strain level group promoted the global deformation of the specimen and reduce premature strain localisation effects [Souto *et al.* 2017].

Table 2.2: Absolute values and relative weights used in the indicator I_{T1} having in consideration [Souto *et al.* 2017].

w_{a1}	w_{a2}	w_{a3}	w_{a4}	w_{a5}	w_{r1}	w_{r2}	w_{r3}	w_{r4}	w_{r5}
1	4	0.25	0.8	0.4	0.13	0.02	0.25	0.35	0.25

The second indicator used was an adaptation of the one proposed in [Barroqueiro *et al.* 2020]. The original indicator was developed and used for a topology optimisation method and had in consideration the numerical elements' density (ρ_e) that was replaced by the elements' volume (V_e) in this work. It benefits solutions with less stress concentrations, and can be written as:

$$I_{\mathrm{T2}} = \prod_{s=1}^{3} \frac{3}{\sum_{e=1}^{n} V_e} \cdot \sum_{e=1}^{n_e} \left(\delta_e^s \cdot Z_e \cdot V_e\right), \quad (2.3)$$

where s denotes indexes defined in Eq. 2.6, corresponding to a stress state. In this case, 1, 2, and 3 indicate compression, shear, and tension strain states, respectively. The total

element's number (n_e) are analysed, either under plastic or elastic deformation. The term Z_e penalizes solutions with stress concentrations and non-stressed material (Fig. 2.4a), given as:

$$Z_e = \frac{1}{1 + (b \cdot \sigma_e^*)2}, \tag{2.4}$$

where b is a constant for the penalisation "aggressiveness" (fixed as 3) and σ_e^* is calculated as:

$$\sigma_e^* = \frac{\sigma_e^{\mathrm{VM}} - \overline{\sigma}^{\mathrm{VM}}}{\overline{\sigma}^{\mathrm{VM}}}. \tag{2.5}$$

The subscript VM refers to von Mises and $\overline{\sigma}^{\mathrm{VM}}$ is the mean stress. The operator δ_e^s filters the elements correspondent to the s stress state [Barroqueiro *et al.* 2020]. In order to identify the referred stress state of each element, the principal strains are used (see Fig. 2.4b) [Barroqueiro *et al.* 2020]. The referred operator (δ_e^s) takes approximately the value of one if the element is in the s stress state and zero otherwise. This is achieved via a 2D generalization of the smooth Heaviside function, being formulated as:

$$\delta_e^s = \begin{cases} \frac{1}{2} \cdot (1 - \tanh(\beta \cdot (\varepsilon_e^{11} + 0.75 \cdot \varepsilon_e^{22}))), & s = 1 \\ \frac{1}{4} \cdot (1 + \tanh(\beta \cdot (\varepsilon_e^{11} + 0.75 \cdot \varepsilon_e^{22}))) \cdot (1 - \tanh(\beta \cdot (\varepsilon_e^{11} + 1.5 \cdot \varepsilon_e^{22}))), & s = 2 \\ \frac{1}{2} \cdot (1 + \tanh(\beta \cdot (\varepsilon_e^{11} + 1.5 \cdot \varepsilon_e^{22}))), & s = 3. \end{cases} \tag{2.6}$$

In order to facilitate the reader's interpretation of the operator, a graphical representation is provided in Fig. 2.5, with a 3D representation as well as its projection (2D) in the principal strain plane [Barroqueiro *et al.* 2020].

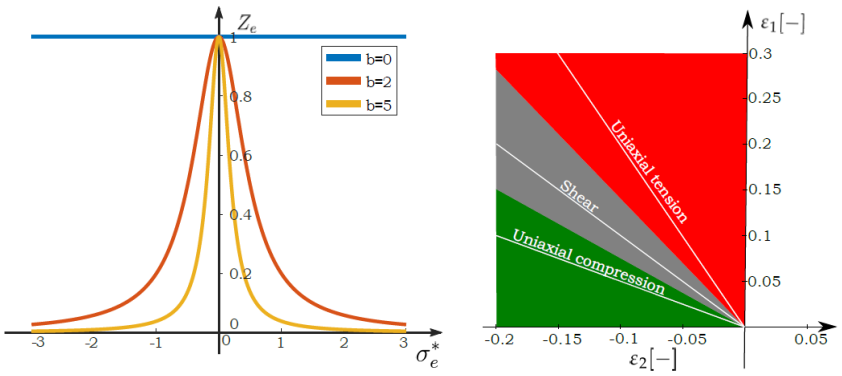

(a) (b)

Figure 2.4: (a) Von Mises stress penalisation function representation and (b) stress state identification via principal strains [Barroqueiro *et al.* 2020].

The larger is the indicator I_{T2}, the more heterogeneous is the solution. So, the cost function to be minimized is $CF_{\mathrm{T2}} = -I_{\mathrm{T2}}$.

The third indicator studied was another adaptation to the indicator proposed in [Barroqueiro *et al.* 2020]. Instead of evaluating the stress concentrations, it was taking

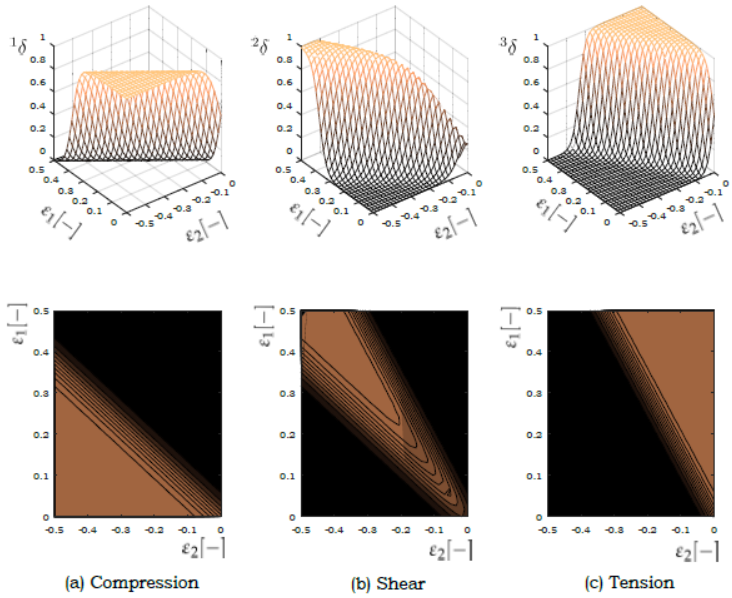

Figure 2.5: Graphical representation of the operator δ_e^s [Barroqueiro *et al.* 2020].

into consideration the equivalent plastic strain value of each element, using:

$$I_{\mathrm{T3}} = \prod_{s=1}^{3} \frac{3}{\sum_{e=1}^{n} V_e} \cdot \sum_{e=1}^{n_e} \left(\delta_e^s \cdot \bar{\varepsilon}^{\mathrm{P}}_{\mathrm{MAX}_e} \cdot V_e \right). \tag{2.7}$$

The goal of this indicator is to benefit solutions with larger equivalent plastic strain values and strain state diversity. The remaining equation's terms were evaluated similarly to the indicator I_{T2}. The cost function to be minimized is $CF_{\mathrm{T3}} = -I_{\mathrm{T3}}$.

2.2 Implementation and numerical simulation procedure

A more detailed flowchart of the iterative optimisation process is depicted in Fig. 2.6. The optimisation variables are initialised using polar coordinates to define the radial distance to the centre of the specimen, while it is imposed an equal angular spacing between the points and a variable transformation technique is used for the normalisation and limit restriction. For the variable normalisation and boundary constraint, a variable transformation technique is applied [Andrade-Campos *et al.* 2015].

Then, these variables are converted to cartesian coordinates values, and the extra and fixed points are introduced for writing a complete spline's coordinates on a text file. A fixed point is introduced for giving another point to the curve and at the same to reduce the number of optimisation variables. It is assumed that the shape obtained at the end of the optimisation procedure can be scaled up or down without loss of information. This simplification is made having into consideration a variable dependency analysis on the specimen's height/width ratio. To make sure that the curve C^1 continuity or even C^2 continuity are established in the FEA specimen symmetries, extra points were introduced just next to the first and last points of the spline. Having two consecutive points in the same direction is expected to produce a spline's first and second continuous derivatives.

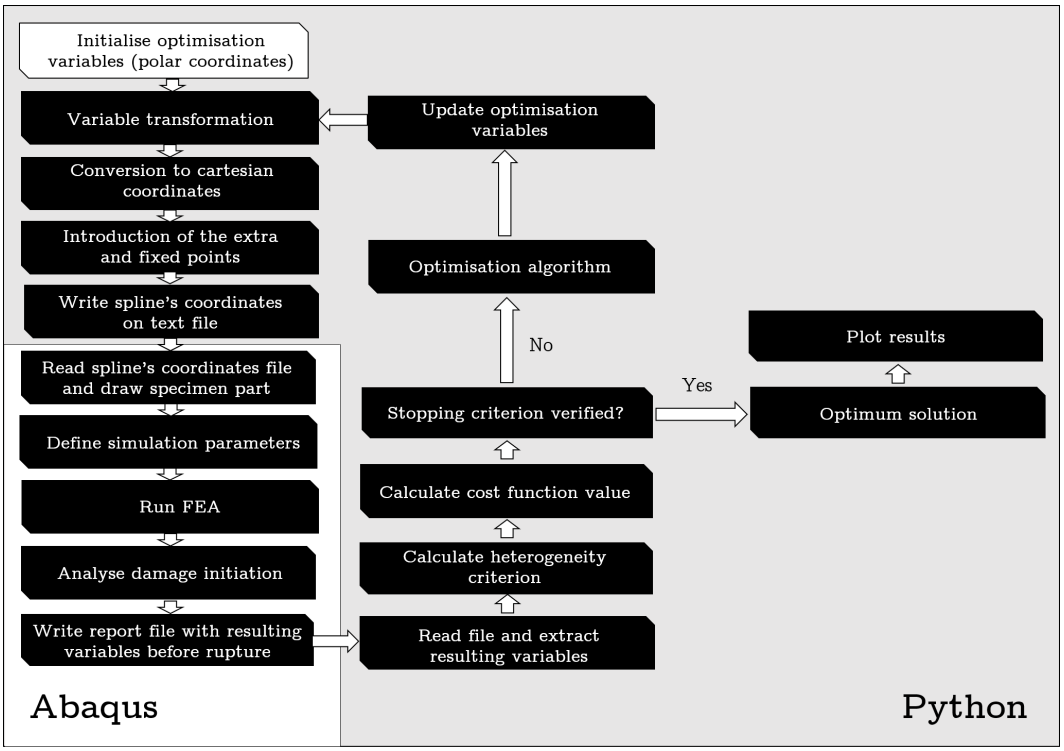

Figure 2.6: Design by optimisation procedure flowchart.

These points are introduced based on the numerical element size, just horizontally next to the fixed point and vertically to the last control point. The spline's coordinates file is read and the specimen part is drawn in Abaqus, and all the simulation parameters are introduced. The finite element analysis (FEA) analysis is submitted, and the damage initiation is analysed to write a report file at the moment just before rupture occurs. The report file presents the results necessary for the solution's evaluation. It is analysed using Python scripts and the heterogeneity criterion is calculated. The iterative process continues until the stopping criterion is verified and the optimum solution is achieved, terminating with the results charting.

2.2.1 Specimen geometry: dimensions and curve definition

Some numerical analysis simplifications were made to reduce the computational time. Only $\frac{1}{4}$ of the sample was modelled, considering symmetric and plane stress conditions. There were used two symmetries, one along the xx axis and another along the yy axis. Although, having no symmetries might have created a more heterogeneous specimen, since the optimisation procedure could originate a non-symmetric sample, with a different interior notched shape. It would require the quadruple number of control points and of numerical elements. This would increase considerably the optimisation procedure elapsed time. A non-linear quasi-static analysis is staged with a vertical displacement enough to break the sample.

Considering the uniaxial standard tensile test machine, a outer rectangular shape was considered for the specimen. The specimen dimensions initially used in the FEA analysis

are depicted in Fig. 2.7.

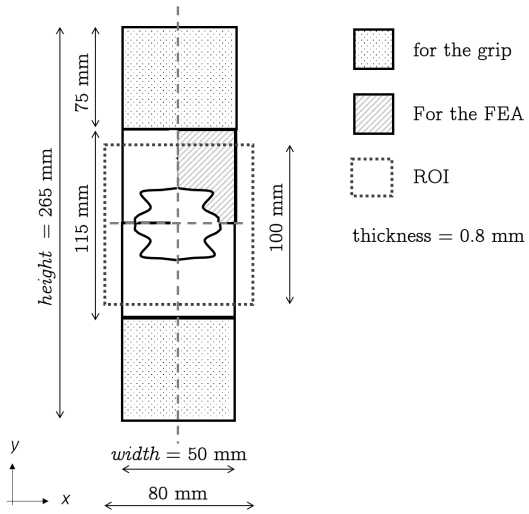

Figure 2.7: Specimen overall dimensions.

The sample's top and bottom parts are used for the grips and not considered for the numerical analysis since the strain and stress states cannot be analysed experimentally in that location. These dimensions were chosen having in consideration the standard tensile testing specimen's dimensions and the DIC camera attributes, such as the size of the region of interest (ROI). It was preferred a smaller height/width ratio than the standard tensile test specimen, giving more freedom for the algorithm to generate the curves. Bearing in mind that is assumed to have no loss of information with the specimen's size scaled up or down, these dimensions are merely indicatives. Thus, it is given more importance to the height/width ratio, which in this case is $\frac{265}{50} = 5.3$. The Abaqus software has a spline tool to calculate the shape of the curve using a cubic spline fit between all points along the spline; besides, the first and second derivatives of the spline are continuous [Dassault Systèmes 2014]. This was the technique used for the specimen perforation curve definition since it is easy to implement, has a small number of defining parameters, and shows enough flexibility. More complex curve parametrisation could be used, but it would involve having more design optimisation variables to deal with. Increasing the number of curve parameters implies increasing the computational time required for the optimisation process.

2.2.2 Material behaviour

It was specified an elastoplastic material, using the Swift hardening law. To account for damage, the material's forming limit diagram was used. A dual-phase steel (DP600) was specified for the specimen numerical simulation. The DP600 steel elastic properties: Young Modulus (E) and poisson's ratio (ν); as well as the Swift hardening law's parameters (K, σ_0 and n) are specified in Tab. 2.3.

To evaluate the range of specimen's strain and stress paths the Abaqus' forming limit diagram (FLD) (Fig. 2.8a) was used as rupture criterion. The deformation state is

Table 2.3: DP600 steel elastic properties and Swift hardening law's parameters [Ozturk *et al.* 2014].

Elastic		**Plastic**		
E (GPa)	ν	K (MPa)	σ_0 (MPa)	n
210.0	0.3	979.46	355.0	0.194

determined by [Dassault Systèmes 2014]:

$$\omega_{\text{FLD}} = \frac{\varepsilon_{\text{major}}}{\varepsilon^{\text{FLD}}_{\text{major}}(\varepsilon_{\text{minor}}, \theta, f_i)}, \tag{2.8}$$

as a function of the current deformation state and is defined as the ratio of the current major principal strain ($\varepsilon_{\text{major}}$), to the major limit strain on the forming limit curve (FLC) ($\varepsilon^{\text{FLD}}_{\text{major}}$) evaluated at the current values of the minor principal strain ($\varepsilon_{\text{minor}}$), temperature ($\theta$) and predefined field variables (f_i) [Dassault Systèmes 2014].

The DP600 steel forming limit curve is defined by the experimental data depicted in Fig. 2.8b. The damage initiation is verified when $\omega_{\text{FLD}} = 1$.

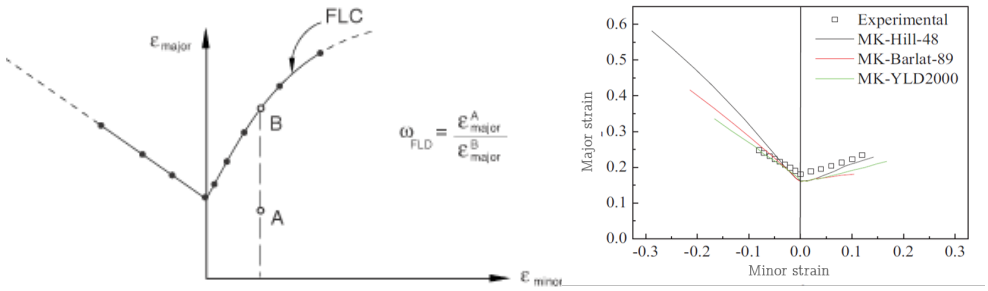

(a) (b)

Figure 2.8: Forming limit diagram (a) for damage initiation criterion [Dassault Systèmes 2014] and (b) referring to DP600 steel specifications [Ozturk *et al.* 2014].

2.2.3 Boundary conditions and finite element mesh

The displacement required for the virtual uniaxial tensile test is the one enough to break the specimen. It depends on the material used, as well as the sample's geometry. It was numerically analysed the minimum displacement required for the specimen rupture with the smallest perforation possible. The conclusion was that it is only necessary about 2 % of the specimen height, to reach rupture of the sample, which is approximately 5.3 mm of vertical displacement.

The numerical mesh is automatically defined whenever a new solution is evaluated in the design by optimisation procedure. It is used a non-parametric mesh with two seeded edges, depicted in Fig. 2.9. The element size and type were further evaluated in terms of dependency on the results.

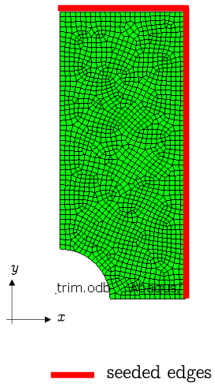

Figure 2.9: Seeded edges for the mesh definition (element edge dimension of 1 mm).

2.3 Optimisation algorithm and procedure

The design problem here defined is non-linear, with continuous optimisation variables that are within a minimum and maximum values. To impose the variables domain, it is used a variable transformation, as mentioned before. Thus, it is considered a problem with no constraints. The cost functions used are also non-linear.

There are two types of algorithms for non-linear optimisation problems: in the direct search algorithms, that only use the information about the cost function evaluation to find the optimum solution. These techniques require a large number of evaluations but can better search the variables domain. Heuristics, meta-heuristic, or classical direct search methods are examples of this type of algorithms and the other kind of algorithms is based on the function's gradient to find the direction of search. These are more efficient and ensure the local minimum finding for convex and differential functions.

Since it is not possible to know the cost function's gradient of this problem, a direct search algorithm must be used. The stopping criterion of this type of algorithm is based on the cost function and optimisation variables variation.

The Nelder-Mead simplex algorithm was selected for this problem's first approach since it revealed a good performance in a similar optimisation problem in [Souto 2015]. It was used SciPy Python's library for its implementation. The algorithm is based on the n-dimensional space geometric properties to find the best solution. The simplex is a geometric figure formed by $n + 1$ vertices of an n dimensional space. Each vertex is a possible solution to the optimisation procedure. The optimisation procedure iterative evolution is defined by the $n + 1$ simplex vertices cost function value comparison and its gradual movement in direction to the minimum. The simplex movement is based on three operations: reflection, expansion, and contraction. These are used to replace the point with the larger cost function value by a new one [Andrade-Campos *et al.* 2015]. In the first iteration, the $n + 1$ solutions are analysed. Then, for each iteration, only one or two evaluations are required. Due to the starting-point dependence of this problem, different initial solutions are going to be further analysed to find the one that reaches a better final solution. A multi-starting method is a solution to avoid local minimums.

Chapter 3

Analysis and results

3.1 Element dimension dependency analysis

The numerical elements dimension is crucial for the quality of the FEA results. On the overall, a larger number of elements (finer mesh) would outcome in more accurate results. Although, with a smaller element dimension, the computational time required for the numerical simulation analysis is way higher. It is necessary to have a compromise between the quality of the results and the simulation's elapsed time.

It was noticed that for a 1 mm vertical displacement imposed, when the specimen's interior notch area increases, the maximum equivalent plastic strain (PEEQ) obtained also increases. This was expected since when the specimen area decreases, the stress and strain become larger. The element dimension dependency was analysed with this test with a 1 mm specimen thickness.

It was used a free mesh with 2 seeded edges with a 4-node bilinear plane stress quadrilateral with reduced integration and hourglass control element. All the 5 control points were increased gradually and equally with a perturbation depending on the element edge size, while the fixed point was kept in place. Some solutions are presented in Fig. A.1, for better understanding. It was tested the element dimensions of 1 mm, 0.8 mm, 0.5 mm, 0.3 mm, 0.2 mm and 0.1 mm as presented in Fig. A.2. The element size dependency results are plotted in Fig. 3.1a. The maximum equivalent plastic strain values of each solution were normalised by the highest equivalent plastic strain of all solutions, while the control points position was normalised by the value of the fixed point (10 mm). The number of analysed solutions with 0.1 mm was reduced due to the computational time required for the study. In this case, it was used 1 mm as a control point's position perturbation.

The reached curves nearly follow a fourth-degree polynomial and by comparison to the obtained data, it can be noticed the solutions' noise. This noise is verified in all the considered element dimensions.

Besides, the solutions with larger element edge dimensions show lower equivalent plastic strain, while the solutions with smaller element dimensions present larger strain. This fact can be due to the strain concentration at one element with a smaller area when refining the mesh. In terms of absolute value, the maximum equivalent plastic strain obtained in all the solutions studied was 0.310 and it is the result of the solution with 1.6 control points normalised position for the element dimension of 0.1 mm (Fig. A.3). More accurate results are achieved when using a smaller element edge dimension.

The computational time per evaluation required for the analysis of each solution is plotted in Fig. 3.1b.

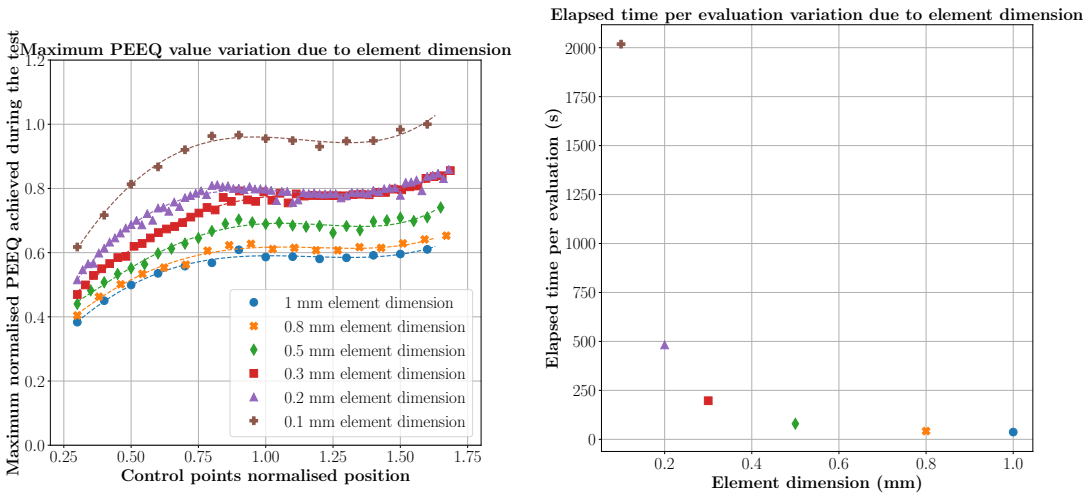

(a) (b)

Figure 3.1: (a) Maximum normalised equivalent plastic strain achieved during the test with the different control points' position and (b) its required computational time due to element edge dimension variation.

It is noticed a large variation of the elapsed time per evaluation, depending on the element dimension. The smaller the element edge dimension, the larger is the elapsed time per evaluation. For the solutions with an element edge dimension smaller than 0.3 mm, the required time for each solution is more than 250 seconds. The following analyses adopt the element edge dimension of 0.3 mm, since it finds a relatively accurate solution, with little noise within an acceptable computational time. Although, it must be kept in mind that the results of this process are still element size-dependent and future error can be due to it. These errors can be associated with the heterogeneity criterion evaluation as well as the specimen spline drawing.

3.2 Element type dependency analysis

The stress and strain outputs are evaluated in the numerical elements' integration points. Different element types can influence the numerical simulation results, so it is necessary to study its dependency. In the overall, an element type with more integration points will require more computational time for the solution's evaluation.

The numerical elements investigated in this analysis were CPS4R, CPS4, and CPS8R, depicted in Fig. B.1. CPS4 is a four-node bilinear plane stress quadrilateral with complete integration, having 4 integration points. CPS4R is a similar numerical element but has a reduced integration method and hourglass control. It has just one integration point and is expected to take less computational time for the numerical evaluation than the CPS4. CPS8R is an eight-node quadrilateral with four integration points.

It was adopted an element dimension of 0.3 mm and a dependency analysis similar to section 3.1 was performed, but this time, varying only the element type. The results

obtained are depicted in Fig. 3.2a.

The curves are also near a fourth-degree polynomial, showing similar behaviour as before. CPS4 results reveal a lot of noise when varying the control points position. CPS4R and CPS8R show similar behaviour in terms of variation, but different absolute values. It is noticed some noise in both solutions, but CPS8R reaches larger equivalent plastic strain values. Concerning the elapsed time for each numerical evaluation and analysing Fig. 3.2b, CPS8R is the most time-consuming element and CPS4R the least.

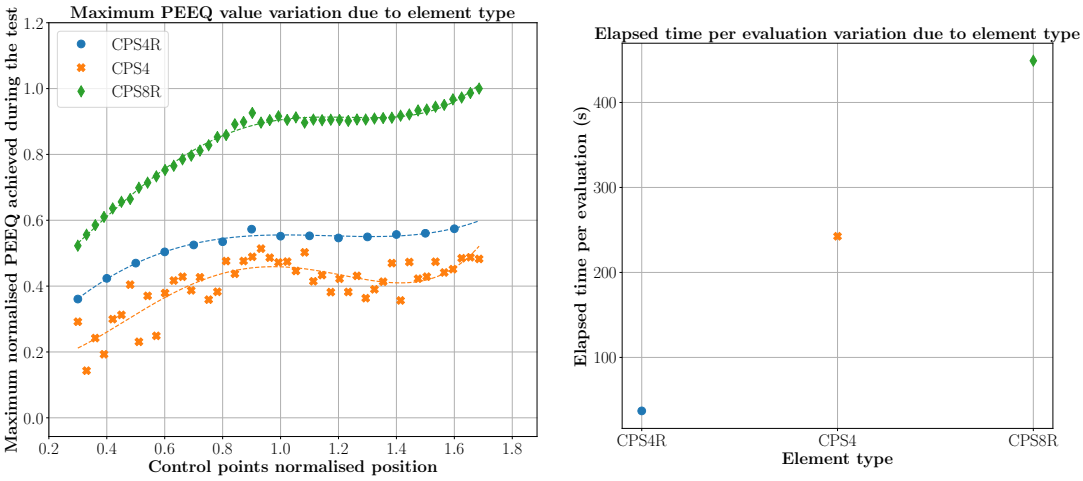

(a) (b)

Figure 3.2: (a) Maximum normalised equivalent plastic strain achieved during the test with the different control points' position and (b) its required computational time due to element type variation.

It is assumed that the solutions analysed using this process have element type dependency and future errors might be caused by it. CPS4R was chosen for the following work as element type since it provides a good time-accuracy compromise.

3.3 Reference solution

Having the finite element mesh size and element type defined for the FEA, a solution was used as a reference for further comparisons. It is the best solution obtained out of the optimisation procedure, with an initial circular interior notch specimen shape, with a 10 mm radius. The used finite element mesh is non-parametric and made with CPS4R elements with 0.3 mm along the edges. The cost function used to evaluate the solutions is I_{T1}. It was considered five curve control points, and a fixed point is introduced in the vertical symmetry. The specimen's height/width ratio used in the design by optimisation method is 5.3, obtained by an overall specimen's height of 265.0 mm and width of 50.0 mm. The optimisation algorithm used is the Nelder-Mead, a direct search type. The mentioned parameters are analysed in the following, by varying each one and comparing it to the reference solution results. This way, the best parameters can be chosen and used together to obtain the most heterogeneous specimen shape.

3.4 Objective function dependency analysis

One of the most challenging goals of this work is the use of a heterogeneous indicator as a cost function for the solution's evaluation. Keeping in mind that the goal is to find the specimen's geometry that provides the most amount of mechanical information, such as many strain and stress states, as well as a significant strain levels, the optimisation analysis was performed with the different indicators.

Fig. 3.3 shows each cost function evolution along with the iterations and evaluations, as well as the obtained final solutions' and the respective first and second spline's derivative. Every optimisation process terminated successfully, reaching an inferior value compared to the first evaluation, as can be seen in Fig. 3.3a, 3.3c and 3.3e. The convergence to a minimum is noticed, although it cannot be proved that it is the global minimum. Since the number of evaluations required for I_{T3} analysis is lower than the others, it might be due to premature convergence and local minimum finding.

All the achieved solutions show different interior notch shapes, although some particularities in the solutions generated with I_{T2} and I_{T3} are visible in the solution obtained with I_{T1}. The spline's C^1 continuity is checked for every achieved solution since the x first derivative is zero in one end and the y first derivative is zero in the other end, ensuring symmetry conditions of the specimens. In contrast, the second derivative is different from zero in the symmetries, thus the C^2 spline's continuity is not verified.

To compare the variation of the cost function value between the initial solution and the best solution, it was calculated the normalised cost function variation mathematically given as:

$$CF_{\mathrm{norm,var}} = \left\| \frac{CF_{\mathrm{best}} - CF_{\mathrm{first}}}{CF_{\mathrm{first}}} \right\|. \tag{3.1}$$

These values are presented in Fig. 3.4, as well as the number of evaluations normalised by the reference.

The highest cost function variation is reached with the indicator I_{T3} and the lowest was obtained with the indicator I_{T1}. A lower normalised cost function variation value can indicate that the solution has converged to a local minimum, but not guaranteed.

The minor and major stress (SMinSMaxRatio) and strain ratios (LEMinLEMaxRatio), von Mises stress (S, Mises) and equivalent plastic strain (PEEQ) of the moment just before rupture can be analysed in Fig. 3.5. The range of strain and stress states is limited to the considered states in this work. That is why some elements are coloured black and grey. Comparing the values of the Tab. 2.1 with the solutions' strain and stress ratios, it can be concluded that the majority of the specimens' surface is within tension state, showing uniaxial compression and pure shear states in the top and bottom surroundings of the interior notch. The optimum solutions obtained with the indicators I_{T1} and I_{T3} have similar von Mises stress distributions. The larger PEEQ value is obtained with the indicator I_{T1} and the lowest with I_{T2}, although all indicators result in similar maximum PEEQ values, as expected due to the rupture criterion. Concerning the PEEQ distribution along the specimen, it can be noticed that the top part of the specimen has no plastic strain, meaning that the grips will not interfere in the experimental data acquisition. Besides, the opposite occurs along the specimen width, meaning that this dimension should be further analysed.

The strain and stress diagrams (Fig. 3.6) offer a better understanding of the strain

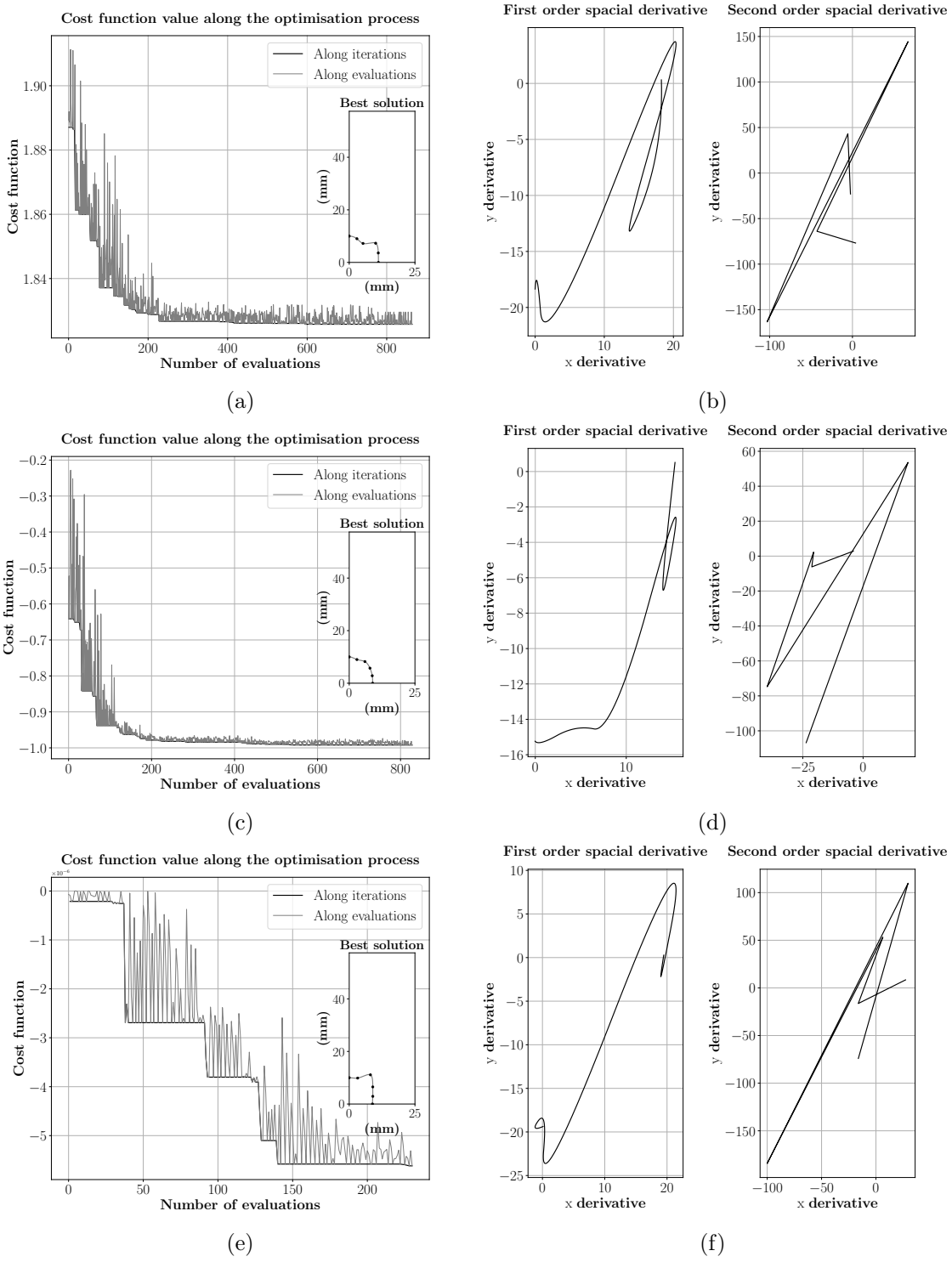

Figure 3.3: Cost function evaluation and best-obtained solution, using (a) I_{T1}, (c) I_{T2} and (e) I_{T3}. Best solution's first and second derivative, using (b) I_{T1}, (d) I_{T2} and (f) I_{T3}.

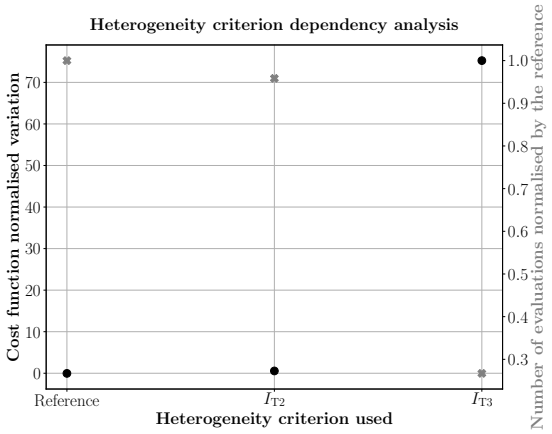

Figure 3.4: Analysis of the optimisation cost function and number of evaluations, depending on the heterogeneity criterion used.

and stress states and its intensity, resulting in a good method for the specimens' heterogeneity comparison. Looking at the principal strain diagrams, the sample generated with the indicator I_{T3} seems to show a larger number of elements with higher plastic strain values, than the other specimens. This is a characteristic that should be valued in a heterogeneous mechanical test. Whereas the solution created with the indicator I_{T1} presents an interesting stress state sweep starting in the uniaxial tension state, ending in the compression state, going through the pure shear state and every in-between stress states. While the solution obtained with I_{T2} seems to show a larger number of elements in the uniaxial compression.

In Fig. 3.7 it can be seen the average PEEQ of each considered strain state at the moment just before rupture occurs of the best geometries obtained with each criteria. None of the specimens produces the biaxial neither the plane strain states. The best geometry generated with I_{T1} shows uniaxial tension, pure shear and uniaxial compression strain states, whereas the specimen obtained with I_{T2} favours the uniaxial compression strain state and the solution created with I_{T3} favours the pure shear strain state. The average PEEQ is larger in the solution obtained with the indicator I_{T3}.

Tab. 3.1 shows, for the three specimens obtained with the different indicators, its cost function value considering the other heterogeneity indicators. For all cases, the best cost function value is obtained with the respectively best-obtained solutions, except for the solution obtained with I_{T3} that has a better performance with the indicator I_{T1} than the solution originated by the I_{T1}. This indicates that the solution obtained with I_{T1} is a local minimum, and the solution of I_{T3} outperforms the solution of I_{T1}

Table 3.1: Analysis of the best solutions using the three different heterogeneity indicators.

	CF value with I_{T1}	**CF value with I_{T2}**	**CF value with I_{T3}**
I_{T1}	1.826	-0.639	-1.81E-06
I_{T2}	1.867	-0.992	-2.18E-06
I_{T3}	1.820	-0.664	-5.62E-06

In conclusion, the different heterogeneity criteria show different benefits and none of

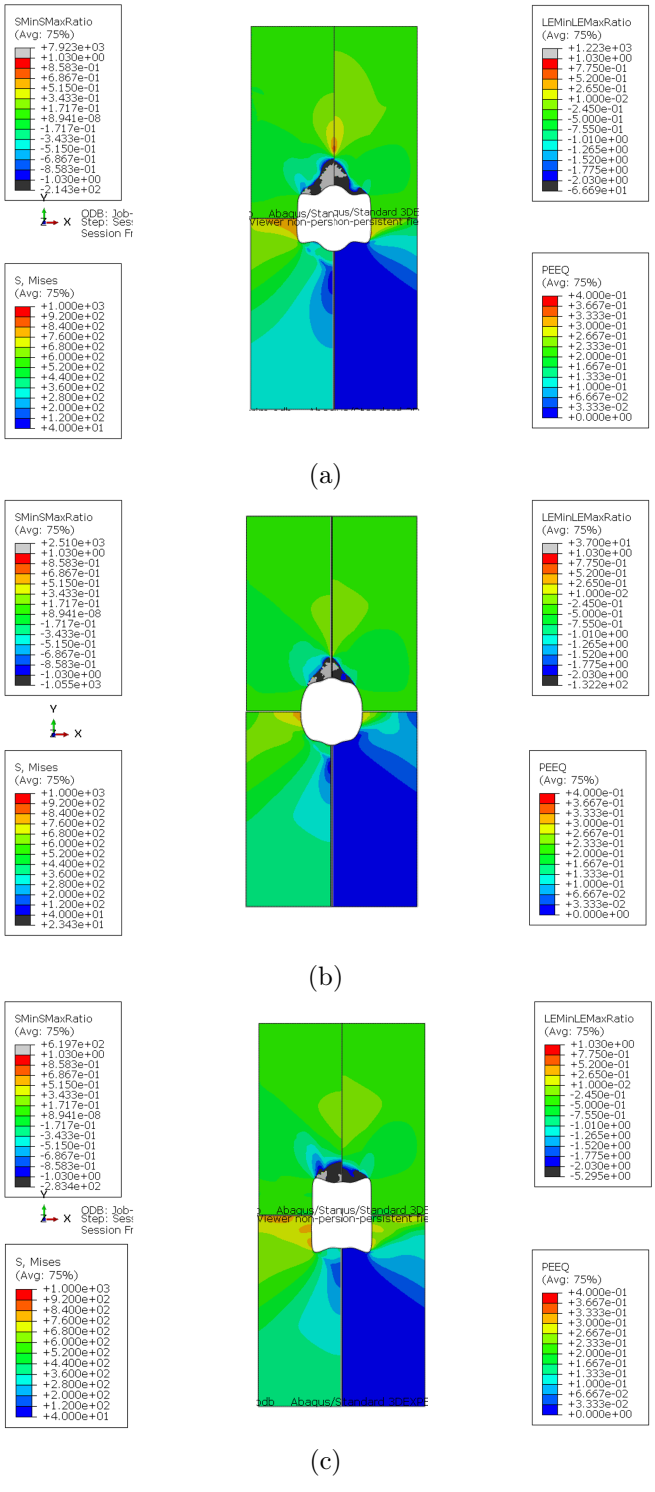

Figure 3.5: Best obtained solutions' minor and major stress (SMinSMaxRatio) and strain ratios (LEMinLEMaxRatio), von Mises stress (S, Mises) and equivalent plastic strain (PEEQ) at the moment just before rupture using (a) I_{T1}, (b) I_{T2} and (c) I_{T3}.

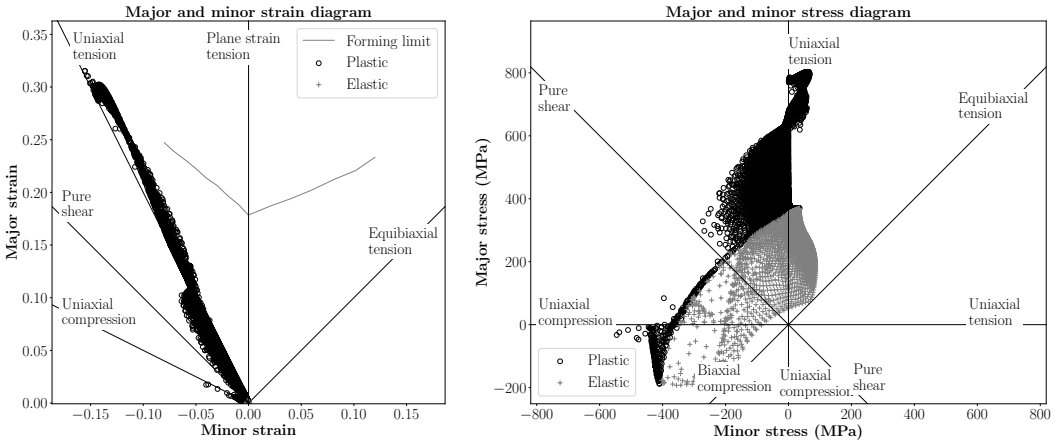

(a)

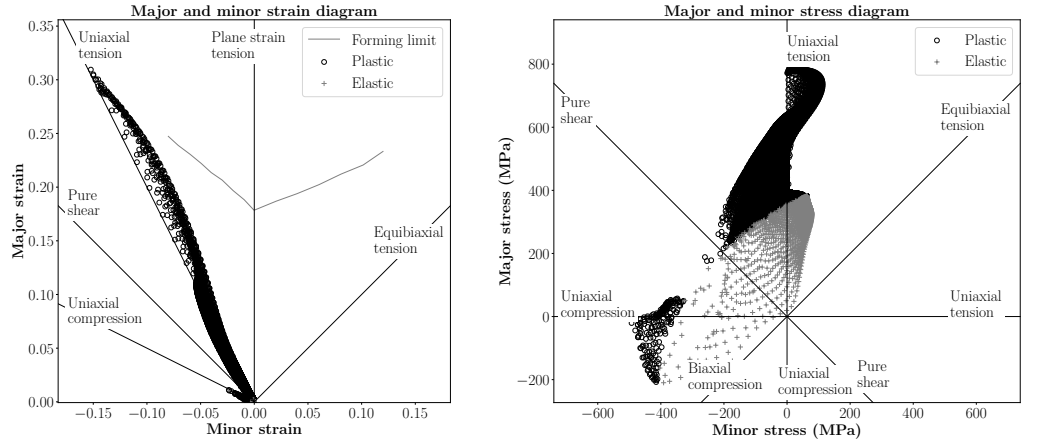

(b)

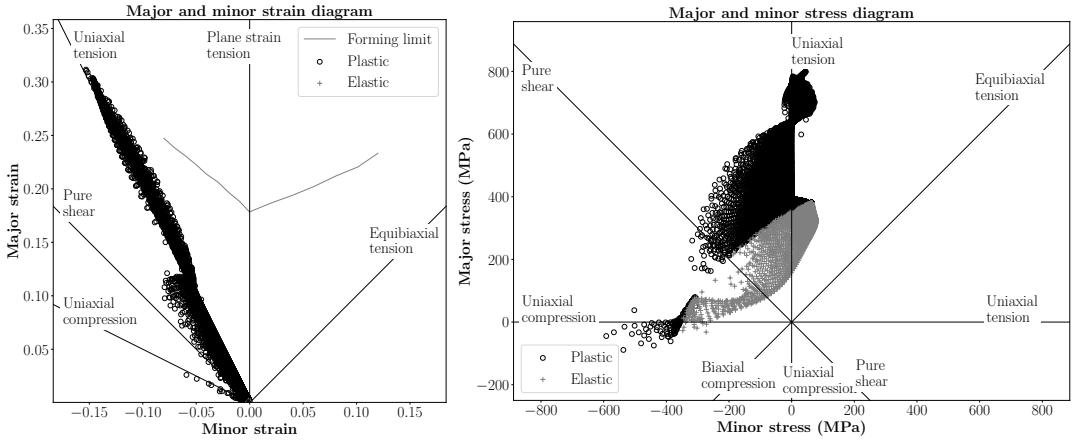

(c)

Figure 3.6: Minor and major strain and stress diagrams at the moment just before rupture using (a) I_{T1}, (b) I_{T2} and (c) I_{T3}.

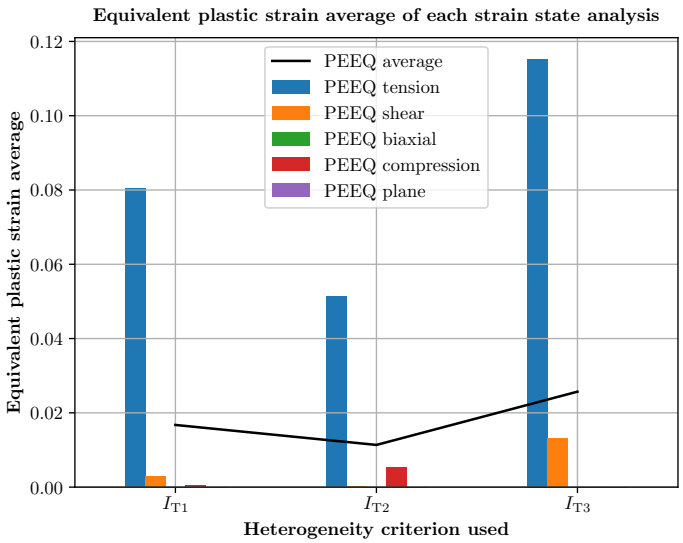

Figure 3.7: Average equivalent plastic strain for each strain state depending on the heterogeneity criterion used.

them is clearly better than the others. Since that a choice has to be made for the further analysis, it was chosen the I_{T1} indicator, because of its promising principal stress diagram with a range of elements with stress states from the uniaxial tension until the uniaxial compression. Besides, this indicator is obtained from the literature and has already been well studied and applied for many different specimens.

3.5 Boundary conditions dependency analysis

The specimen's boundary conditions in the vertical and horizontal axis are symmetries and one of them has a fixed curve point. The fixed point introduced in the spline in the vertical symmetry must be analysed in order to understand its influence in the final result. So, it was changed its position in the curve. It was performed an optimisation procedure with the same number of curve control points, but the fixed point was introduced in the horizontal symmetry, while the vertical symmetry had a free radius position for its point.

The cost function evolution, as well as the final solution and its first and second spline's derivative are presented in Fig. 3.8. The solution referring to Fig. 3.8a is the reference and has its fixed point in the vertical symmetry, while Fig 3.8c belongs to the solution with the fixed point in the horizontal symmetry. Both optimisation procedures terminated successfully with a cost function value of 1.826 for the reference solution and of 1.843 for the solution with the fixed point in the horizontal symmetry. The reference solution achieved a better cost function final value. The obtained shapes are different, but both have C^1 continuity in the symmetries.

Comparing the cost function best value (Fig. 3.9), the solution with the fixed point in the horizontal symmetry is approximately 1.01 times the reference's cost function value and the number of required evaluations is smaller than for the reference.

Analysing the solutions' minor and major stress (SMinSMaxRatio) and strain ratios

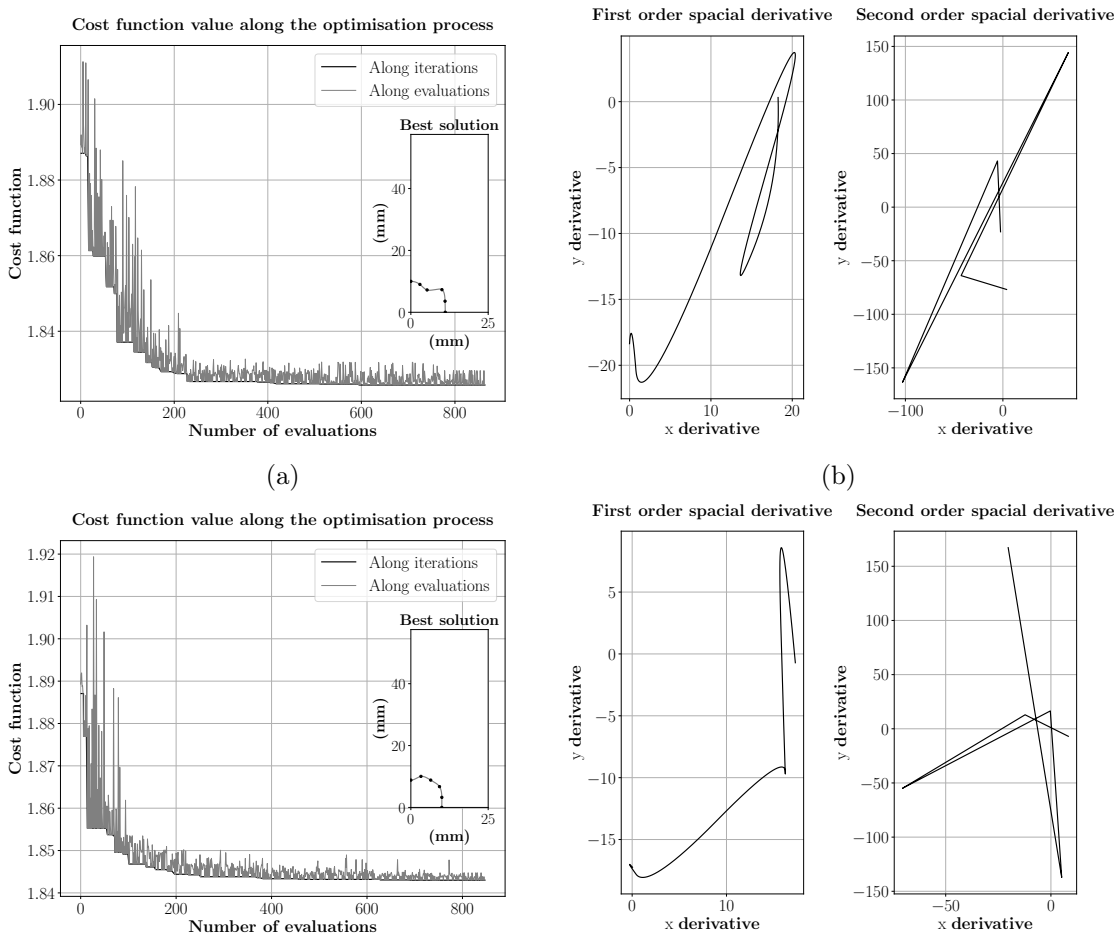

Figure 3.8: Cost function evaluation and best-obtained solution, when the fixed point is in (a) the vertical symmetry and (c) in the horizontal symmetry. Best solution's first and second derivative, when the fixed point is in (b) the vertical symmetry and (d) in the horizontal symmetry.

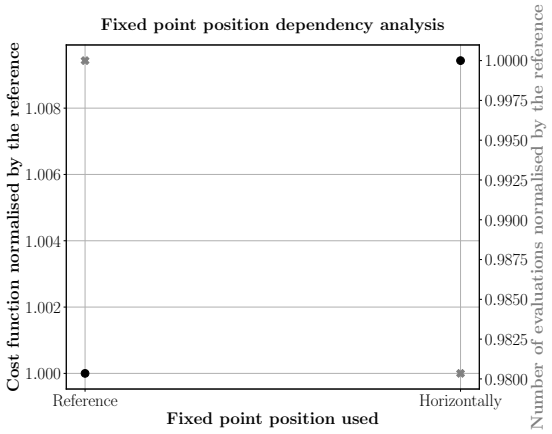

Figure 3.9: Analysis of the optimisation cost function and number of evaluations, depending on the boundary conditions applied.

(LEMinLEMaxRatio), von Mises stress (S, Mises) and equivalent plastic strain (PEEQ) at the moment just before rupture, depicted in Fig. 3.10, all the variables reveal similar distributions. The specimen's top part is not under plastic deformation, so there will not be a problem concerning the grips interfering in the experimental data extraction.

Having in consideration the best-obtained solution's principal strain and stress diagrams shown in Fig. 3.11, both are quite similar in terms of strain and stress elements' distribution along the deformation states. Although, it seems that the reference solution presents more elements in the pure shear state.

For a better strain states and comparison, Fig. 3.12 is presented. It shows the best solution's average value of the obtained equivalent plastic strain for each strain state. Both solutions achieved the same strain states, but the reference solution reached larger average strain values for all the states. A larger difference is noticed in the uniaxial compression strain state.

The best-obtained solution with the fixed point in the horizontal symmetry achieved lower strain levels, resulting in a worse cost function evaluation, comparing to the reference solution.

3.6 Analysis of the number of curve control points

It was performed an analysis varying only the number of the spline's control points. It was studied the solutions with 4, 5, 6, 8, 10, 12, and 14 control points. The cost function value along the evaluations, as well as the best solutions and its derivatives, are presented in Fig. 3.13. All processes have successfully converged to a better solution. The solution analysed with 14 control points has stopped due to the reaching of the maximum number of iterations of 500, resulting in more than 2000 evaluations. However, looking at the figure, the process shows convergence. When using a larger number of control points, the number of evaluations is higher, apart from the solution obtained with 8 control points. This might be due to a local minimum finding. It is noticeable small variances when adding another control point to the previous spline's solution. It is verified C^1 splines' continuity in every solution, for both symmetries.

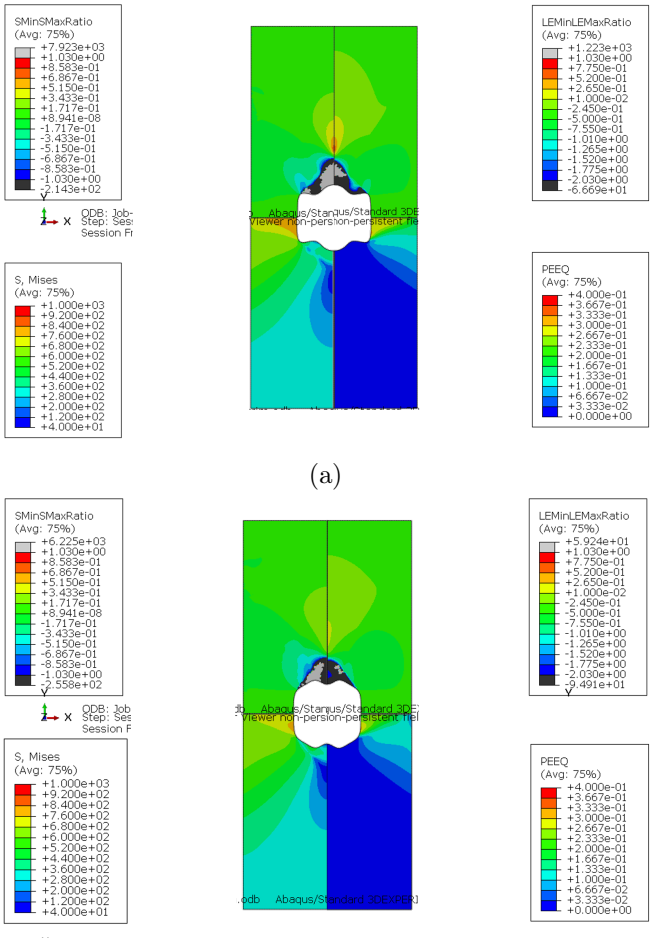

Figure 3.10: Best obtained solutions' minor and major stress (SMinSMaxRatio) and strain ratios (LEMinLEMaxRatio), von Mises stress (S, Mises) and equivalent plastic strain (PEEQ) at the moment just before rupture, when the fixed point is in (a) the vertical symmetry and (b) in the horizontal symmetry.

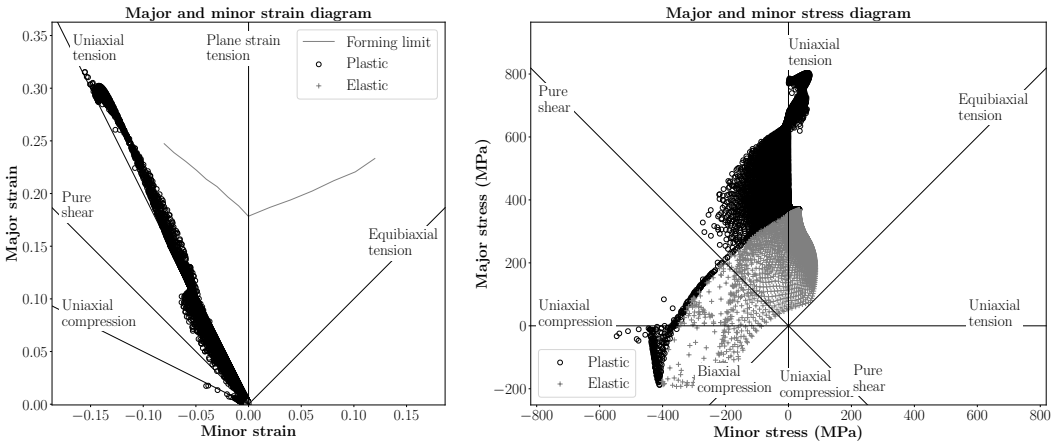

(a)

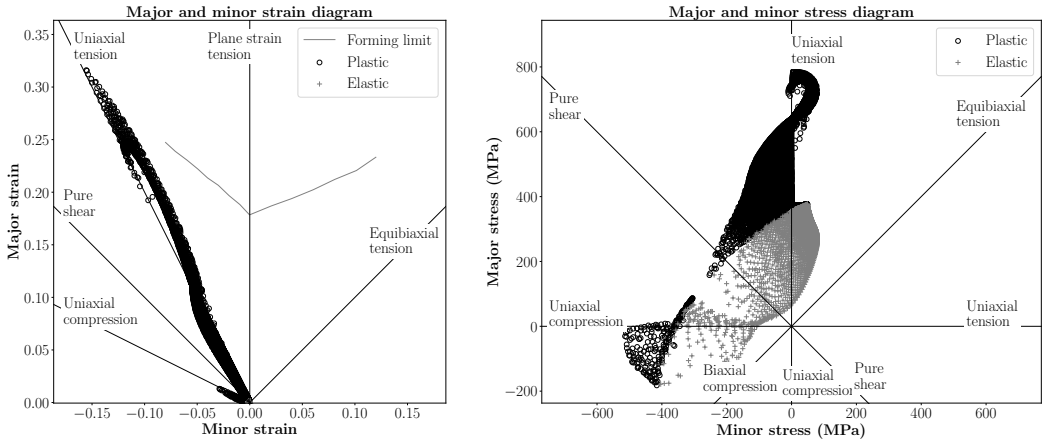

(b)

Figure 3.11: Minor and major strain and stress diagrams at the moment just before rupture, when the fixed point is in (a) the vertical symmetry and (b) in the horizontal symmetry.

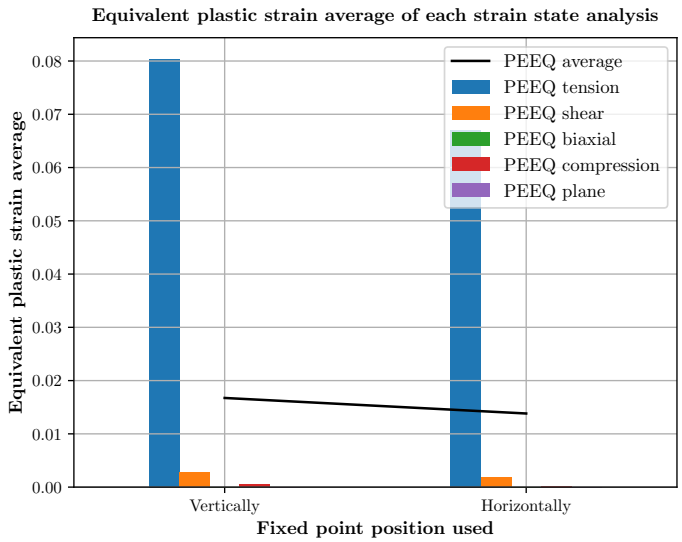

Figure 3.12: Average equivalent plastic strain for each strain state, depending on the boundary condition applied.

Concerning the cost function value and number of evaluations comparison, Fig. 3.14 is presented. Overall, for a larger number of control points, the cost function value is higher, whereas, for a smaller number of control points, the cost function value is lower. Every number of control points analysed generated worse solutions, in terms of cost function value, compared to the reference solution, apart from the solution with 6 control points. The solution with the best cost function value was the one obtained with 6 control points.

It can be noticed that the strain and stress distributions presented in Fig. 3.15 are relatively similar to each other, whatever the number of control points is used. All the solutions show a large predominance of the uniaxial tensile strain state, as expected. However, in the area near the interior notch it is noticeable uniaxial compression and pure shear strain states. None of the solutions exhibit possible problems regarding the experimental test and its data acquisition.

Analogous conclusions can be made when observing the principal strain and stress diagrams in Fig. 3.16. The number of control points little influences the strain and stress states.

Concerning only the equivalent plastic strain average of each strain state, shown in Fig. 3.17, it is verified that the solution obtained with 6 control points presents a larger PEEQ average mainly due to the tension strain state, whereas the solution with 12 control points generates larger PEEQ subjected to shear and compression strain states. Nevertheless, it shows a smaller PEEQ averaged for the tension strain state. The solution with 14 control points is the one with a larger PEEQ average subjected to the compression strain state.

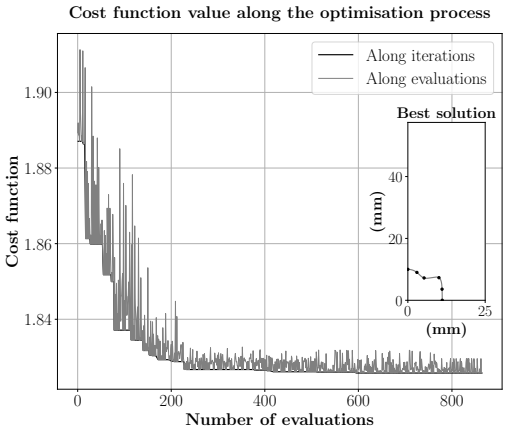
Cost function value along the optimisation process
Along iterations
Along evaluations
Best solution
(mm)
Cost function
Number of evaluations

(a)

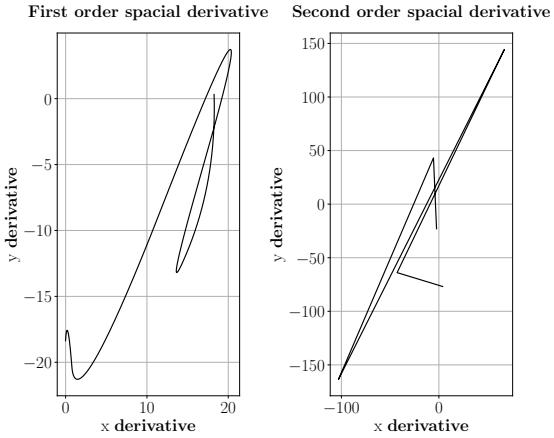
First order spacial derivative
Second order spacial derivative
y derivative
x derivative

(b)

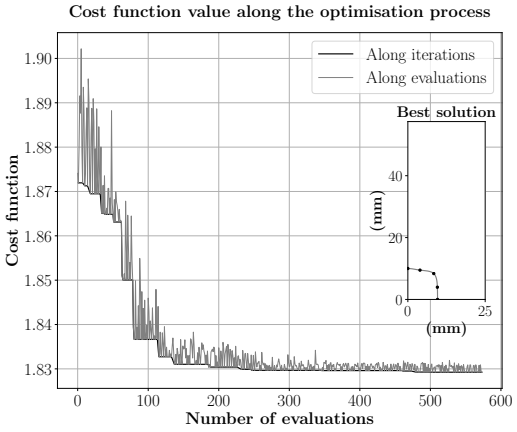
Cost function value along the optimisation process
Along iterations
Along evaluations
Best solution
(mm)
Cost function
Number of evaluations

(c)

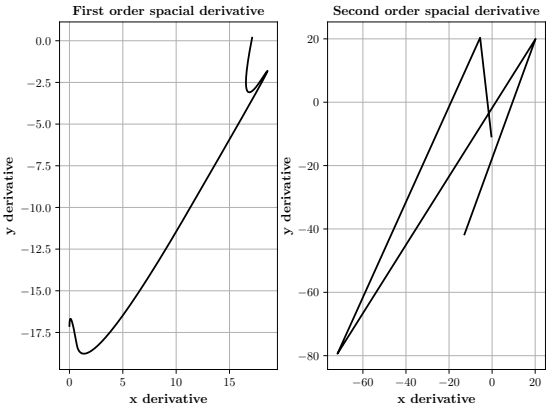
First order spacial derivative
Second order spacial derivative
y derivative
x derivative

(d)

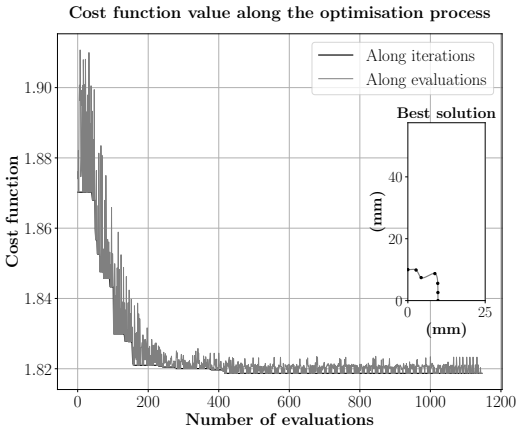
Cost function value along the optimisation process
Along iterations
Along evaluations
Best solution
(mm)
Cost function
Number of evaluations

(e)

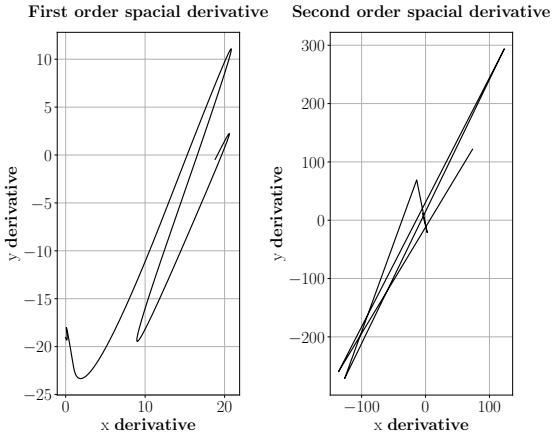
First order spacial derivative
Second order spacial derivative
y derivative
x derivative

(f)

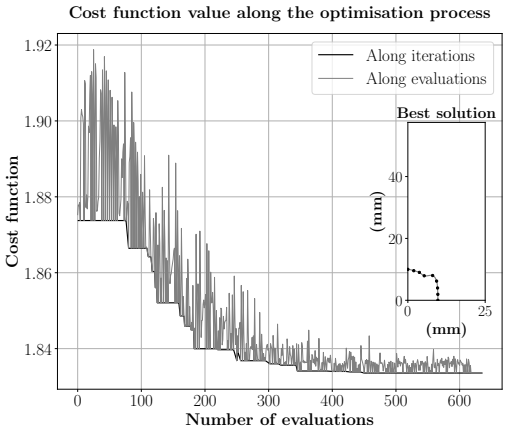
Cost function value along the optimisation process
Along iterations
Along evaluations
Best solution
(mm)
(mm)
Cost function
Number of evaluations

(g)

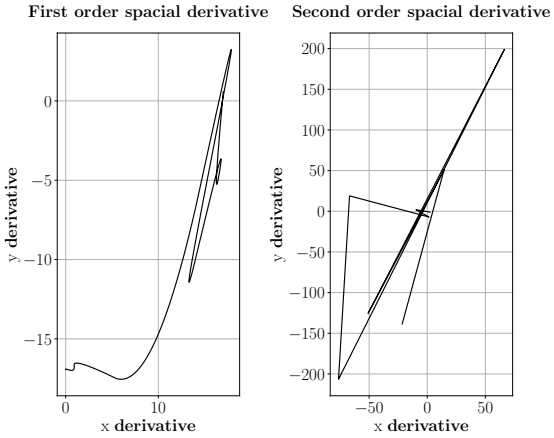
First order spacial derivative
Second order spacial derivative
y derivative
x derivative
y derivative
x derivative

(h)

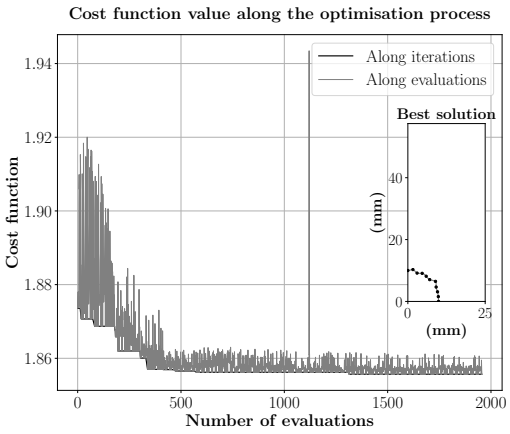
Cost function value along the optimisation process
Along iterations
Along evaluations
Best solution
(mm)
(mm)
Cost function
Number of evaluations

(i)

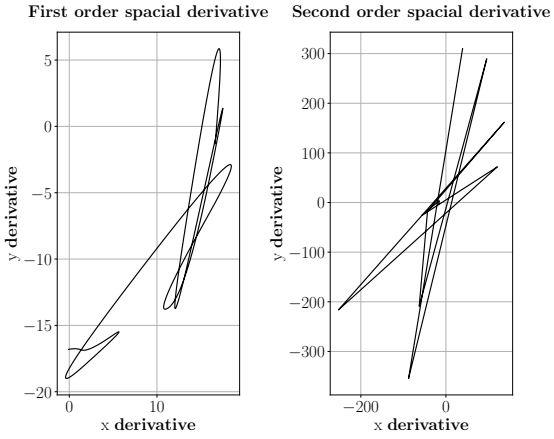
First order spacial derivative
Second order spacial derivative
y derivative
x derivative
y derivative
x derivative

(j)

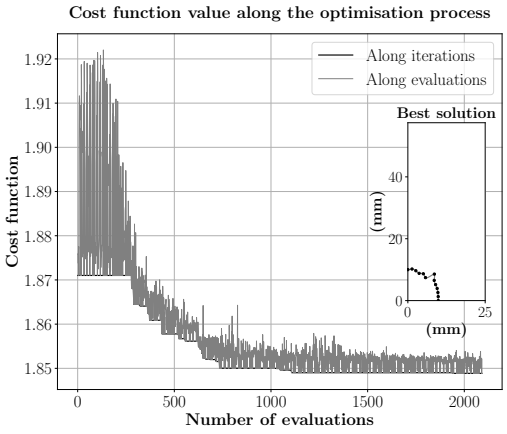
Cost function value along the optimisation process
Along iterations
Along evaluations
Best solution
(mm)
(mm)
Cost function
Number of evaluations

(k)

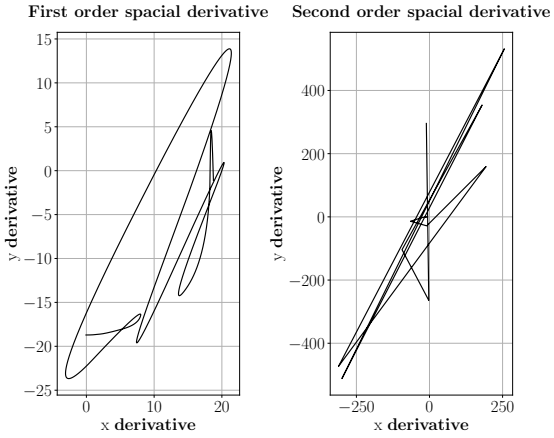
First order spacial derivative
Second order spacial derivative
y derivative
x derivative
y derivative
x derivative

(l)

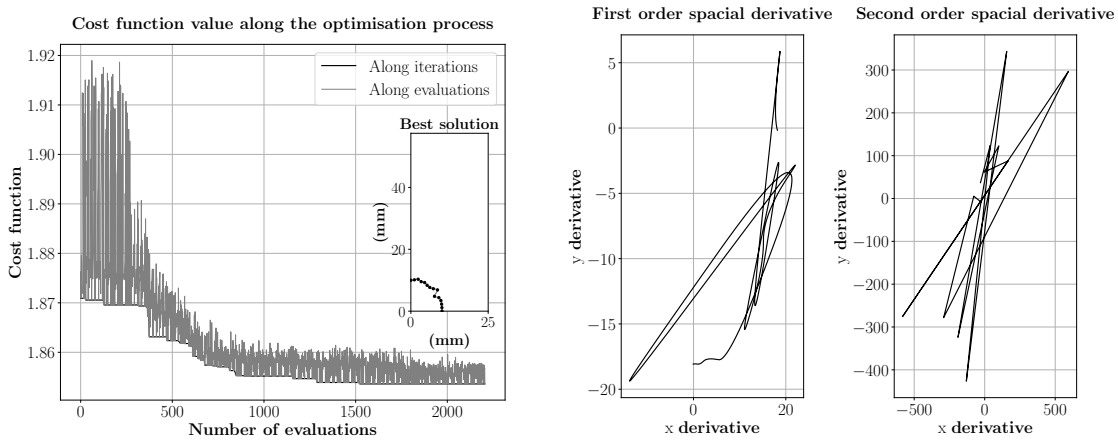

(m) (n)

Figure 3.13: Cost function evaluation and best-obtained solution, using (a) 5 control points, (c) 4 control points, (e) 6 control points, (g) 8 control points, (i) 10 control points, (k) 12 control points and (m) 14 control points. Best solution's first and second derivative, using (b) 5 control points, (d) 4 control points, (f) 6 control points, (h) 8 control points, (j) 10 control points, (l) 12 control points and (n) 14 control points.

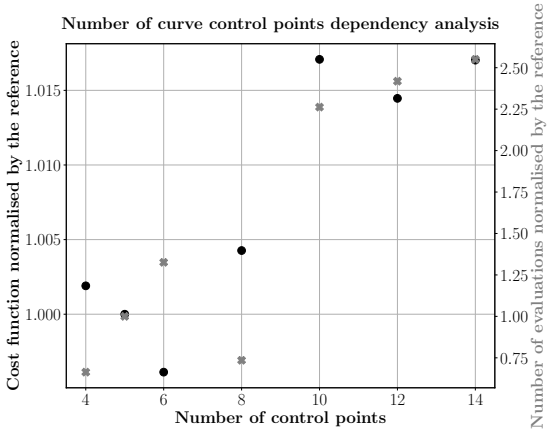

Figure 3.14: Analysis of the optimisation cost function and number of evaluations, depending on the number of the curve control points used.

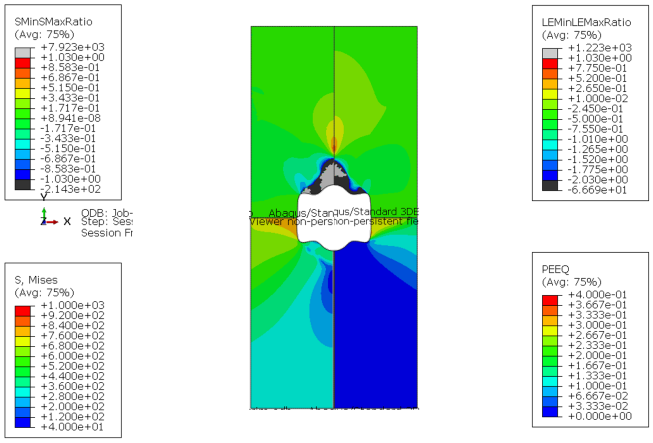
SMinSMaxRatio
(Avg: 75%)
+7.923e+03
+1.030e+00
+8.583e-01
+6.867e-01
+5.150e-01
+3.433e-01
+1.717e-01
+8.941e-08
-1.717e-01
-3.433e-01
-5.150e-01
-6.867e-01
-8.583e-01
-1.030e+00
-2.143e+02
LEMinLEMaxRatio
(Avg: 75%)
+1.223e+03
+1.030e+00
+7.750e-01
+5.200e-01
+2.650e-01
+1.000e-02
-2.450e-01
-5.000e-01
-7.550e-01
-1.010e+00
-1.265e+00
-1.520e+00
-1.775e+00
-2.030e+00
-6.669e+01
S, Mises
(Avg: 75%)
+1.000e+03
+9.200e+02
+8.400e+02
+7.600e+02
+6.800e+02
+6.000e+02
+5.200e+02
+4.400e+02
+3.600e+02
+2.800e+02
+2.000e+02
+1.200e+02
+4.000e+01
PEEQ
(Avg: 75%)
+4.000e-01
+3.667e-01
+3.333e-01
+3.000e-01
+2.667e-01
+2.333e-01
+2.000e-01
+1.667e-01
+1.333e-01
+1.000e-01
+6.667e-02
+3.333e-02
+0.000e+00

(a)

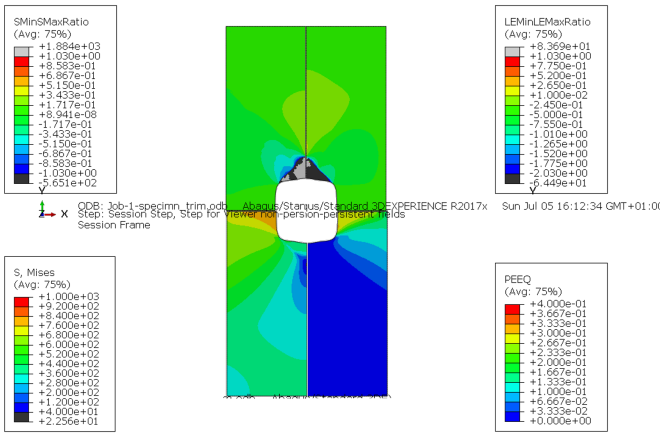
SMinSMaxRatio
(Avg: 75%)
+1.884e+03
+1.030e+00
+8.583e-01
+6.867e-01
+5.150e-01
+3.433e-01
+1.717e-01
+8.941e-08
-1.717e-01
-3.433e-01
-5.150e-01
-6.867e-01
-8.583e-01
-1.030e+00
-6.651e+02
LEMinLEMaxRatio
(Avg: 75%)
+8.369e+01
+1.030e+00
+7.750e-01
+5.200e-01
+2.650e-01
+1.000e-02
-2.450e-01
-5.000e-01
-7.550e-01
-1.010e+00
-1.265e+00
-1.520e+00
-1.775e+00
-2.030e+00
-6.449e+01
ODB: Job-1-specimn_trim.odb Abaqus/Standard 3DEXPERIENCE R2017x Sun Jul 05 16:12:34 GMT+01:0
Step: Session Step, Step for Viewer non-persion-persistent fields
Session Frame
S, Mises
(Avg: 75%)
+1.000e+03
+9.200e+02
+8.400e+02
+7.600e+02
+6.800e+02
+6.000e+02
+5.200e+02
+4.400e+02
+3.600e+02
+2.800e+02
+2.000e+02
+1.200e+02
+4.000e+01
+2.256e+01
PEEQ
(Avg: 75%)
+4.000e-01
+3.667e-01
+3.333e-01
+3.000e-01
+2.667e-01
+2.333e-01
+2.000e-01
+1.667e-01
+1.333e-01
+1.000e-01
+6.667e-02
+3.333e-02
+0.000e+00

(b)

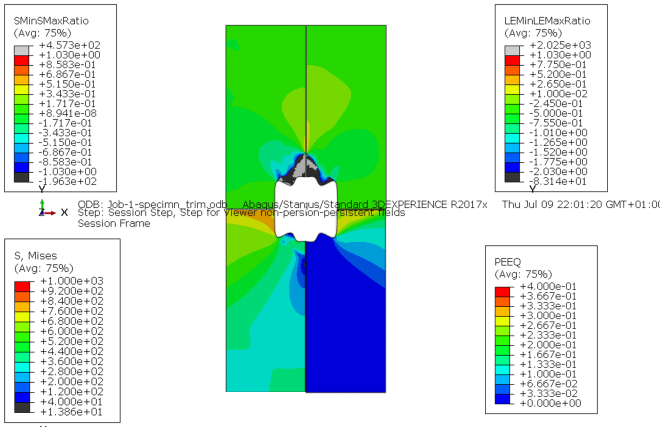
SMinSMaxRatio
(Avg: 75%)
+4.573e+02
+1.030e+00
+8.583e-01
+6.867e-01
+5.150e-01
+3.433e-01
+1.717e-01
+8.941e-08
-1.717e-01
-3.433e-01
-5.150e-01
-6.867e-01
-8.583e-01
-1.030e+00
-1.963e+02
LEMinLEMaxRatio
(Avg: 75%)
+2.025e+03
+1.030e+00
+7.750e-01
+5.200e-01
+2.650e-01
+1.000e-02
-2.450e-01
-5.000e-01
-7.550e-01
-1.010e+00
-1.265e+00
-1.520e+00
-1.775e+00
-2.030e+00
-8.314e+01
ODB: Job-1-specimn_trim.odb Abaqus/Standard 3DEXPERIENCE R2017x Thu Jul 09 22:01:20 GMT+01:0
Step: Session Step, Step for Viewer non-persion-persistent fields
Session Frame
S, Mises
(Avg: 75%)
+1.000e+03
+9.200e+02
+8.400e+02
+7.600e+02
+6.800e+02
+6.000e+02
+5.200e+02
+4.400e+02
+3.600e+02
+2.800e+02
+2.000e+02
+1.200e+02
+4.000e+01
+1.386e+01
PEEQ
(Avg: 75%)
+4.000e-01
+3.667e-01
+3.333e-01
+3.000e-01
+2.667e-01
+2.333e-01
+2.000e-01
+1.667e-01
+1.333e-01
+1.000e-01
+6.667e-02
+3.333e-02
+0.000e+00

(c)

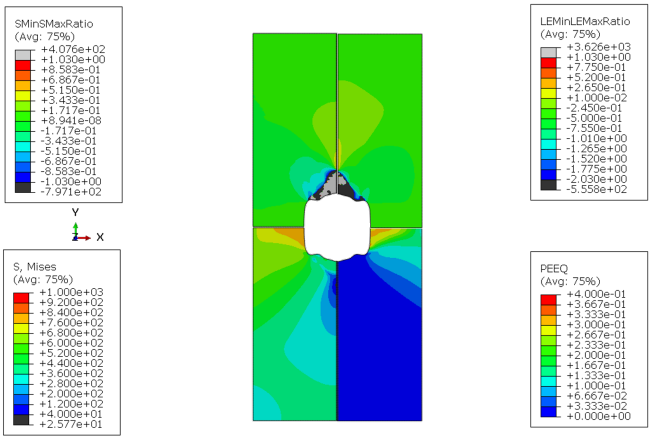
SMinSMaxRatio
(Avg: 75%)
+4.076e+02
+1.030e+00
+8.583e-01
+6.867e-01
+5.150e-01
+3.433e-01
+1.717e-01
+8.941e-08
-1.717e-01
-3.433e-01
-5.150e-01
-6.867e-01
-8.583e-01
-1.030e+00
-7.971e+02
S, Mises
(Avg: 75%)
+1.000e+03
+9.200e+02
+8.400e+02
+7.600e+02
+6.800e+02
+6.000e+02
+5.200e+02
+4.400e+02
+3.600e+02
+2.800e+02
+2.000e+02
+1.200e+02
+4.000e+01
+2.577e+01
LEMinLEMaxRatio
(Avg: 75%)
+3.626e+03
+1.030e+00
+7.750e-01
+5.200e-01
+2.650e-01
+1.000e-02
-2.450e-01
-5.000e-01
-7.550e-01
-1.010e+00
-1.265e+00
-1.520e+00
-1.775e+00
-2.030e+00
-5.558e+02
PEEQ
(Avg: 75%)
+4.000e-01
+3.667e-01
+3.333e-01
+3.000e-01
+2.667e-01
+2.333e-01
+2.000e-01
+1.667e-01
+1.333e-01
+1.000e-01
+6.667e-02
+3.333e-02
+0.000e+00

(d)

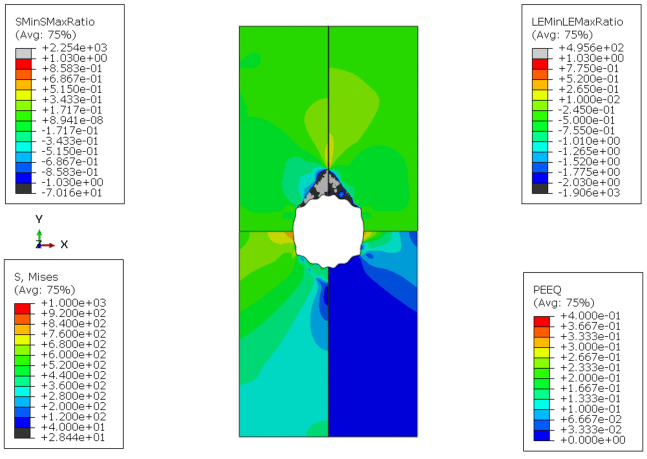
SMinSMaxRatio
(Avg: 75%)
+2.254e+03
+1.030e+00
+8.583e-01
+6.867e-01
+5.150e-01
+3.433e-01
+1.717e-01
+8.941e-08
-1.717e-01
-3.433e-01
-5.150e-01
-6.867e-01
-8.583e-01
-1.030e+00
-7.016e+01
S, Mises
(Avg: 75%)
+1.000e+03
+9.200e+02
+8.400e+02
+7.600e+02
+6.800e+02
+6.000e+02
+5.200e+02
+4.400e+02
+3.600e+02
+2.800e+02
+2.000e+02
+1.200e+02
+4.000e+01
+2.844e+01
LEMinLEMaxRatio
(Avg: 75%)
+4.956e+02
+1.030e+00
+7.750e-01
+5.200e-01
+2.650e-01
+1.000e-02
-2.450e-01
-5.000e-01
-7.550e-01
-1.010e+00
-1.265e+00
-1.520e+00
-1.775e+00
-2.030e+00
-1.906e+03
PEEQ
(Avg: 75%)
+4.000e-01
+3.667e-01
+3.333e-01
+3.000e-01
+2.667e-01
+2.333e-01
+2.000e-01
+1.667e-01
+1.333e-01
+1.000e-01
+6.667e-02
+3.333e-02
+0.000e+00

(e)

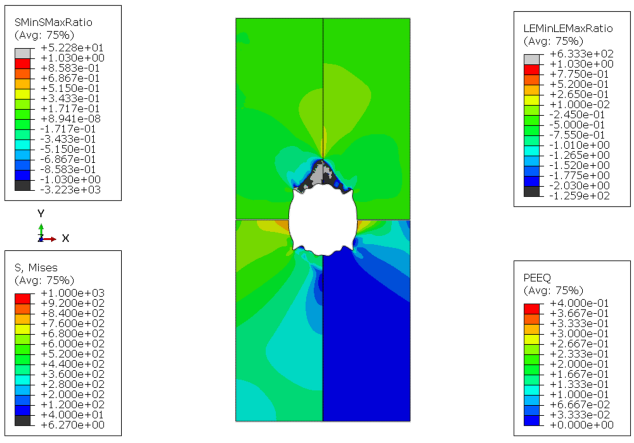
SMinSMaxRatio
(Avg: 75%)
+5.228e+01
+1.030e+00
+8.583e-01
+6.867e-01
+5.150e-01
+3.433e-01
+1.717e-01
+8.941e-08
-1.717e-01
-3.433e-01
-5.150e-01
-6.867e-01
-8.583e-01
-1.030e+00
-3.223e+03
S, Mises
(Avg: 75%)
+1.000e+03
+9.200e+02
+8.400e+02
+7.600e+02
+6.800e+02
+6.000e+02
+5.200e+02
+4.400e+02
+3.600e+02
+2.800e+02
+2.000e+02
+1.200e+02
+4.000e+01
+6.270e+00
LEMinLEMaxRatio
(Avg: 75%)
+6.333e+02
+1.030e+00
+7.750e-01
+5.200e-01
+2.650e-01
+1.000e-02
-2.450e-01
-5.000e-01
-7.550e-01
-1.010e+00
-1.265e+00
-1.520e+00
-1.775e+00
-2.030e+00
-1.259e+02
PEEQ
(Avg: 75%)
+4.000e-01
+3.667e-01
+3.333e-01
+3.000e-01
+2.667e-01
+2.333e-01
+2.000e-01
+1.667e-01
+1.333e-01
+1.000e-01
+6.667e-02
+3.333e-02
+0.000e+00

(f)

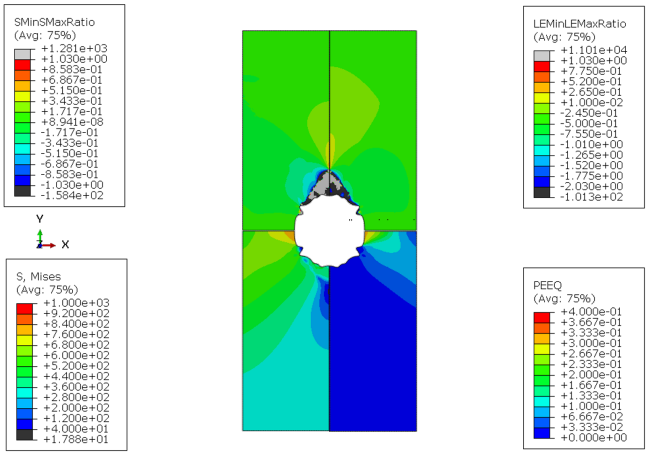

(g)

Figure 3.15: Best obtained solutions' minor and major stress (SMinSMaxRatio) and strain ratios (LEMinLEMaxRatio), von Mises stress (S, Mises) and equivalent plastic strain (PEEQ) at the moment just before rupture, using (a) 5 control points, (b) 4 control points, (c) 6 control points, (d) 8 control points, (e) 10 control points, (f) 12 control points and (g) 14 control points.

3.7 Specimen height/width ratio dependency analysis

Since the specimen's width and height were not considered as optimisation variables and considering that they can influence the results, it was performed a height/width ratio dependency analysis. The widths of 50 mm, 60 mm, 65 mm, 80 mm, 100 mm and 120 mm were tested, keeping the specimens' height, corresponding to height/width ratios of 5.30, 4.42, 4.08, 3.31, 2.65 and 2.21, respectively. The evaluations' cost function value, the obtained solutions, and its splines' first and second derivatives are depicted in Fig. 3.18.

Every analysed solution seems to have successfully converged to a better solution within approximately 800 evaluations. All the obtained solutions are different from each other and show spline C^1 continuity.

Seeing Fig. 3.19, it is noticed that the cost function value improves (reduce) with larger height/width ratios than the reference, until ratios larger than 4 where it starts to get worse (higher), with the exception of the solution obtained with the height/width ratio of 2.65. The best solution value is obtained with this ratio.

In Fig. 3.20, the best-obtained solutions' minor and major stress and strain ratios, von Mises stress and equivalent plastic strain are illustrated at the moment just before rupture, along the specimens' surface. Here it is observed that, for some solutions, the spline's continuity is lost when transferred to Abaqus [Dassault Systèmes 2014]. Several differences in the strain and stress distributions are noticed. However, all the solutions exhibit uniaxial tension, uniaxial compression and pure shear strain states. Concerning the grips interference in the experimental test, the solutions with a smaller height/width ratio show some problems, since the plastic deformation is verified in the specimen's bottom and top parts.

The minor and major strain and stress diagrams at the moment just before rupture, with the different height/width ratios, are presented in Fig. 3.21. On the overall, the

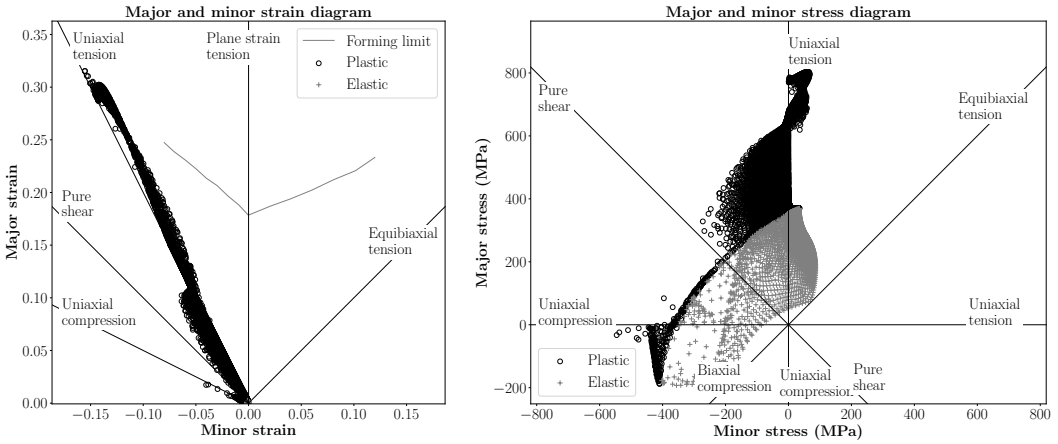
Major and minor strain diagram
Uniaxial tension
Plane strain tension
Forming limit
Plastic
Elastic
Pure shear
Equibiaxial tension
Uniaxial compression
Major strain
Minor strain
Major and minor stress diagram
Uniaxial tension
Pure shear
Equibiaxial tension
Uniaxial compression
Uniaxial tension
Plastic
Elastic
Biaxial compression
Uniaxial compression
Pure shear
Major stress (MPa)
Minor stress (MPa)

(a)

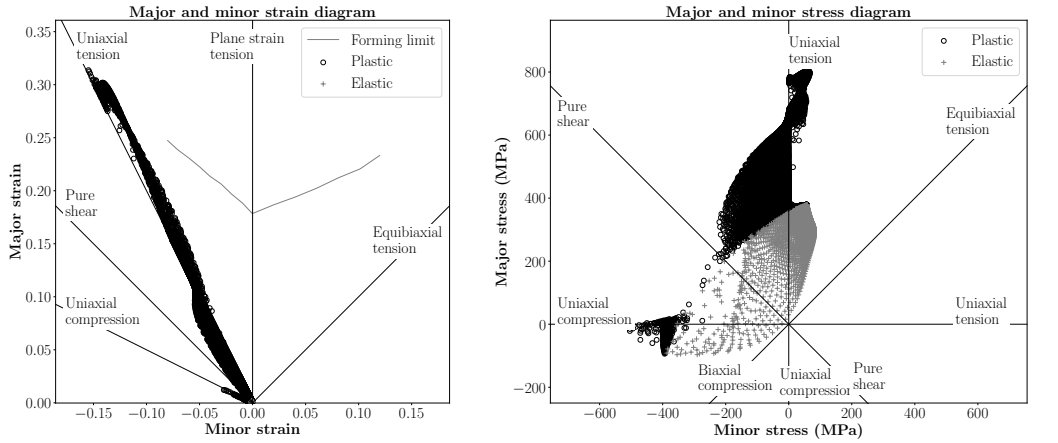
Major and minor strain diagram
Uniaxial tension
Plane strain tension
Forming limit
Plastic
Elastic
Pure shear
Equibiaxial tension
Uniaxial compression
Major strain
Minor strain
Major and minor stress diagram
Uniaxial tension
Plastic
Elastic
Pure shear
Equibiaxial tension
Uniaxial compression
Uniaxial tension
Biaxial compression
Uniaxial compression
Pure shear
Major stress (MPa)
Minor stress (MPa)

(b)

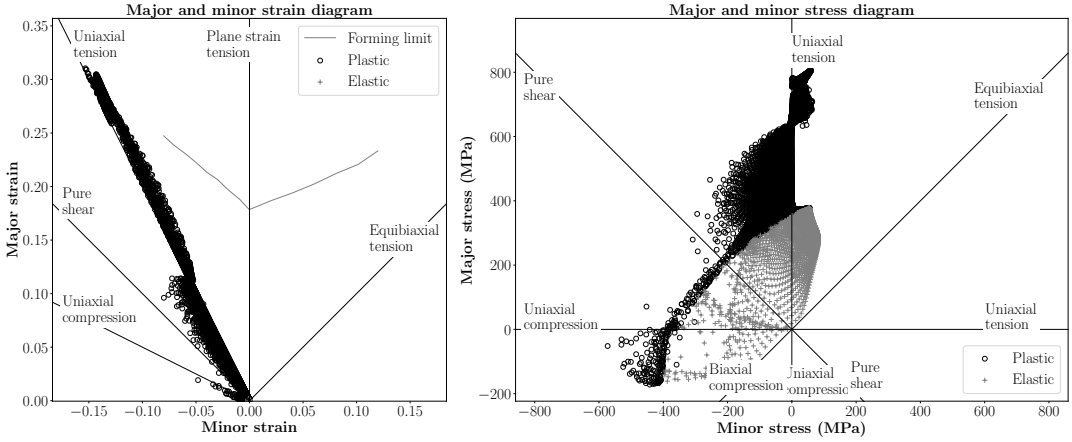
Major and minor strain diagram
Uniaxial tension
Plane strain tension
Forming limit
Plastic
Elastic
Pure shear
Equibiaxial tension
Uniaxial compression
Major strain
Minor strain
Major and minor stress diagram
Uniaxial tension
Pure shear
Equibiaxial tension
Uniaxial compression
Uniaxial tension
Plastic
Elastic
Biaxial compression
Pure shear
Major stress (MPa)
Minor stress (MPa)

(c)

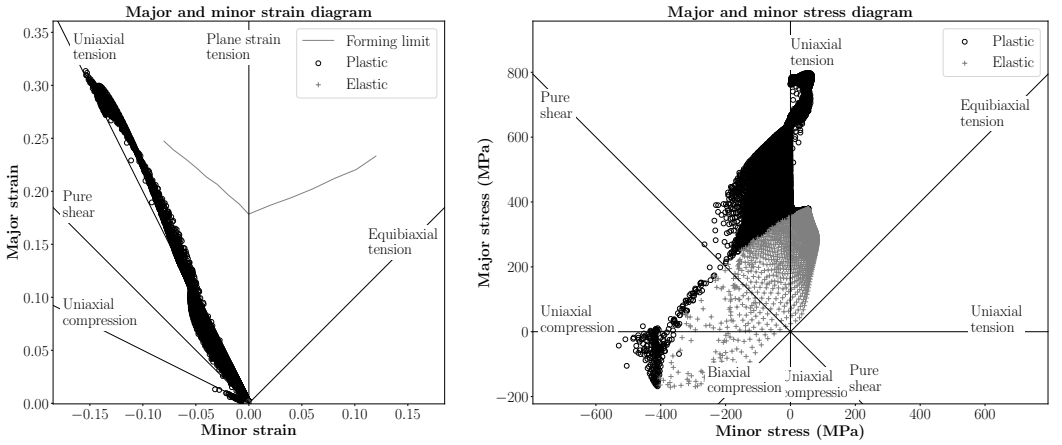
Major and minor strain diagram
Uniaxial tension
Plane strain tension
Forming limit
Plastic
Elastic
Pure shear
Equibiaxial tension
Uniaxial compression
Major strain
Minor strain
Major and minor stress diagram
Uniaxial tension
Plastic
Elastic
Pure shear
Equibiaxial tension
Uniaxial compression
Uniaxial tension
Biaxial compression
Uniaxial compressio
Pure shear
Major stress (MPa)
Minor stress (MPa)

(d)

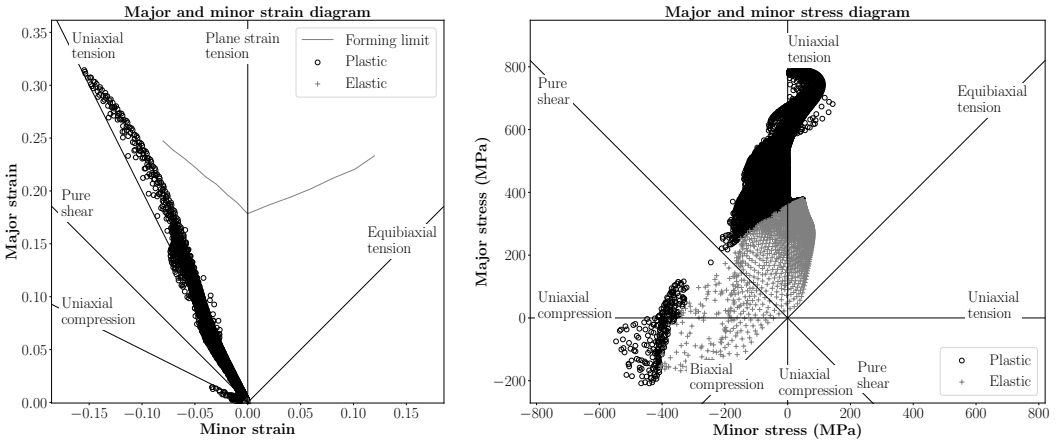
Major and minor strain diagram
Uniaxial tension
Plane strain tension
Forming limit
Plastic
Elastic
Pure shear
Equibiaxial tension
Uniaxial compression
Major strain
Minor strain
Major and minor stress diagram
Uniaxial tension
Pure shear
Equibiaxial tension
Uniaxial compression
Uniaxial tension
Biaxial compression
Uniaxial compression
Pure shear
Plastic
Elastic
Major stress (MPa)
Minor stress (MPa)

(e)

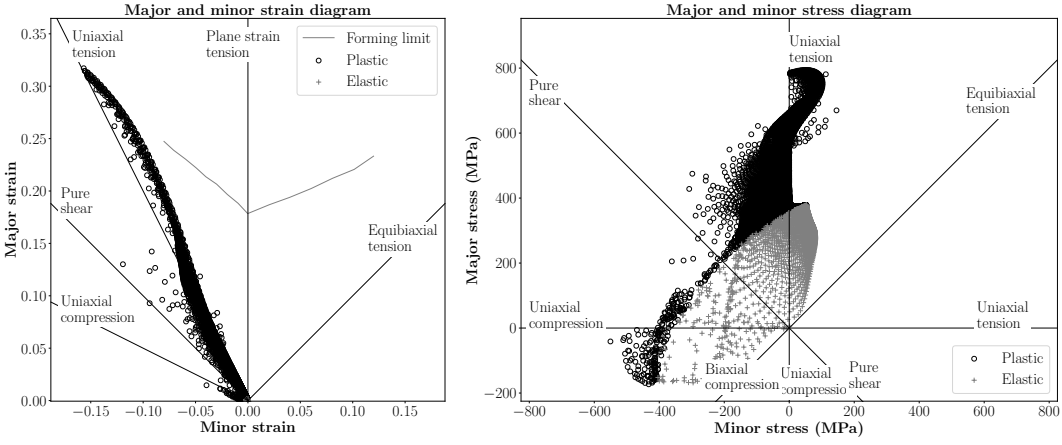
Major and minor strain diagram
Uniaxial tension
Plane strain tension
Forming limit
Plastic
Elastic
Pure shear
Equibiaxial tension
Uniaxial compression
Major strain
Minor strain
Major and minor stress diagram
Uniaxial tension
Pure shear
Equibiaxial tension
Uniaxial compression
Uniaxial tension
Biaxial compression
Uniaxial compressio
Pure shear
Plastic
Elastic
Major stress (MPa)
Minor stress (MPa)

(f)

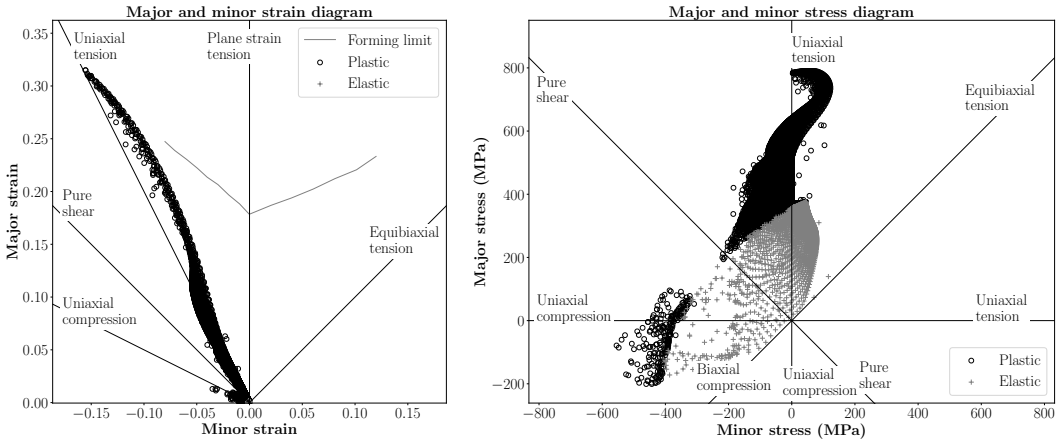

(g)

Figure 3.16: Minor and major strain and stress diagrams at the moment just before rupture, using (a) 5 control points, (b) 4 control points, (c) 6 control points, (d) 8 control points, (e) 10 control points, (f) 12 control points and (g) 14 control points.

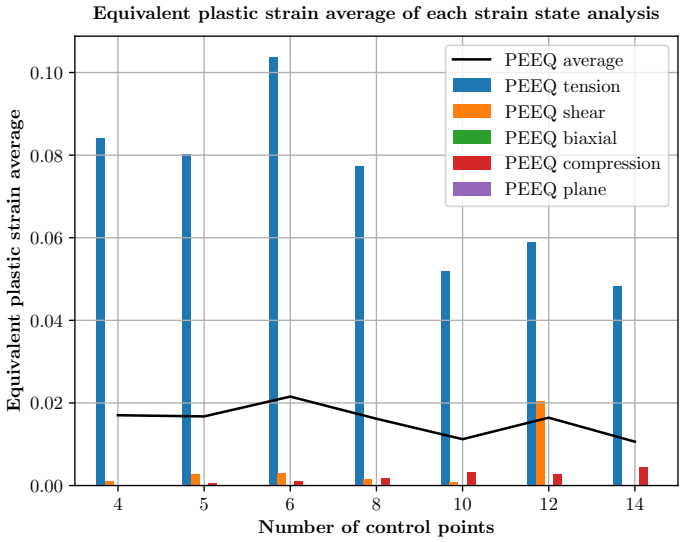

Figure 3.17: Average equivalent plastic strain for each strain state, depending on the number of control points used.

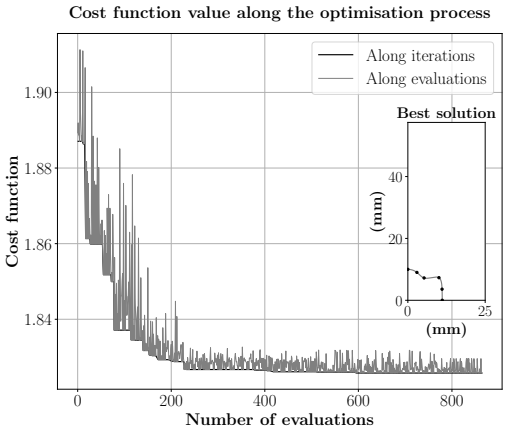
Cost function value along the optimisation process
Along iterations
Along evaluations
Best solution
(mm)
(mm)
Cost function
Number of evaluations

(a)

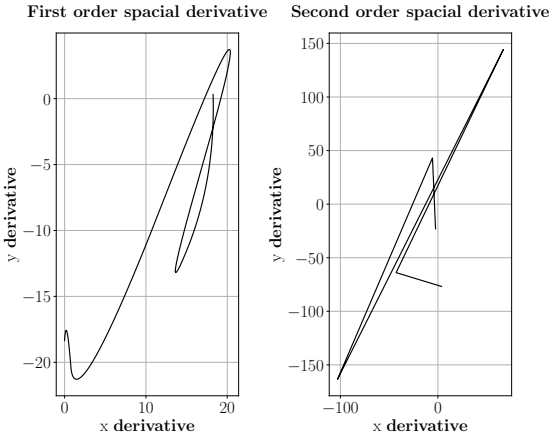
First order spacial derivative
Second order spacial derivative
y derivative
x derivative
y derivative
x derivative

(b)

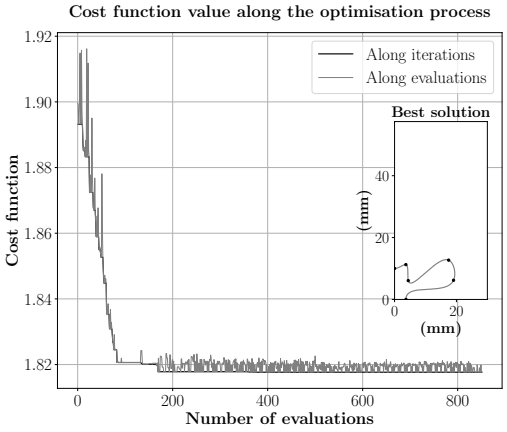
Cost function value along the optimisation process
Along iterations
Along evaluations
Best solution
(mm)
(mm)
Cost function
Number of evaluations

(c)

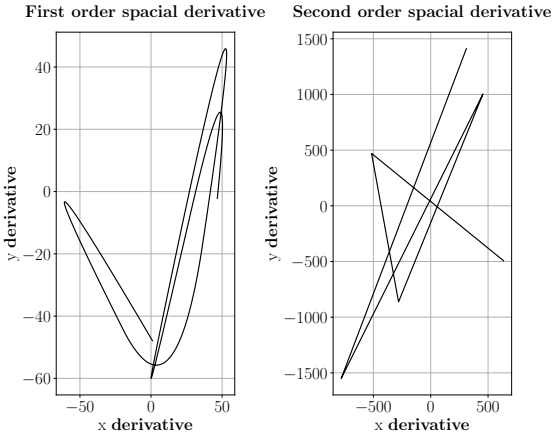
First order spacial derivative
Second order spacial derivative
y derivative
x derivative
y derivative
x derivative

(d)

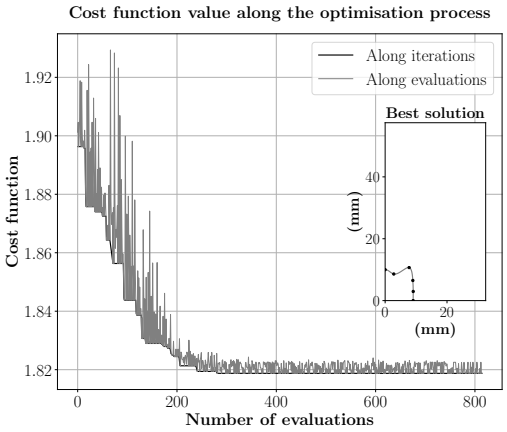
Cost function value along the optimisation process
Along iterations
Along evaluations
Best solution
(mm)
(mm)
Cost function
Number of evaluations

(e)

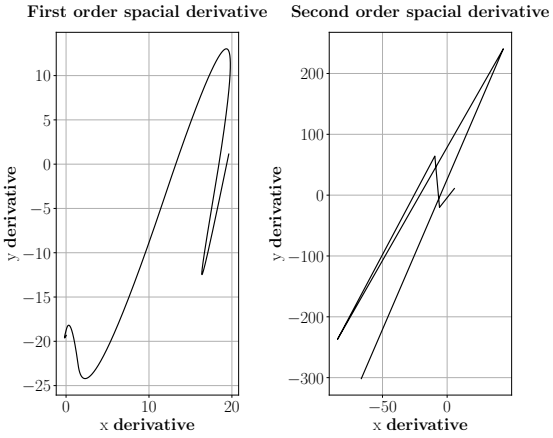
First order spacial derivative
Second order spacial derivative
y derivative
x derivative
y derivative
x derivative

(f)

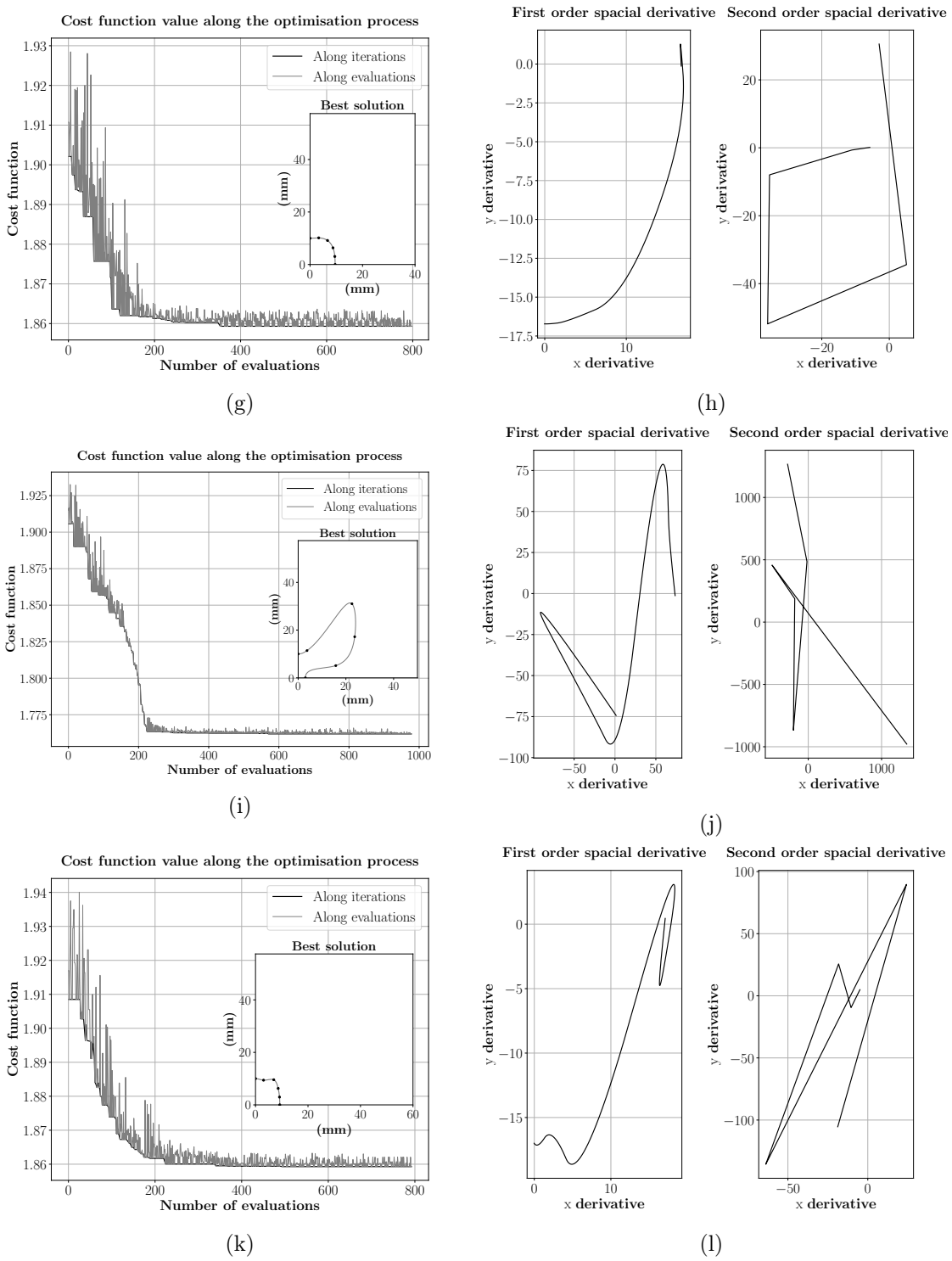

Figure 3.18: Cost function evaluation and best-obtained solution, with a height/width ratio of (a) 5.30, (c) 4.42, (e) 4.08, (g) 3.31, (i) 2.65 and (k) 2.21. Best solution's first and second derivative, with a height/width ratio of (b) 5.30, (d) 4.42, (f) 4.08, (h) 3.31,(j) 2.65 and (l) 2.21.

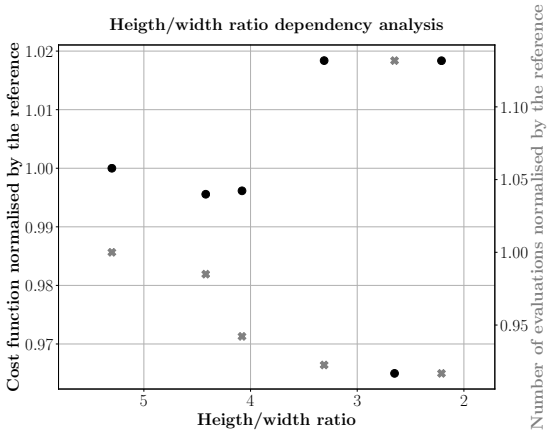

Figure 3.19: Analysis of the optimisation cost function and number of evaluations, depending on the height/width ratio used.

diagrams are identical but have a larger number of points when the height/width ratio is smaller. However, the principal stress' diagram of the 2.65 height/width ratio shows several elements within the equibiaxial tension, facing elastic deformation. Notice that the 4.08 height/width ratio solution exhibits elements with uniaxial tension stress state to the uniaxial compression state with the in-between stress states all covered and presenting plastic deformation.

Concerning the best solutions' average equivalent plastic strain of each considered strain state (see Fig. 3.22) the 4.08 height/width ratio solution shows larger average strain for the tension strain state than the reference solution and all the other tested solutions, whereas the solution obtained with the height/width ratio of 2.21 demonstrates larger average strain for the pure shear and compression strain states.

3.8 Initial solution dependency analysis

Three different initial shapes were tested, as shown in Fig. C.1, with the aim of understating the dependency of the initial solution used in the final solution. The reference solution in this analysis is again the specimen with the circular-shaped interior notch (Fig. C.1a). A solution with a cross-like shaped interior notch (Fig. C.1b) was analysed as initial solution as well as with an ellipse shape's interior notch (Fig. C.1c).

The obtained cost function value along each evaluation and iteration is depicted in Fig. 3.23, for each analysis, as well as the final solution obtained from each initial solution and its first and second spline derivatives. The three optimisation processes finished successfully with a similar number of evaluations, resulting in a similar computational time.

The initial solution that reached the best cost function value was the specimen with the ellipse-shaped interior notch, with approximately 1.786, whereas the reference solution (circular shaped interior notch) reached 1.826. The cross-like shaped interior notch solution achieved approximately 1.864 as cost function value. In terms of cost function variation, the larger result was with the cross-like as an interior notch.

Concerning the resulting splines, it is confirmed the C^1 continuity in both symmetries,

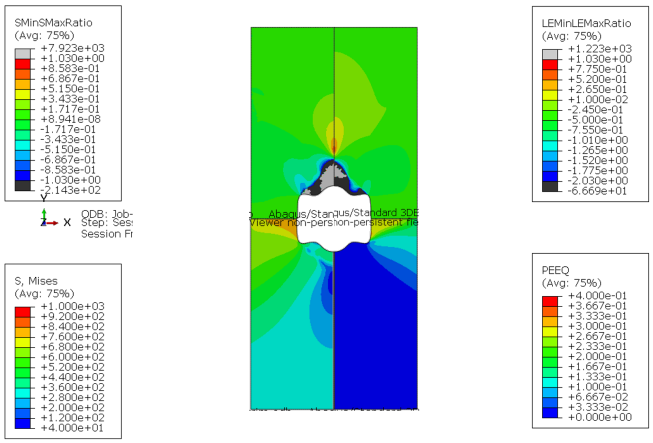
SMinSMaxRatio
(Avg: 75%)
+7.923e+03
+1.030e+00
+8.583e-01
+6.867e-01
+5.150e-01
+3.433e-01
+1.717e-01
+8.941e-08
-1.717e-01
-3.433e-01
-5.150e-01
-6.867e-01
-8.583e-01
-1.030e+00
-2.143e+02
S, Mises
(Avg: 75%)
+1.000e+03
+9.200e+02
+8.400e+02
+7.600e+02
+6.800e+02
+6.000e+02
+5.200e+02
+4.400e+02
+3.600e+02
+2.800e+02
+2.000e+02
+1.200e+02
+4.000e+01
LEMinLEMaxRatio
(Avg: 75%)
+1.223e+03
+1.030e+00
+7.750e-01
+5.200e-01
+2.650e-01
+1.000e-02
-2.450e-01
-5.000e-01
-7.550e-01
-1.010e+00
-1.265e+00
-1.520e+00
-1.775e+00
-2.030e+00
-6.669e+01
PEEQ
(Avg: 75%)
+4.000e-01
+3.667e-01
+3.333e-01
+3.000e-01
+2.667e-01
+2.333e-01
+2.000e-01
+1.667e-01
+1.333e-01
+1.000e-01
+6.667e-02
+3.333e-02
+0.000e+00

(a)

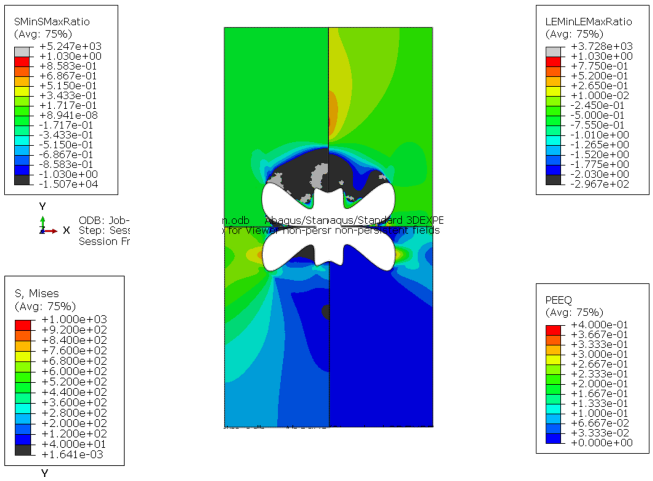
SMinSMaxRatio
(Avg: 75%)
+5.247e+03
+1.030e+00
+8.583e-01
+6.867e-01
+5.150e-01
+3.433e-01
+1.717e-01
+8.941e-08
-1.717e-01
-3.433e-01
-5.150e-01
-6.867e-01
-8.583e-01
-1.030e+00
-1.507e+04
S, Mises
(Avg: 75%)
+1.000e+03
+9.200e+02
+8.400e+02
+7.600e+02
+6.800e+02
+6.000e+02
+5.200e+02
+4.400e+02
+3.600e+02
+2.800e+02
+2.000e+02
+1.200e+02
+4.000e+01
+1.641e-03
LEMinLEMaxRatio
(Avg: 75%)
+3.728e+03
+1.030e+00
+7.750e-01
+5.200e-01
+2.650e-01
+1.000e-02
-2.450e-01
-5.000e-01
-7.550e-01
-1.010e+00
-1.265e+00
-1.520e+00
-1.775e+00
-2.030e+00
-2.967e+02
PEEQ
(Avg: 75%)
+4.000e-01
+3.667e-01
+3.333e-01
+3.000e-01
+2.667e-01
+2.333e-01
+2.000e-01
+1.667e-01
+1.333e-01
+1.000e-01
+6.667e-02
+3.333e-02
+0.000e+00

(b)

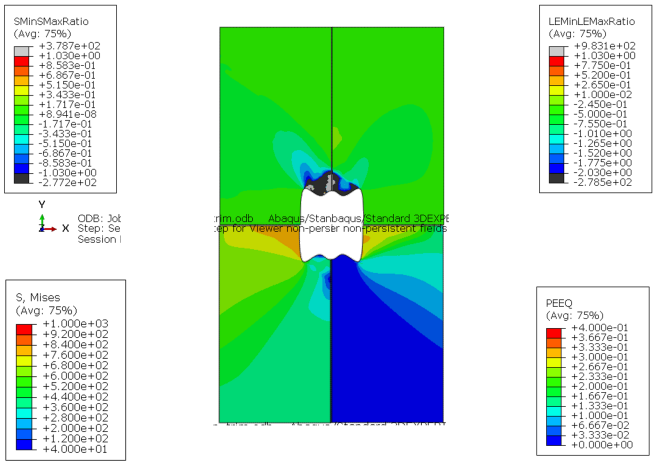
SMinSMaxRatio
(Avg: 75%)
+3.787e+02
+1.030e+00
+8.583e-01
+6.867e-01
+5.150e-01
+3.433e-01
+1.717e-01
+8.941e-08
-1.717e-01
-3.433e-01
-5.150e-01
-6.867e-01
-8.583e-01
-1.030e+00
-2.772e+02
S, Mises
(Avg: 75%)
+1.000e+03
+9.200e+02
+8.400e+02
+7.600e+02
+6.800e+02
+6.000e+02
+5.200e+02
+4.400e+02
+3.600e+02
+2.800e+02
+2.000e+02
+1.200e+02
+4.000e+01
LEMinLEMaxRatio
(Avg: 75%)
+9.831e+02
+1.030e+00
+7.750e-01
+5.200e-01
+2.650e-01
+1.000e-02
-2.450e-01
-5.000e-01
-7.550e-01
-1.010e+00
-1.265e+00
-1.520e+00
-1.775e+00
-2.030e+00
-2.785e+02
PEEQ
(Avg: 75%)
+4.000e-01
+3.667e-01
+3.333e-01
+3.000e-01
+2.667e-01
+2.333e-01
+2.000e-01
+1.667e-01
+1.333e-01
+1.000e-01
+6.667e-02
+3.333e-02
+0.000e+00

(c)

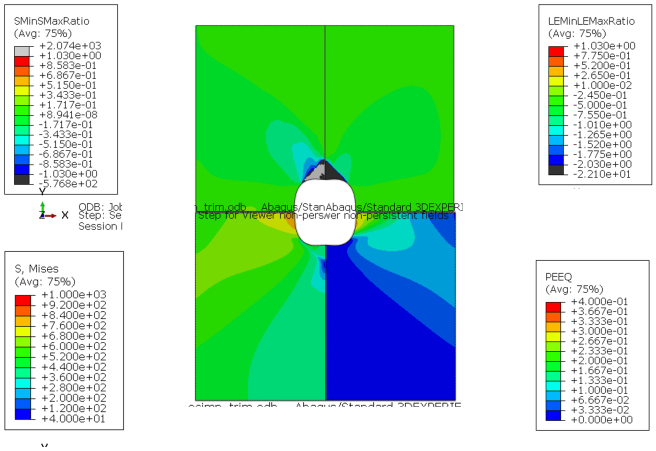

(d)

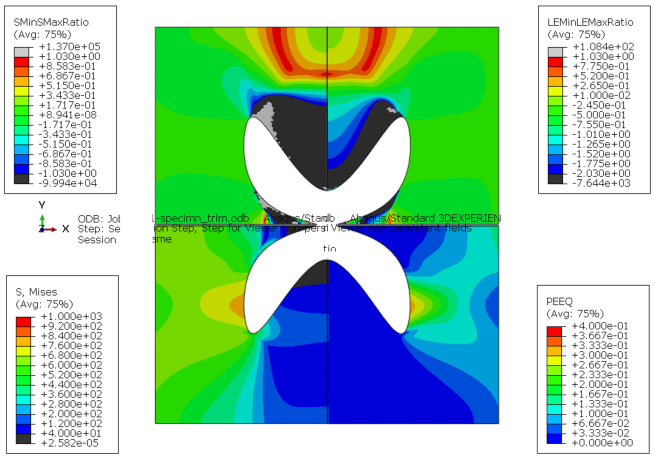

(e)

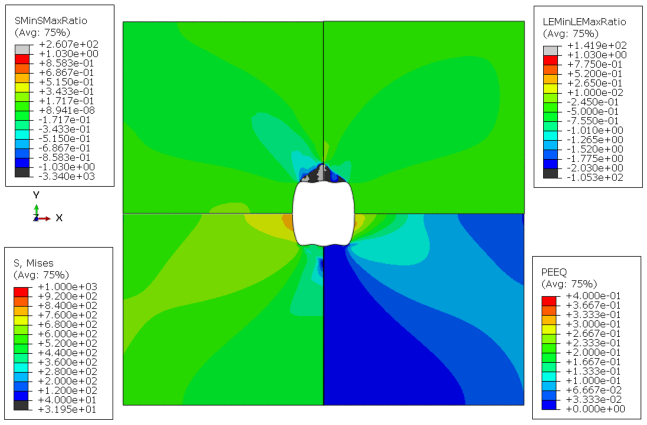

(f)

Figure 3.20: Best obtained solutions' minor and major stress (SMinSMaxRatio) and strain ratios (LEMinLEMaxRatio), von Mises stress (S, Mises) and equivalent plastic strain (PEEQ) at the moment just before rupture, with a height/width ratio of (a) 5.30, (b) 4.42, (c) 4.08, (d) 3.31, (e) 2.65 and (f) 2.21.

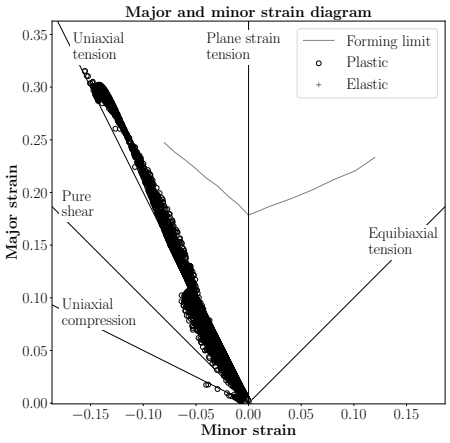
Major and minor strain diagram
Uniaxial tension
Plane strain tension
Forming limit
Plastic
Elastic
Pure shear
Equibiaxial tension
Uniaxial compression
Major strain
Minor strain

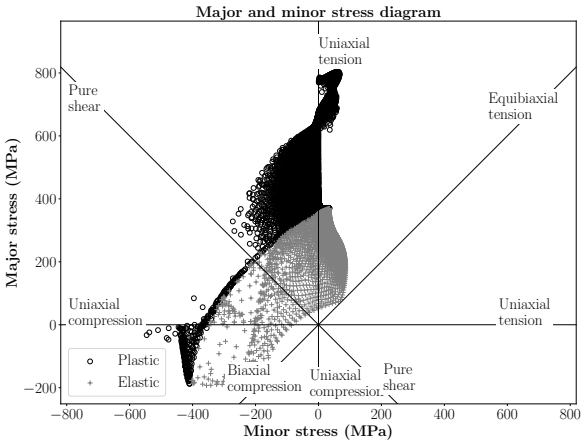
Major and minor stress diagram
Uniaxial tension
Pure shear
Equibiaxial tension
Uniaxial compression
Uniaxial tension
Plastic
Elastic
Biaxial compression
Pure shear
Major stress (MPa)
Minor stress (MPa)

(a)

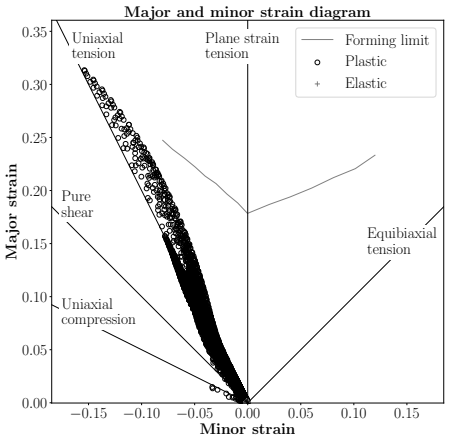
Major and minor strain diagram
Uniaxial tension
Plane strain tension
Forming limit
Plastic
Elastic
Pure shear
Equibiaxial tension
Uniaxial compression
Major strain
Minor strain

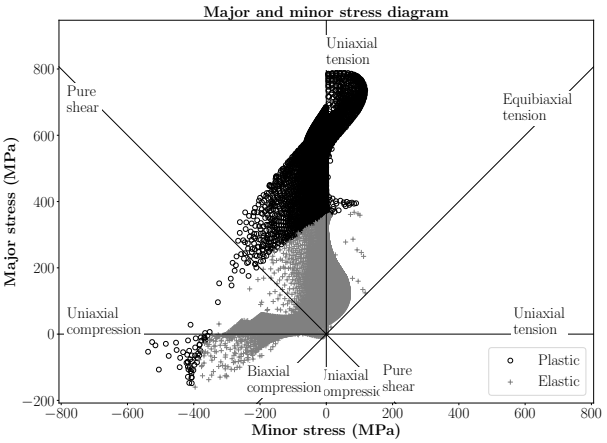
Major and minor stress diagram
Uniaxial tension
Pure shear
Equibiaxial tension
Uniaxial compression
Uniaxial tension
Plastic
Elastic
Biaxial compression
Pure shear
Major stress (MPa)
Minor stress (MPa)

(b)

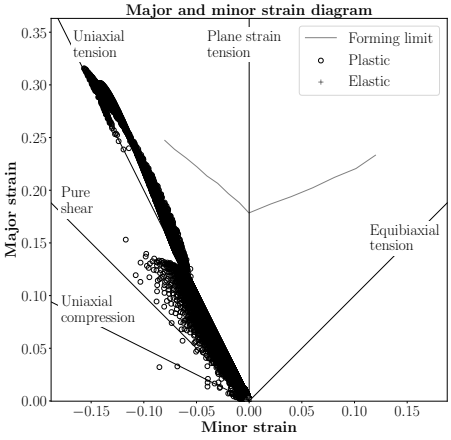
Major and minor strain diagram
Uniaxial tension
Plane strain tension
Forming limit
Plastic
Elastic
Pure shear
Equibiaxial tension
Uniaxial compression
Major strain
Minor strain

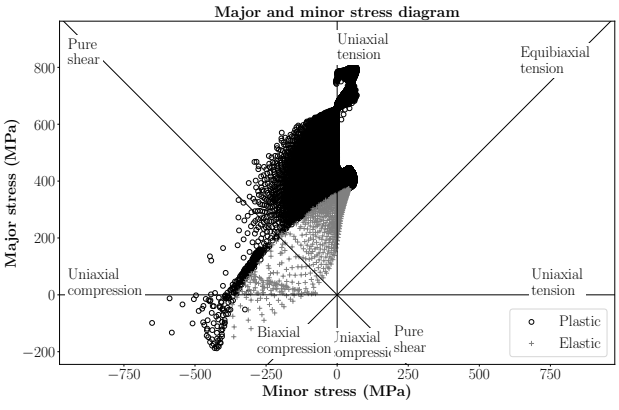
Major and minor stress diagram
Uniaxial tension
Pure shear
Equibiaxial tension
Uniaxial compression
Uniaxial tension
Plastic
Elastic
Biaxial compression
Pure shear
Major stress (MPa)
Minor stress (MPa)

(c)

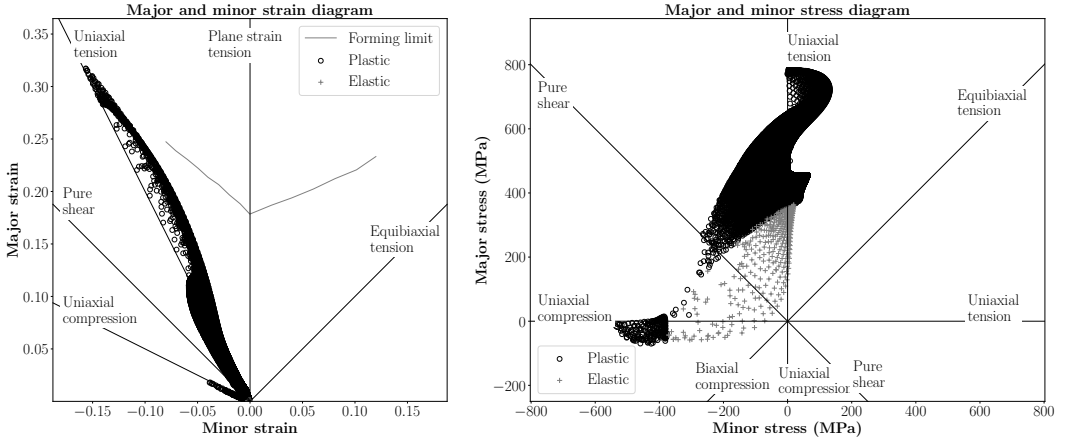

(d)

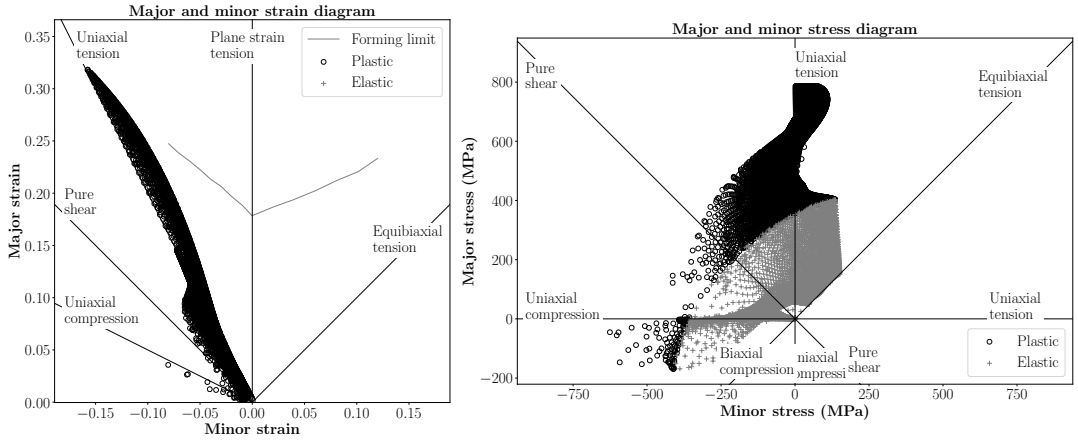

(e)

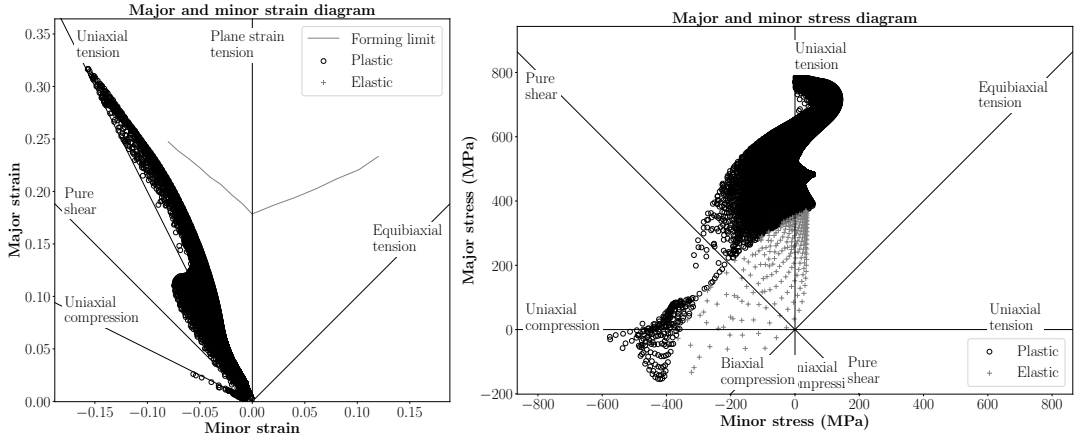

(f)

Figure 3.21: Minor and major strain and stress diagrams at the moment just before rupture, with a height/width ratio of (a) 5.30, (b) 4.42, (c) 4.08, (d) 3.31, (e) 2.65 and (f) 2.21.

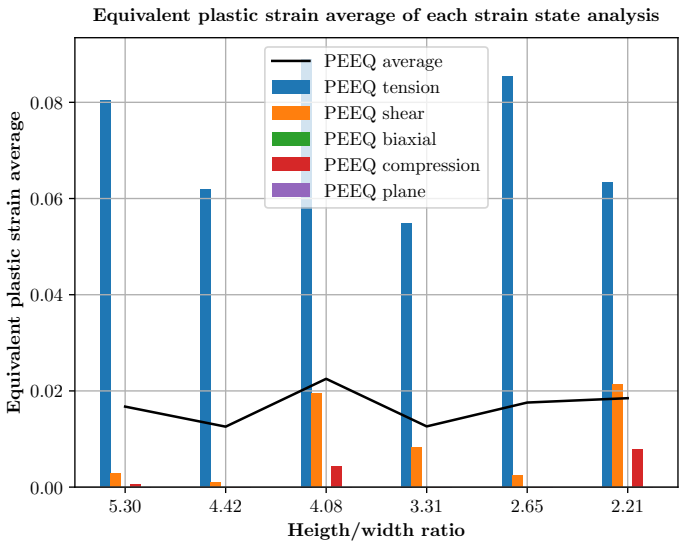

Figure 3.22: Average equivalent plastic strain for each strain state, depending on the height/width ratio.

except for the ellipse solution that loses its C^1 continuity in the horizontal symmetry when converted to Abaqus, as can be seen in Fig. 3.25c. However, theoretically this condition is verified (Fig. 3.23f).

Different interior notch final shapes were obtained out of different initial solutions in the optimisation procedure, so the design method depends on it. A possible way to avoid this situation is to use a multi-starting algorithm, giving several different initial solutions to analyse, instead of just one. However, que computational effort required would be very large.

It is presented the normalised best cost function value and normalised number of evaluations of each analysis in Fig. 3.24. The solution obtained with the initial ellipse shape generated a better cost function but required a larger number of evaluations.

In Fig. 3.25 it can be seen the minor and major stress (SMinSMaxRatio) and strain ratios (LEMinLEMaxRatio), von Mises stress (S, Mises) and equivalent plastic strain (PEEQ) at the moment just before rupture of the final achieved solutions. In terms of minor and major strain and stress ratios, it can be noticed again in all solutions that the surrounding top and bottom of the interior notch show shear and compression state, whereas the majority of the specimen reveals tension state. The maximum PEEQ and von Mises stress results are very similar in the three shapes. The solution originated out of the cross-like shaped interior notch shows a smaller number of elements subjected to plastic strain, whereas the solution achieved with the ellipse interior notch has a very different PEEQ and von Mises stress distribution along its surface. None of the solutions reveal possible problems regarding the interference of the grips with the material plastic deformation.

In Fig. 3.26 it can be seen the minor and major strain and stress diagrams for the three final solutions. The circular and cross-like interior notch strain and stress states are relatively similar, while the ellipse interior notch demonstrates more differences.

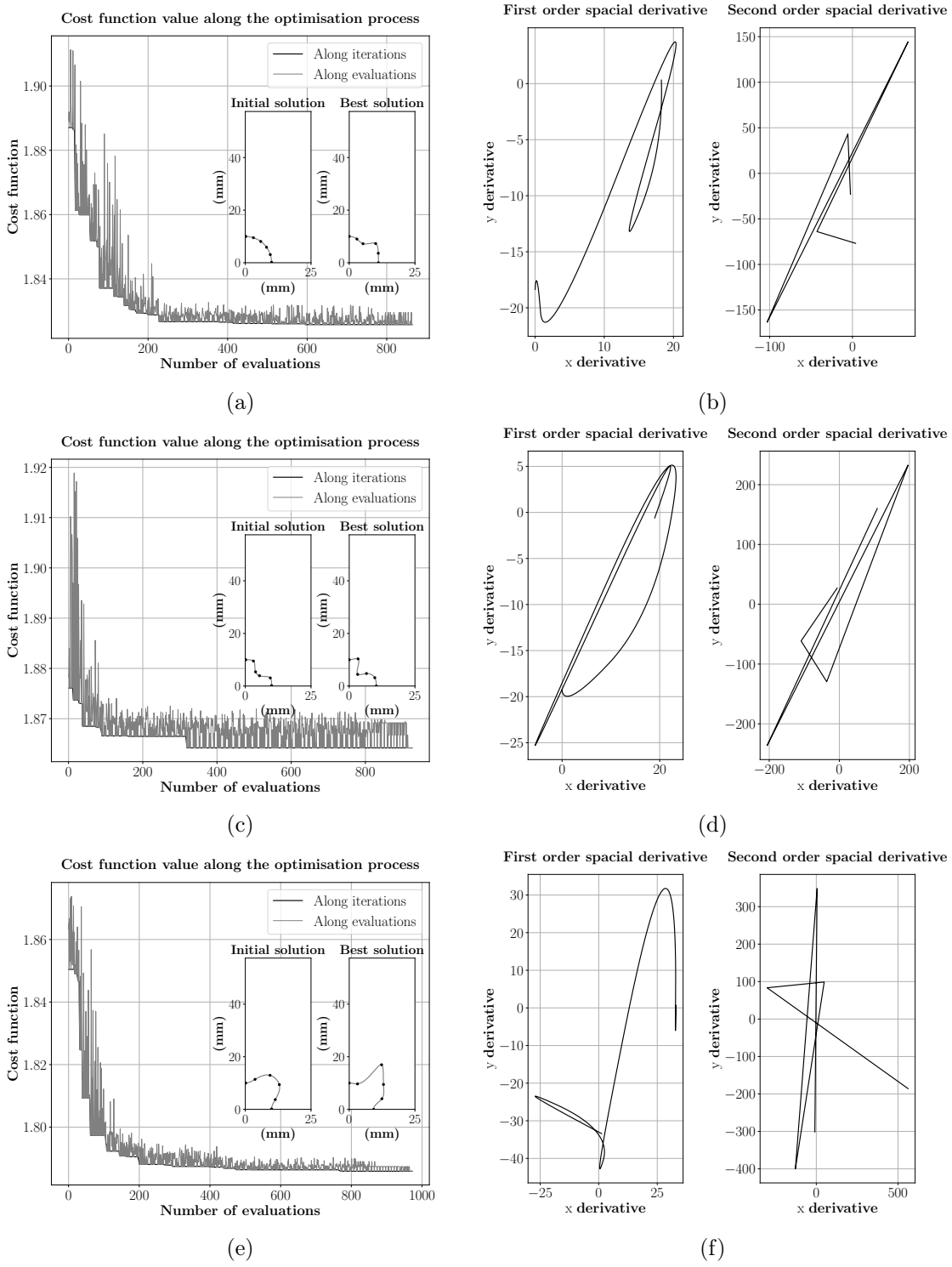

Figure 3.23: Evaluation of the cost function value, initial and best solutions obtained with (a) the circular interior notch, (c) the cross-like interior notch, and (e) the ellipse-shaped interior notch as initial solution. Best solution's first and second derivative for (b) the circular interior notch, (d) the cross-like interior notch and (f) the ellipse-shaped interior notch as initial solution.

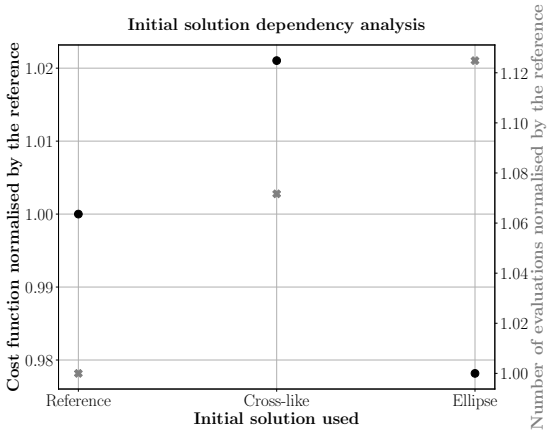

Figure 3.24: Analysis of the optimisation cost function and number of evaluations, depending on the initial solution used.

The obtained average equivalent plastic strain for each strain state is depicted in Fig. 3.27. None of the final solutions has exhibited the plane and biaxial strain states in plasticity. The solution obtained out of the cross-like shaped interior notch shows the same strain states as the reference solution, but with smaller amounts. Although the solution achieved with the ellipse interior notch has a better cost function value, it does not exhibit the compression strain state with plastic deformation. However, the equivalent plastic strain of the different strain states is larger than the reference, as well as its mean value.

It is concluded that the optimisation process with this algorithm is dependent on the initial solution. A multi-starting strategy might be a way of avoiding local minimums and obtain a better final solution.

3.9 Optimisation algorithm dependency analysis

The way an optimisation procedure evolves is crucial for the best solution's finding. The convergence to local minimums dependes on the used optimisation algorithm. So, an optimisation algorithm dependency analysis was performed. The reference solution uses Nelder-Mead method, whereas the other solution uses a differential evolution algorithm. The optimisation procedures' results are depicted in Fig. 3.28. Concerning the evaluations' evolution, the procedure using a differential evolution algorithm, using a population size of 30 and random initial solutions, completes more than 1500 evaluations with no signs of convergence. Although the optimisation process was forced to stop, it showed higher cost function values compared to the reference process. The outcoming best solution was analysed, anyway. All the obtained solutions have spline's C^1 continuity.

In terms of cost function value, the generated solution from the differential evolution algorithm shows a worse evaluation, comparing to the reference solution (Fig. 3.29), even with a large number of the performed evaluations.

The minor and major stress and strain ratios, the von Mises stress and equivalent plastic strain at the moment just before rupture are depicted in 3.30. It is noticeable that

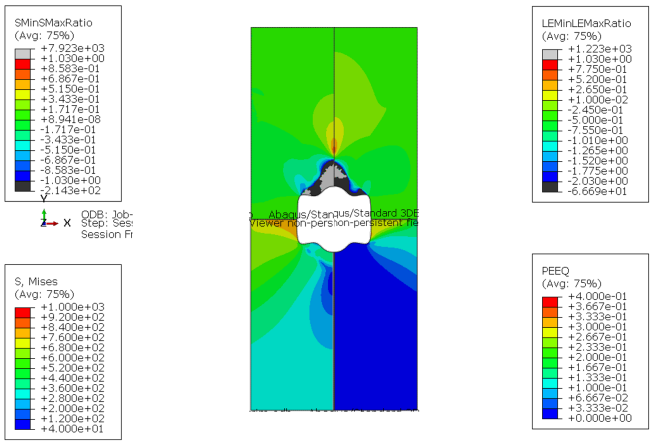

(a)

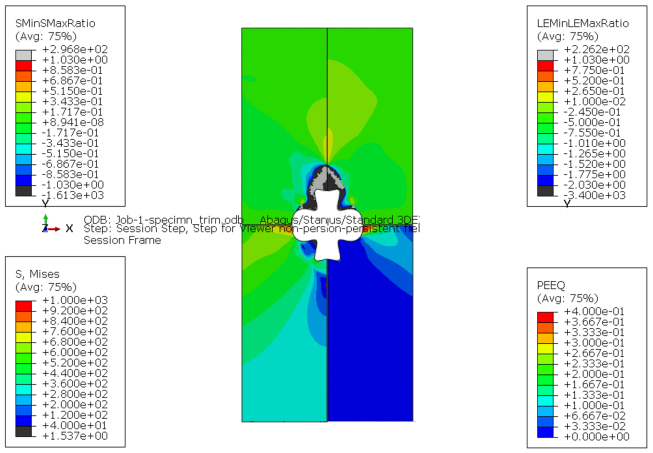

(b)

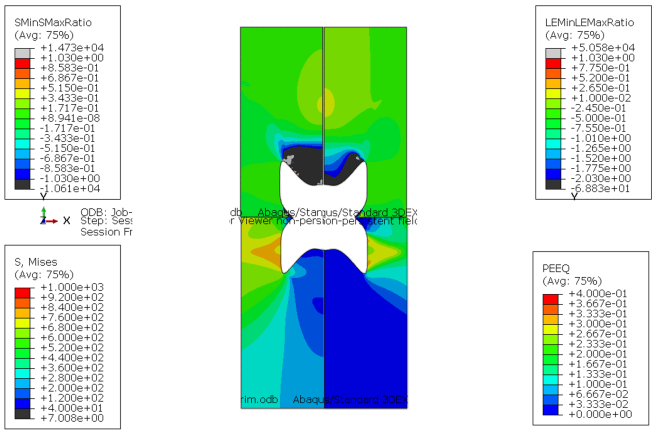

(c)

Figure 3.25: Best obtained solutions' minor and major stress (SMinSMaxRatio) and strain ratios (LEMinLEMaxRatio), von Mises stress (S, Mises) and equivalent plastic strain (PEEQ) at the moment just before rupture, using (a) the circular interior notch, (b) cross-like interior notch and (c) the ellipse interior notch as initial solutions.

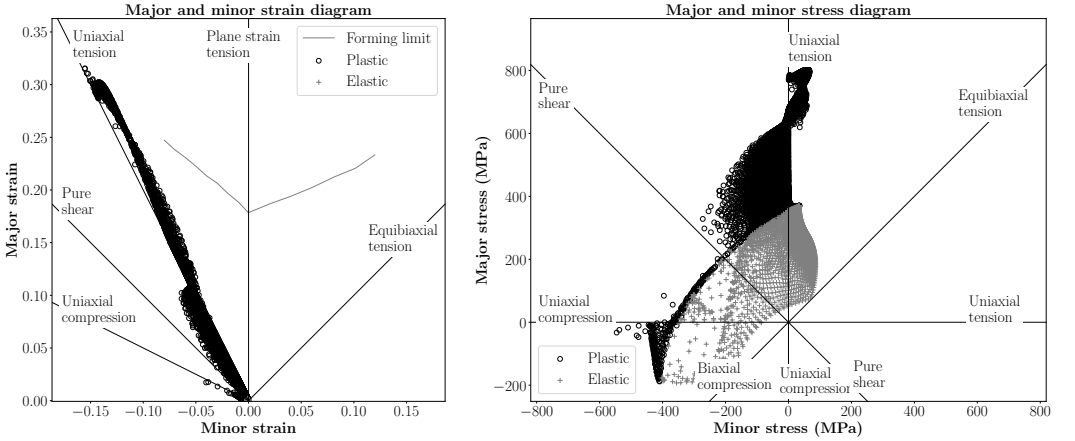

(a)

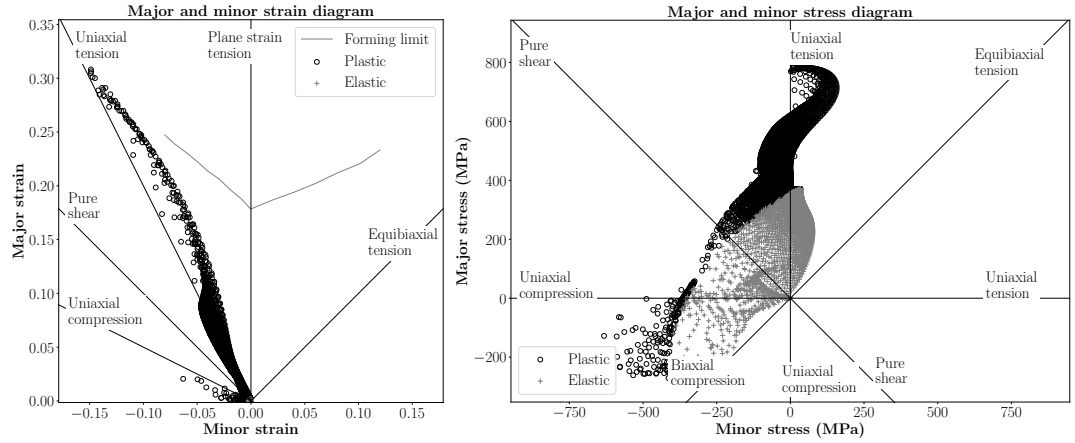

(b)

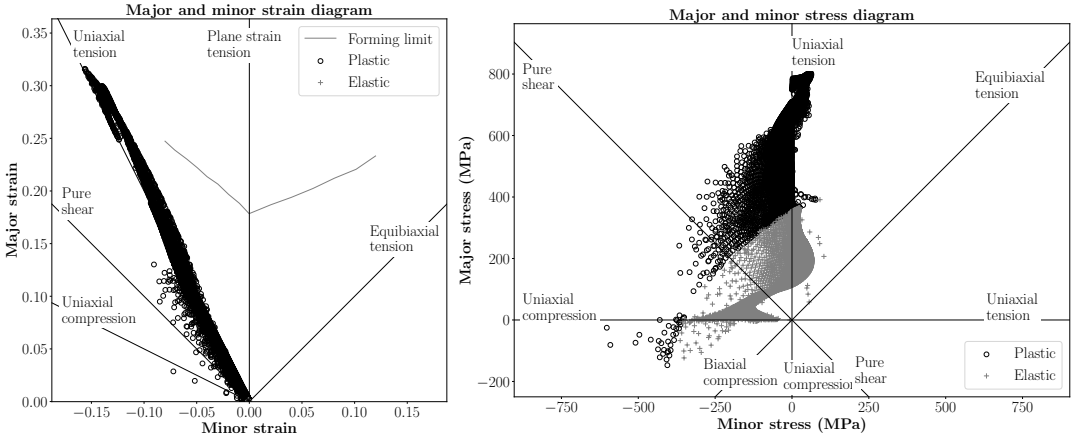

(c)

Figure 3.26: Minor and major strain and stress diagrams at the moment just before rupture, using (a) circular interior notch, (b) cross-like interior notch and (c) the ellipse interior notch as initial solutions.

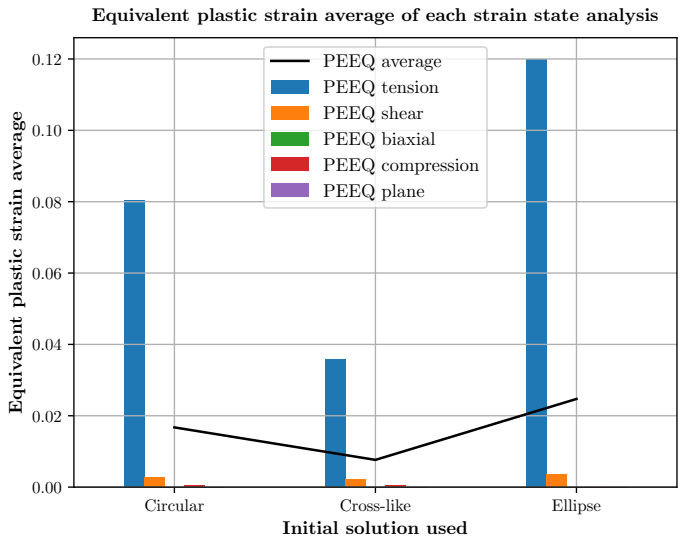

Figure 3.27: Average equivalent plastic strain for each strain state, depending on the initial solution used.

the maximum PEEQ from the solution obtained with the differential evolution algorithm is smaller than the reference and fewer elements are exhibiting plastic deformation. The maximum von Mises stress is also smaller. Concerning the strain and stress ratios, these show a very large predominance of the uniaxial tensile state. Regarding the grips' compatibility, it is verified since the plastic deformation is only observed in the specimen's middle area.

It is also noticeable in the minor and major stress diagram (Fig. 3.31) the predominance of the uniaxial tensile state, as well as the small strains in the minor and major strain diagram.

Regarding the average equivalent plastic strain of the considered strain states, once again the solution obtained with the differential evolution algorithm shows a smaller strain average and fewer strain states, comparing to the reference.

3.10 Analysis of the best parameters combined

Analysing all the performed parameters dependency analysis, it was found the best features of the optimisation procedure, in order to find the most heterogeneous specimen, varying only the spline's control points position. Concerning the finite element mesh, the CPS4R element type with a 0.3 mm edge leads to a good compromise between computational time and accuracy. The heterogeneous criterion used as cost function that outcome in a more interesting solution in terms of strain and stress states variety was the I_{T1} since it exhibited a range of elements with stress states from the uniaxial tension until the uniaxial compression and is previously well-studied indicator from the literature. However, since the I_{T3} also led to good conclusions, it was also evaluated in this final approach.

The fixed point position that outcome in a solution with better cost function value

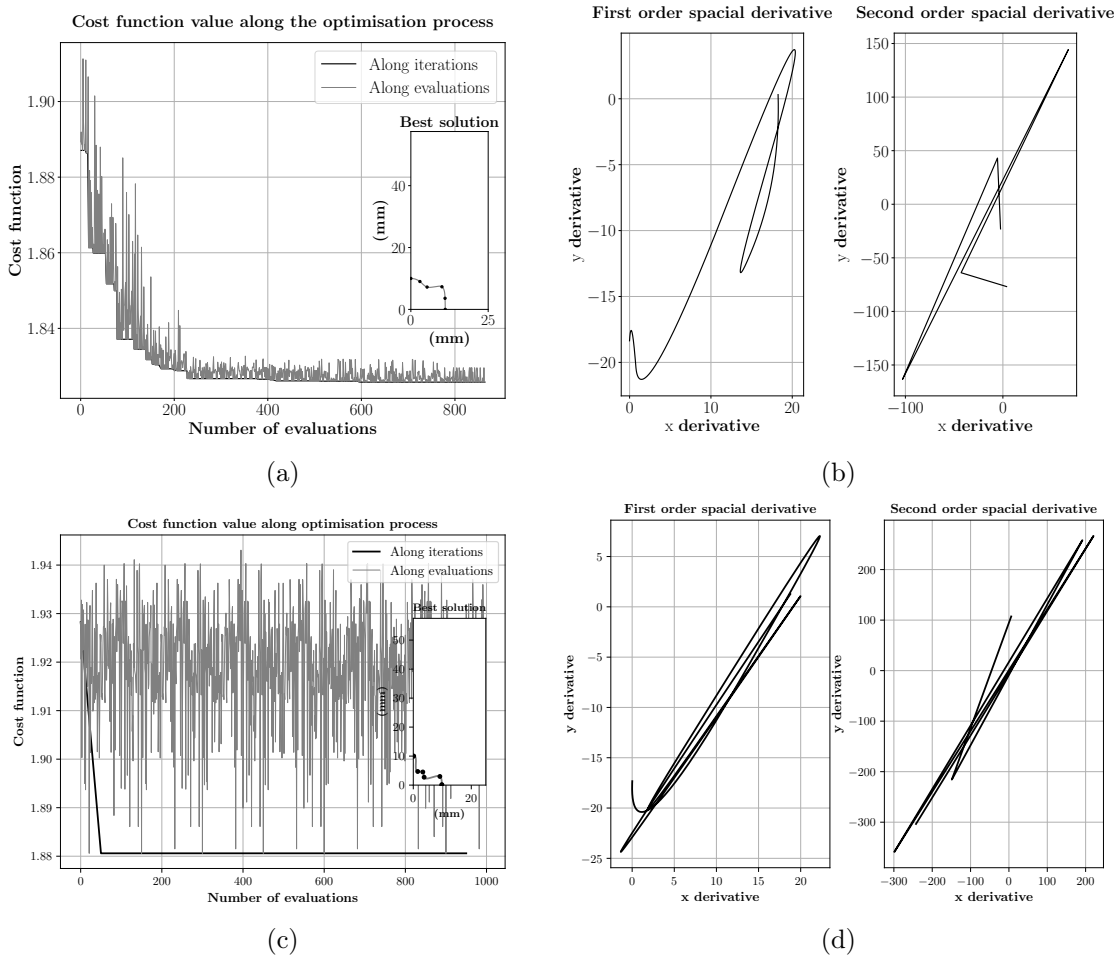

Figure 3.28: Cost function evaluation and best-obtained solution, using (a) Nelder-Mead algorithm and (c) differential evolution algorithm. Best solution's first and second derivative, using (b) Nelder-Mead algorithm and (d) a differential evolution algorithm.

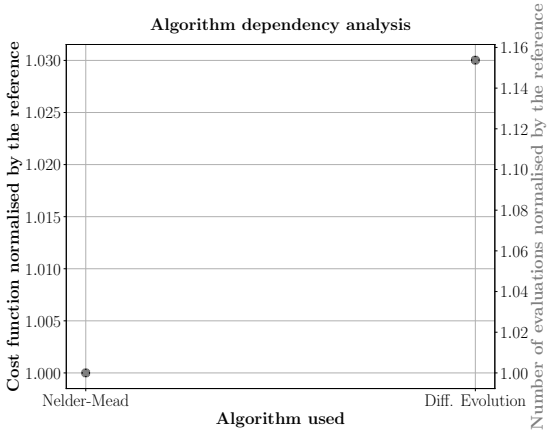

Figure 3.29: Analysis of the optimisation cost function and number of evaluations, depending on the algorithm used.

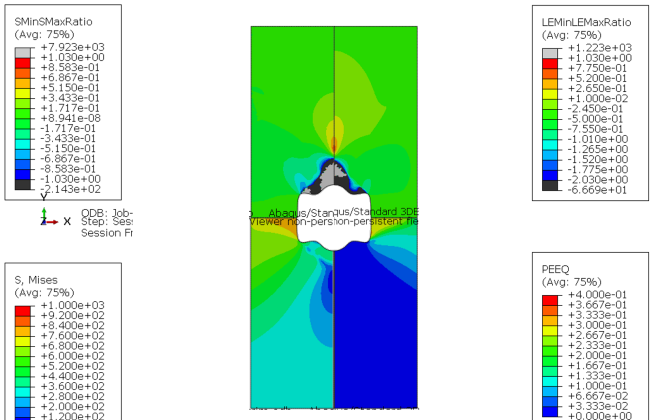

(a)

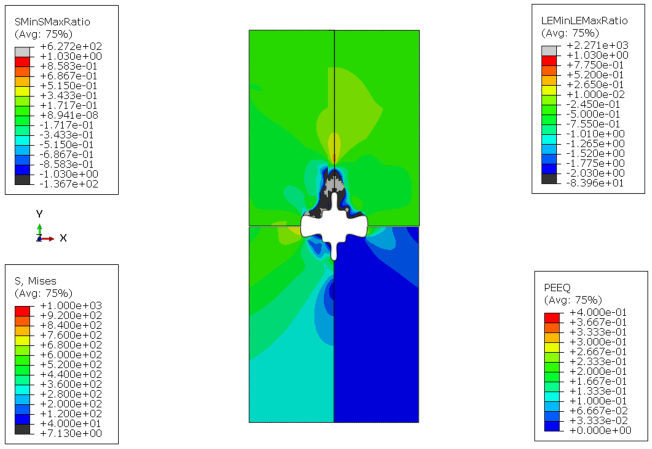

(b)

Figure 3.30: Best obtained solutions' minor and major stress (SMinSMaxRatio) and strain ratios (LEMinLEMaxRatio), von Mises stress (S, Mises) and equivalent plastic strain (PEEQ) at the moment just before rupture, using (a) Nelder-Mead algorithm and (b) differential evolution algorithm.

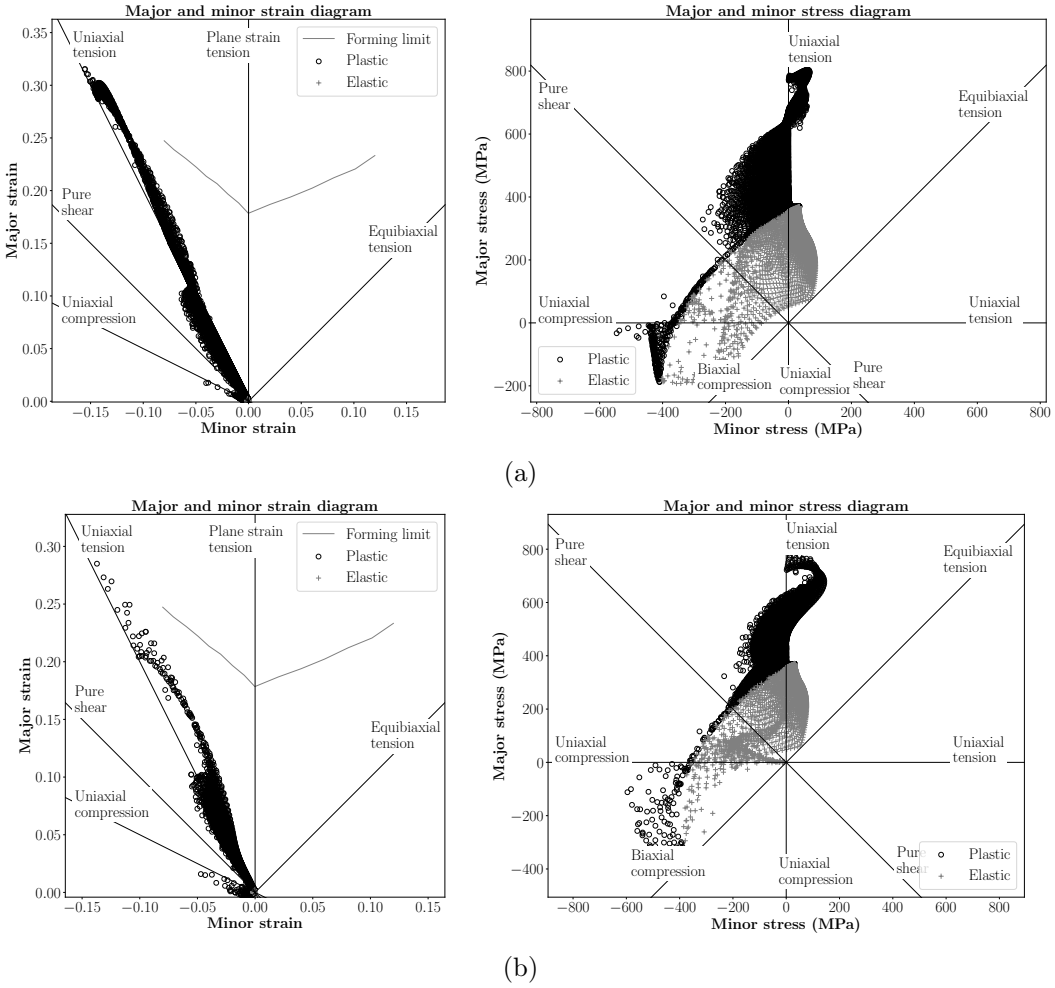

Figure 3.31: Minor and major strain and stress diagrams at the moment just before rupture, using (a) Nelder-Mead algorithm and (b) differential evolution algorithm.

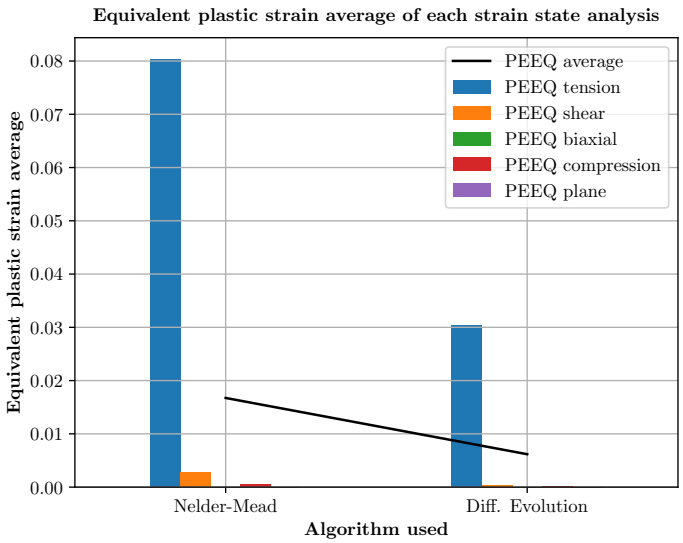

Figure 3.32: Average equivalent plastic strain for each strain state, depending on the algorithm used.

was in the vertical symmetry. The number of curve control points that revealed a more heterogeneous specimen was 6. In terms of height/width ratio, the best is 2.65, which means a 100 mm overall specimen's width.

About the initial solution, a large dependency was seen, when used the Nelder-Mead algorithm. The obtained final solutions were always different from each other, with different cost function values, but similar to each initial solution. It was expected that using a multi-starting method along with a differential evolution algorithm this dependency would be avoided. However, the success of this method was not achieved. So, for the procedure's best parameter's combination, it was used the Nelder-Mead algorithm with the ellipse-shape as initial solution.

Observing Fig. 3.33, it can be noticed that the number of evaluations required for convergence of the solution using I_{T1} is smaller than the usual with the same algorithm. Therefor, a local minimum was probably reached. The process using I_{T3} required a larger number of evaluations, comparing to the previous design process using this cost function. The final solutions show different interior notch shapes, but both show C^1 spline's continuity in the symmetries. The first is just one hole in the middle of the specimen, despite it looks like two.

Comparing the cost function evolution in Fig. 3.34, the solution using I_{T3} presents larger variation as well as larger number of evaluations.

For a better comparison, both solutions were analysed using the non-respective heterogeneous criterions as cost function, as depicted in Tab. 3.2. For both cases, the final solution shows better performance with the respective heterogeneity criterion.

From Fig. 3.35, it can be noted that the solution obtained with the I_{T1} shows larger heterogeneity since it has a larger range of minor and major strain and stress ratios, compared to the one obtained with I_{T3}. Note that, the solution obtained with the I_{T1} indicator shows different strain states in the middle area of the specimen and not just

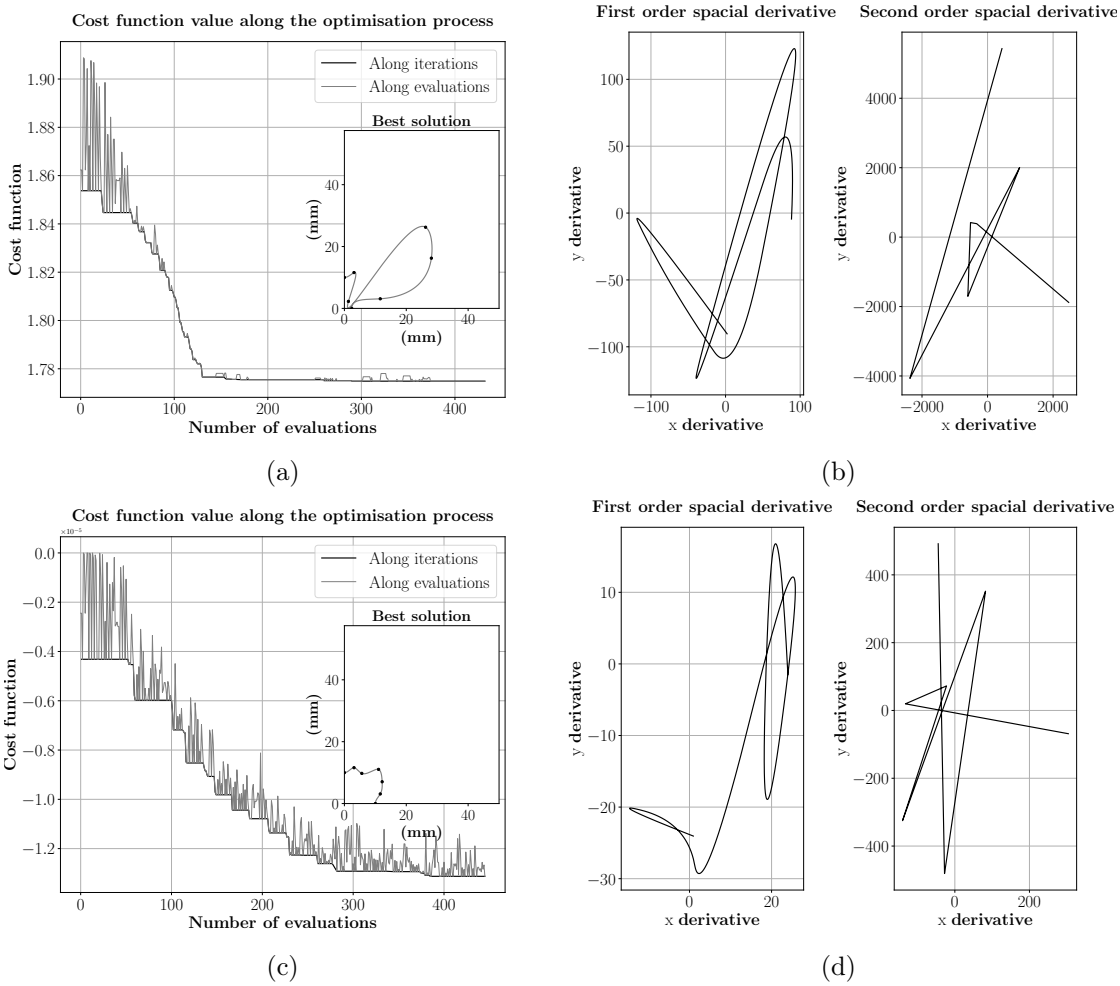

Figure 3.33: Cost function evaluation and best-obtained solution using the best parameters combined and (a) the heterogeneous criterion I_{T1} and (c) I_{T3}. Best solution's first and second derivative using the best parameters combined and (b) the heterogeneous criterion I_{T1} and I_{T3}.

Table 3.2: Cost function value evaluated with the two different heterogeneity indicators for the best solutions obtained with the best parameters combination.

	CF value with I_{T1}	**CF value with I_{T3}**
I_{T1}	1.775	-1.319E-07
I_{T3}	1.857	-1.312E-05

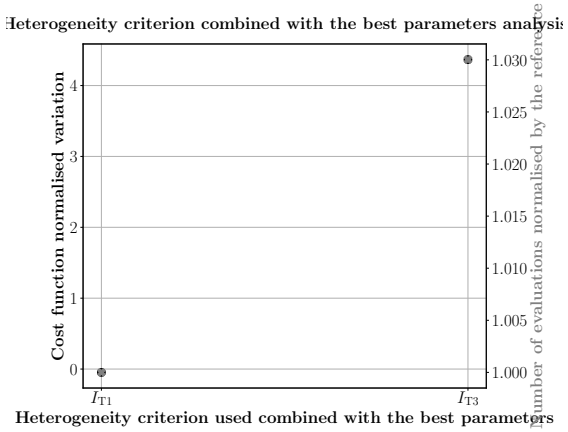

Figure 3.34: Analysis of the optimisation cost function and number of evaluations using the best parameters combined with heterogeneous criterion I_{T1} and I_{T3}.

near the interior notch border. However, it exhibits some elements within the plane strain state in the specimen's top and bottom part, which might interfere with the grips in the experimental data acquisition.

Concerning the strain and stress diagrams of Fig. 3.36, it can be noticed that the obtained solution using I_{T1} shows stress states around the uniaxial tension, uniaxial compression and pure shear in the plastic region. Besides, it also presents equibiaxial tension stress state but with smaller intensities, whereas the solution obtained with I_{T3} shows uniaxial tensile stress state predominance and well-filled range of stress states going from the uniaxial tensile stress state until the uniaxial compression, in the plastic region. There are fewer elements exhibiting strain in the elastic region.

Fig. 3.37 shows with more detail the equivalent plastic strain average of each considered strain state exhibiting in both specimens. It can be noticed that the solution obtained with I_{T3} presents a larger number of strain states in the plastic region. However, the PEEQ average in both cases has a very similar value.

3.11 Best solutions discussion and conclusions

Taking into account the several design optimisation procedures and its analysis in terms of mechanical richness, the most interesting specimen's designs obtained must be highlighted. Those are, from section 3.7, the solution with a height/width ratio of 2.65, from section 3.8, the solution generated by the ellipse interior notch shape as initial solution and, from section 3.10, the solution obtained with the combination of the best analysed parameters and the I_{T1} indicator as cost function. These are depicted in Fig. 3.38.

Their normalised cost function value and number of evaluations are compared in Fig. 3.39. The solution obtained from the procedure with the height/width ratio of 2.65 is the one showing the lowest cost function value. Besides, the same solution required more evaluations for its finding.

Comparing the average equivalent plastic strain of each strain state, depicted in Fig. 3.40, it is noticeable a larger uniaxial tension PEEQ value for the solution obtained from the ellipse initial solution. The pure shear PEEQ value is similar for all solutions.

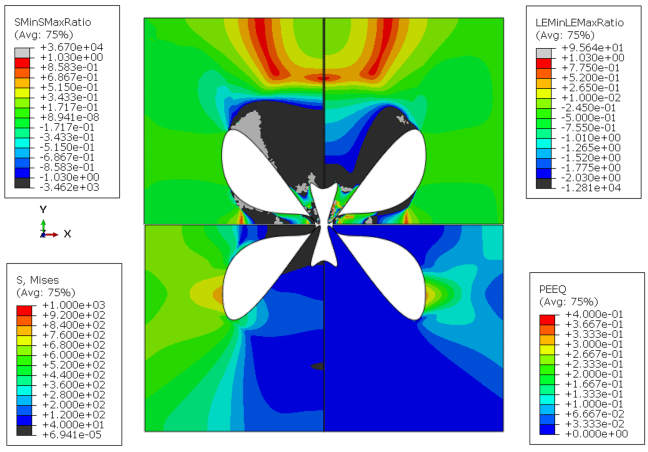

(a)

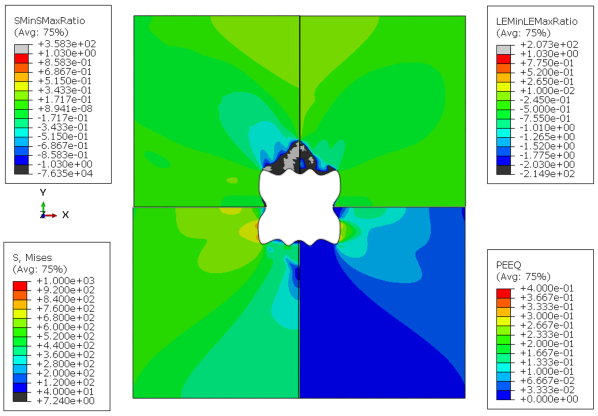

(b)

Figure 3.35: Best obtained solutions' minor and major stress (SMinSMaxRatio) and strain ratios (LEMinLEMaxRatio), von Mises stress (S, Mises) and equivalent plastic strain (PEEQ) at the moment just before rupture using the best parameters combined and (a) the heterogeneous criterion I_{T1} and (b) I_{T3}.

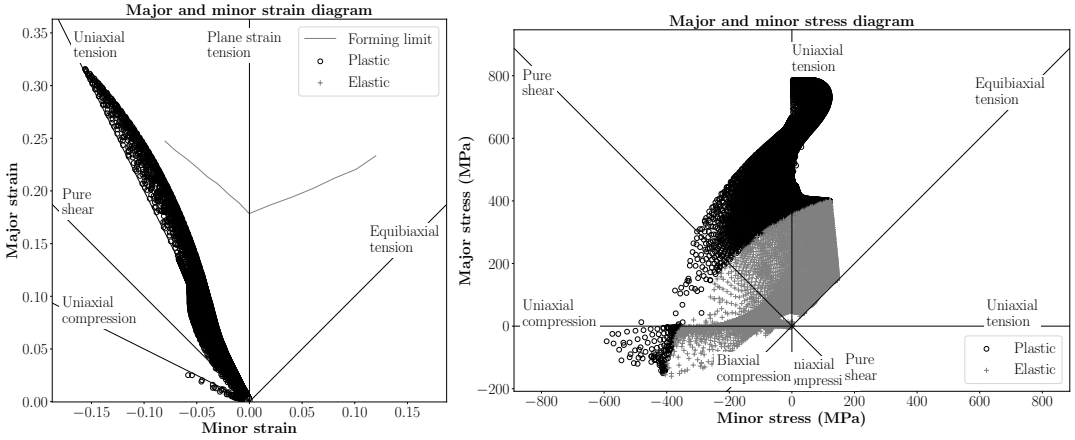

(a)

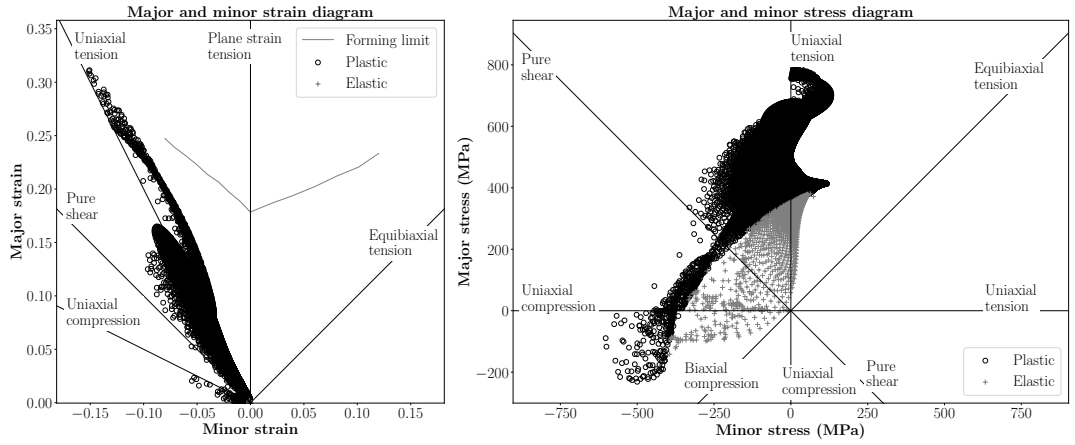

(b)

Figure 3.36: Minor and major strain and stress diagrams at the moment just before rupture using the best parameters combined and (a) the heterogeneous criterion I_{T1} and (b) I_{T3}.

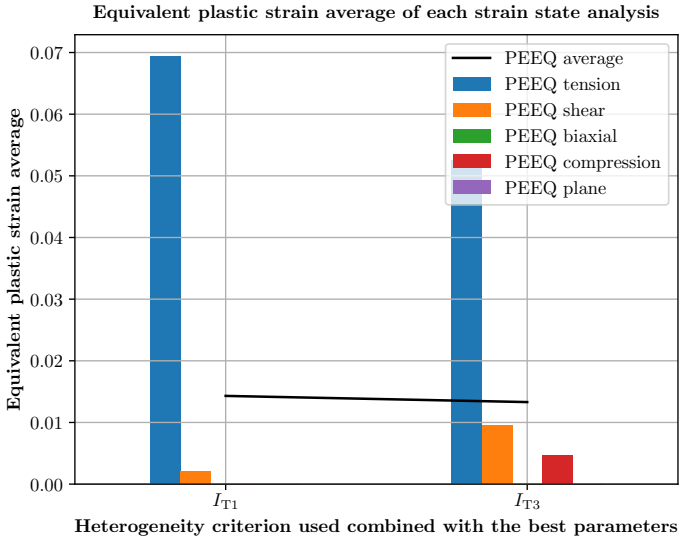

Figure 3.37: Average equivalent plastic strain for each strain state using the best parameters combined and the heterogeneous criterions I_{T1} and I_{T3}.

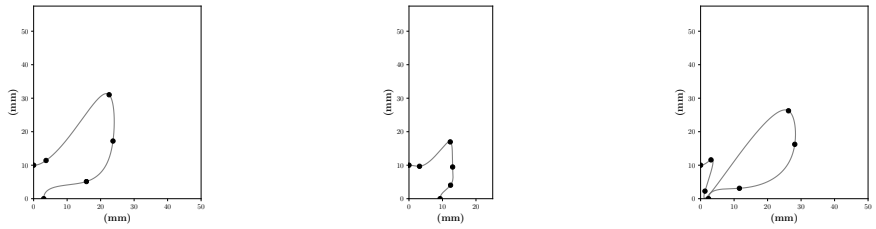

Figure 3.38: Best obtained solutions geometry. Solution obtained with (a) a height/width ratio of 2.65, (b) an interior notch ellipse-shaped as initial solution and (c) the best parameters combined with the I_{T1} indicator as cost function.

Some particularities to emphasize are that the solutions obtained with the height/width ratio of 2.65 and with the best parameters combined with the I_{T1} have a similar geometry. Hence, there minor and major strain and stress states distribution along the specimens' surface are very similar. The three different solutions exhibit uniaxial tension and pure shear states with plastic deformations. Besides, they also present the uniaxial compression state mainly with elastic deformations. The solutions obtained with the height/width ratio of 2.65 and with the best parameters combined also show the equibiaxial and plane states with elastic deformations. It was proved that it is possible to increase the specimen's heterogeneity by using an interior notch shape different from a circular when evaluating it with the I_{T1} indicator. Since a specimen as the reference with an interior circular notch shape achieves a cost function value of 1.889 and the ones mentioned in the present section have a cost function value inferior to 1.789.

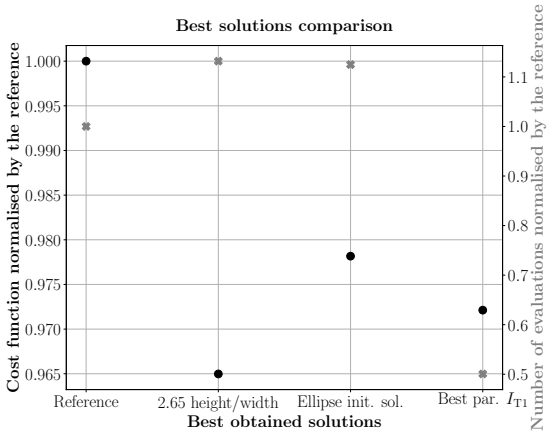

Figure 3.39: Optimisation procedure's cost function normalised by the reference and normalised number of evaluations for the best-obtained solutions.

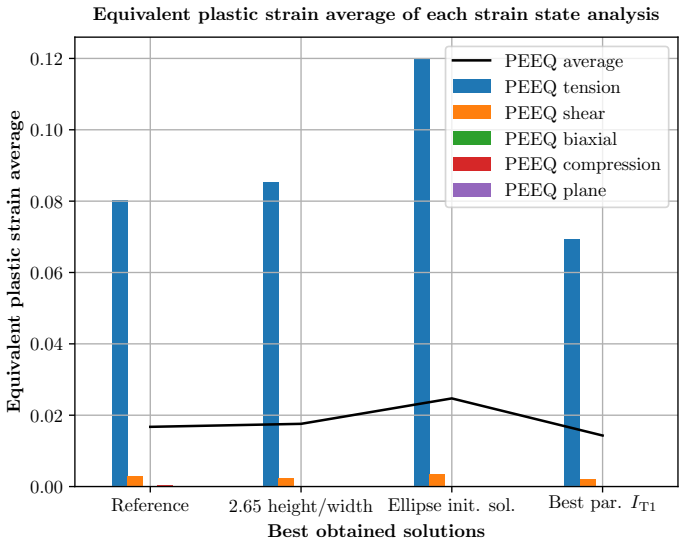

Figure 3.40: Best solutions' equivalent plastic strain average of each considered strain state for the best-obtained solutions.

Chapter 4

Conclusions and future works

4.1 Conclusions

The main goal of the present work is virtually design by optimisation a symmetric heterogeneous specimen for a uniaxial tensile load test. The controlled variables were the curve control points of an interior notch in the middle area of a rectangular specimen. These design constraints allow to develop a future experimental test using a universal tensile test machine with no need of special grips.

First, it was analysed the state of the art in order to know the homogeneous and non-homogeneous tests already developed along with the strain and stress states achieved by them. Then, it was developed a methodology to iteratively perform a virtual uniaxial tensile load test and, by the means of an optimisation algorithm, obtain the richest specimen in terms of mechanical behaviour. A heterogeneity indicator was used to rank the generated solutions in terms of mechanical richness.

Several parameters were analysed, such as the numerical element dimension and type, the optimisation objective function, the specimen's boundary conditions, the number of curve control points, the specimen's height/width ratio, the initial solution as well as the algorithm used for the optimisation procedure. All these parameters demonstrated to have influence in the process and are the reason for local minimums finding and strain and stress states prediction errors. The generated solutions were analysed in terms of mechanical behaviour and compared to the reference solution.

The best-obtained parameters were then used all together so that an even better solution would be generated. There were emphasized three geometries that exhibit a better cost function value. These three specimens exhibiting a butterfly interior notched shape, produce uniaxial tension and pure shear states in plastic regime, as well as uniaxial compression state mainly in elasticity. Besides, two of the specimens show equibiaxial and plane states within elastic deformations. None of the obtained geometries revealed the biaxial state. When using the heterogeneity indicator I_{T1} for comparison, it was proved that for a uniaxial tensile load test, a rectangular specimen with a non-circular interior notch in the centre displays larger heterogeneity than a circular one. There were noted some problems concerning the methodology, such as the way the specimen's boundary conditions were dealt. In some solutions, the spline's C^1 continuity in the symmetries was not verified when performing the numerical simulation, although theoretically, the curve presents this feature. This issue was not verified in the highlighted solutions, being C^1 continuity verified.

This methodology did not consider several experimental limitations, such as the difficulty of acquiring the data of the specimen's surface near the boundaries, which means that the virtual heterogeity indicator evaluation should be different from the experimental one. In addition, the numerical mesh used does not match with full field spatial resolution, which can also reveal some discrepancies in the comparison. Therefore, the reliability of the developed tests must be verified by performing the experimental test along with the material parameter identification. In terms of the objective function used, this is still a subject that requires more study, since its dependency in the final result is very large. The heterogeneity indicator I_{T3} revealed some interesting solutions, since it privileged specimens with larger equivalent plastic strain, resulting in few elements within the elastic region. However, more strain and stress states could be considered in this indicator, not just the uniaxial tensile, the uniaxial compression and the pure shear.

4.2 Future works

After the development of the present work, some future research can be outlined:

- A more complex constitutive model in order to simulate more accurately the material mechanical behaviour.
- A numerical mesh coincident to the ones employed in the experimental data acquisition can be used.
- Besides, the non-consideration of the elements near the specimen's border for the heterogeneity criterion evaluation could lead to more realistic results.
- The experimental validation and the identification of the material parameters could be performed to find the reliability of the design test.
- The overall methodology could also be improved with the analysis of some new possibilities, such as the use of a non-symmetric specimen, or a specimen with more than one hole, or even the interior notch definition with other curve parametrisations. A non-symmetric specimen could provide larger mechanical information than symmetric ones. The same could occur when having several different shaped holes, whereas the use of different curve parametrisations could generate different shapes to analyse and compare.
- In addition, it is proposed to develop the heterogeneity indicator I_{T3} for more strain and stress states, or even develop new ways of ranking and comparing the mechanical information. This issue is very relevant for the guidance of the optimisation procedure and should be well defined.
- The performed research with the differential evolution algorithm did not reveal the expected results, so it could be interesting to better analyse this strategy and even perform it with a different objective function. This type of algorithms requires large computational time, but could avoid the local minimum finding, and therefore find an even better solution than the here obtained.

Appendix A

Figures from the element dimension dependency analysis

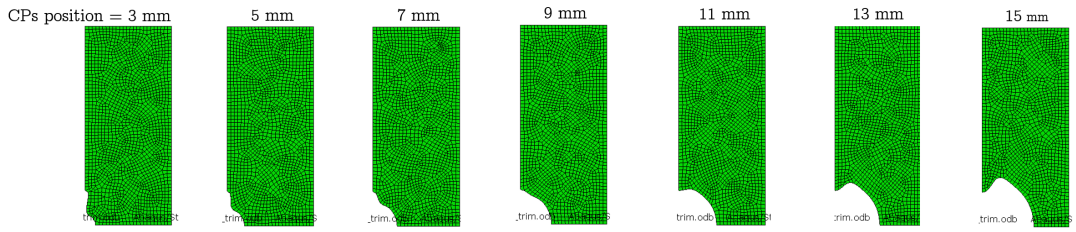

Figure A.1: Some of the analysed solutions for the elements dimension dependency analysis.

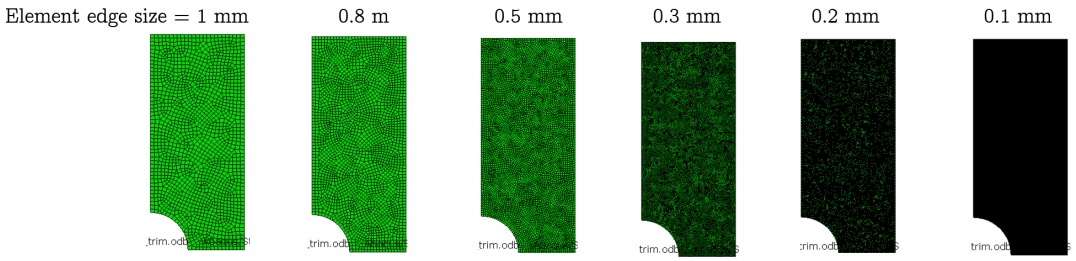

Figure A.2: Numerical meshes used for the elements dimension dependency analysis.

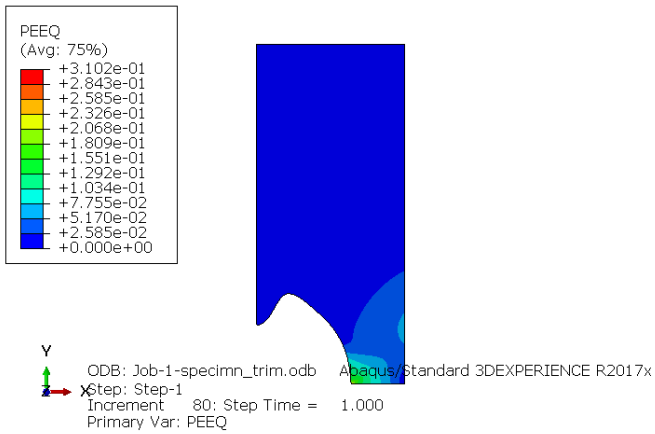

Figure A.3: Equivalent plastic strain obtained for the specimen with 1.6 control points' normalised position and 0.1 mm element edge dimension.

Appendix B

Figure from the element type dependency analysis

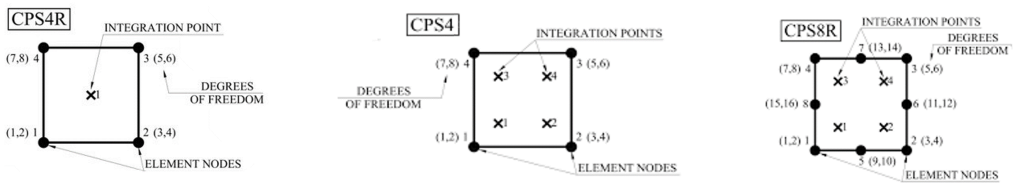

(a) (b) (c)

Figure B.1: Numerical element types used for the variable dependency analysis [Dassault Systèmes 2014].

Intentionally blank page.

Appendix C

Figure from the initial solution dependency analysis

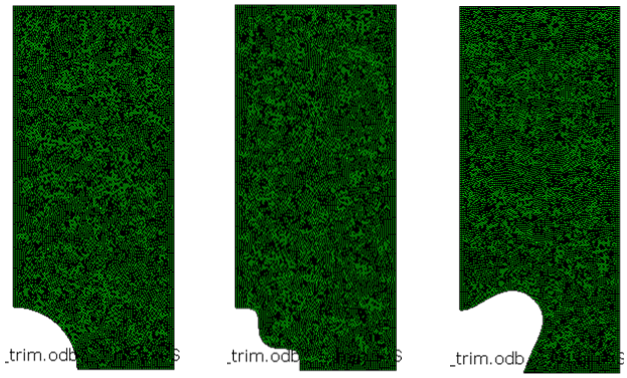

(a) (b) (c)

Figure C.1: Initial solutions used in the optimisation procedure: (a) a round, (b) a cross-like and (c) an ellipse-shaped interior notch.

Intentionally blank page.

Bibliography

[Andrade-Campos *et al.* 2015] A. Andrade-Campos, J. Dias-de Oliveira and J. Pinho-da Cruz. Otimização não-linear em engenharia - cálculo estrutural e computacional em Multiescala. ETEP edições técnicas e profissionais, 1 edition, 2015.

[Andrade-Campos *et al.* 2019] António Andrade-Campos, José Aquino, João M.P. Martins and Bernardete Coelho. On the design of innovative heterogeneous sheet metal tests using a shape optimization approach. *Metals*, 9(3), mar 2019.

[Aquino *et al.* 2019] José Aquino, A. Gil Andrade-Campos, João M.P. Martins and Sandrine Thuillier. Design of heterogeneous mechanical tests: Numerical methodology and experimental validation. *Strain*, 55(4), aug 2019.

[ASTM E8 2010] ASTM E8. ASTM E8/E8M standard test methods for tension testing of metallic materials 1. *Annual Book of ASTM Standards 4*, (C):1–27, 2010.

[Banabic *et al.* 2010] Dorel Banabic, Frédéric Barlat, Oana Cazacu and Toshihiko Kuwabara. Advances in anisotropy and formability. *International Journal of Material Forming*, 3(3):165–189, 2010.

[Barroqueiro *et al.* 2020] B. Barroqueiro, A. Andrade-Campos, João Dias-de Oliveira and R. A.F. Valente. Design of mechanical heterogeneous specimens using topology optimization. *International Journal of Mechanical Sciences*, 181, 2020.

[Belhabib *et al.* 2008] S. Belhabib, H. Haddadi, M. Gaspérini and P. Vacher. Heterogeneous tensile test on elastoplastic metallic sheets: Comparison between FEM simulations and full-field strain measurements. *International Journal of Mechanical Sciences*, 50(1):14–21, 2008.

[Brosius *et al.* 2011] A. Brosius, Q. Yin, A. Güner and A. E. Tekkaya. A new shear test for sheet metal characterization. *Steel Research International*, 82(4):323–328, 2011.

[Campos *et al.* 2014] Hugo Campos, Abel D. Santos, Bruno Martins, K. Ito, N. Mori and F. Barlat. Hydraulic bulge test for stress-strain curve determination and damage calibration for Ito-Goya model. *11th World Congress on Computational Mechanics, WCCM 2014, 5th European Conference on Computational Mechanics, ECCM 2014 and 6th European Conference on Computational Fluid Dynamics, ECFD 2014*, (Wccm Xi):4223–4238, 2014.

[Chamoin *et al.* 2020] L. Chamoin, C. Jailin, M. Diaz and L. Quesada. Coupling between topology optimization and digital image correlation for the design of specimen dedicated to selected material parameters identification. *International Journal of Solids and Structures*, 2020.

[Choung and Cho 2008] J. M. Choung and S. R. Cho. Study on true stress correction from tensile tests. *Journal of Mechanical Science and Technology*, 22(6):1039–1051, 2008.

[Cooreman 2008] Steven Cooreman. Identification of the plastic material behaviour through full-field displacement measurements and inverse methods. PhD Thesis, Free University of Brussels, Belgium, 2008.

[Cooreman *et al.* 2008] S. Cooreman, D. Lecompte, H. Sol, J. Vantomme and D. Debruyne. Identification of mechanical material behavior through inverse modeling and DIC. *Experimental Mechanics*, 48(4):421–433, 2008.

[Dassault Systèmes 2014] Dassault Systèmes. Abaqus 6.14 Online Documentation, 2014.

[Grédiac *et al.* 1999] M. Grédiac, F. Pierron and Y. Surrel. Novel procedure for complete in-plane composite characterization using a single T-shaped specimen. *Experimental Mechanics*, 39(2):142–149, 1999.

[Güner *et al.* 2012] A. Güner, C. Soyarslan, A. Brosius and A. E. Tekkaya. Characterization of anisotropy of sheet metals employing inhomogeneous strain fields for Yld2000-2D yield function. *International Journal of Solids and Structures*, 49(25):3517–3527, 2012.

[Hanabusa 2014] Yasuhiro Hanabusa. Biaxial Tensil Testing Machine, 2014.

[Ishiki *et al.* 2011] Mantaro Ishiki, Toshihiko Kuwabara and Yasuhiro Hayashida. Measurement and analysis of differential work hardening behavior of pure titanium sheet using spline function. *International Journal of Material Forming*, 4(2):193–204, 2011.

[Johnston *et al.* 2002] W. M. Johnston, W. D. Pollock, D. S. Dawicke and John a. Wagner. Biaxial Testing of 2195 Aluminum Lithium Alloy Using Cruciform Specimens. (October), 2002.

[Jones *et al.* 2018] E. M.C. Jones, J. D. Carroll, K. N. Karlson, S. L.B. Kramer, R. B. Lehoucq, P. L. Reu and D. Z. Turner. Parameter covariance and non-uniqueness in material model calibration using the Virtual Fields Method. *Computational Materials Science*, 152(June):268–290, 2018.

[Kajberg and Lindkvist 2004] J. Kajberg and G. Lindkvist. Characterisation of materials subjected to large strains by inverse modelling based on in-plane displacement fields. *International Journal of Solids and Structures*, 41(13):3439–3459, 2004.

[Kim *et al.* 2014] J. H. Kim, F. Barlat, F. Pierron and M. G. Lee. Determination of Anisotropic Plastic Constitutive Parameters Using the Virtual Fields Method. *Experimental Mechanics*, 54(7):1189–1204, 2014.

[Knoxville *et al.* 2012] D. Knoxville, V. Knoxville, S. Knoxville and Y. Knoxville. Material mechanical characterization method for multiple strains and strain rates, 2012.

[Küsters and Brosius 2019] N. Küsters and A. Brosius. Damage characterization on heterogeneous tensile tests. *Procedia Manufacturing*, 29:458–463, 2019.

[Liu *et al.* 2015] Wei Liu, Dominique Guines, Lionel Leotoing and Eric Ragneau. Identification of sheet metal hardening for large strains with an in-plane biaxial tensile test and a dedicated cross specimen. *International Journal of Mechanical Sciences*, 101-102:387–398, 2015.

[Makinde *et al.* 1992] A. Makinde, L. Thibodeau and K. W. Neale. Development of an apparatus for biaxial testing using cruciform specimens. *Experimental Mechanics*, 32(2):138–144, 1992.

[Meuwissen 1998] Michael Hubertus Helena Meuwissen. An inverse Method for the mechanical characterisation of metals. PhD Thesis, Eindhoven University of Technology, Netherlands, 1998.

[Mohr and Henn 2007] D. Mohr and S. Henn. Calibration of stress-triaxiality dependent crack formation criteria: A new hybrid experimental-numerical method. *Experimental Mechanics*, 47(6):805–820, 2007.

[Oliveira *et al.* 2020] Miguel Guimarães Oliveira, Sandrine Thuillier and António Andrade-Campos. Analysis of Heterogeneous Tests for Sheet Metal Mechanical Behavior. *Procedia Manufacturing*, 47(831-838), 2020.

[Ozturk *et al.* 2014] Fahrettin Ozturk, Serkan Toros and Suleyman Kilic. Effects of anisotropic yield functions on prediction of forming limit diagrams of DP600 advanced high strength steel. *Procedia Engineering*, 81(October):760–765, 2014.

[Pijlman 2001] Hermen Pijlman. Sheet material characterisation by multi-axial experiments. 1 edition, 2001.

[Pottier *et al.* 2011] T. Pottier, F. Toussaint and P. Vacher. Contribution of heterogeneous strain field measurements and boundary conditions modelling in inverse identification of material parameters. *European Journal of Mechanics, A/Solids*, 30(3):373–382, 2011.

[Pottier *et al.* 2012] T. Pottier, P. Vacher, F. Toussaint, H. Louche and T. Coudert. Out-of-plane Testing Procedure for Inverse Identification Purpose: Application in Sheet Metal Plasticity. *Experimental Mechanics*, 52(7):951–963, 2012.

[Prates *et al.* 2014] P. A. Prates, M. C. Oliveira and J. V. Fernandes. A new strategy for the simultaneous identification of constitutive laws parameters of metal sheets using a single test. *Computational Materials Science*, 85:102–120, 2014.

[Python Software Foundation 2020] Python Software Foundation. Python 3.8.5 documentation, 2020.

[Rauch 1998] E. F. Rauch. Plastic anisotropy of sheet metals determined by simple shear tests. *Materials Science and Engineering A*, 241(1-2):179–183, 1998.

[Slota 2008] J Slota. Determination of flow stress by the hydraulic bulge test. *METABK*, 47(1):13–17, 2008.

[Souto 2015] Nelson Mineiro Souto. Computational design of a mechanical test for material characterization by inverse analysis. PhD Thesis, University of Aveiro, Portugal, 2015.

[Souto *et al.* 2016] Nelson Souto, Sandrine Thuillier and A. Andrade-Campos. Design of a mechanical test to characterize sheet metals - Optimization using B-splines or cubic splines. *AIP Conference Proceedings*, 1769(October), 2016.

[Souto *et al.* 2017] N. Souto, A. Andrade-Campos and S. Thuillier. Mechanical design of a heterogeneous test for material parameters identification. *International Journal of Material Forming*, 10(3):353–367, jun 2017.

[Syed-Muhammad *et al.* 2009] Kashif Syed-Muhammad, Evelyne Toussaint and Michel Grédiac. Optimization of a mechanical test on composite plates with the virtual fields method. *Structural and Multidisciplinary Optimization*, 38(1):71–82, 2009.

[Wagoner 1981] R. H. Wagoner. Comparison of Plane-Strain and Tensile Work Hardening in Two Sheet Steel Alloys. *Metallurgical transactions. A, Physical metallurgy and materials science*, 12 A(5):877–882, 1981.

[Yulong 2015] L. Yulong. Thermal environment two-way stretch cross test piece, 2015.

[Zhang *et al.* 2015] S. Zhang, L. Léotoing, D. Guines and S. Thuillier. Potential of the Cross Biaxial Test for Anisotropy Characterization Based on Heterogeneous Strain Field. *Experimental Mechanics*, 55(5):817–835, 2015.

[Zhu *et al.* 2019] Zhikang Zhu, Zheng Lu, Peng Zhang, Wei Fu, Changyu Zhou and Xiaohua He. Optimal design of a miniaturized cruciform specimen for biaxial testing of ta2 alloys. *Metals*, 9(8), 2019.

[Zidane *et al.* 2014] Ibrahim Zidane, Cunsheng Zhang, Dominique Guines, Lionel Leotoing, Ibrahim Zidane, Cunsheng Zhang, Dominique Guines, Lionel Leotoing and Eric Ragneau Opti. Optimization of biaxial tensile specimen shape from numerical investigations. *Numisheet*, pp. 1–6, 2014.